
A Thesis Presented to

the Faculty of the Department of Earth and Atmospheric Sciences

University of Houston

In Partial Fulfillment

of the Requirements for the Degree Master of Science

in Geophysics

By

Armando Sosa

December 2012

ASSESSMENT OF AZIMUTHAL VARIATIONS IN DEPTH MIGRATED MARINE WIDE-AZIMUTH DATA: WORKFLOW DERIVATION AND EXAMPLES FROM THE EAST BREAKS REGION OF THE GULF OF MEXICO

_____

Armando Sosa

APPROVED:

_____

Dr. Hua-Wei Zhou, Chairman

_____

Dr. Dan Whitmore

_____

Dr. Evgeny Chesnokov

_____

Dr. Leon Thomsen

_____

Dr. Mark A. Smith, Dean
College of Natural Sciences and Mathematics

ACKNOWLEDGEMENTS

I would like to thank my advisors at the University of Houston, Dr. Hua-Wei Zhou, Dr. Leon Thomsen, Dr. Evgeny Chesnokov, and Dr. Chris Liner for the numerous lessons learned and helping me achieve my goals at the university. Special thanks to Dr. Dan Whitmore, who provided constant guidance and new ideas throughout my thesis work over the last couple of years and who was always willing to spend quality time discussing life and geophysical issues.

I would also like to recognize PGS for the financial support, the data used in this study, and the opportunity to present these results. Throughout nearly five years, numerous colleagues have contributed in various ways to help me dedicate time to this research topic. I would particularly like to acknowledge Sean Crawley for his assistance in generating the reverse time migration images used throughout this study, and for our numerous conversations about the migration algorithm itself.

Above all, I would like to thank my family, specifically my wife Dara and my eight-month old son Dristan. Without their unwavering support and understanding throughout this entire process, I would not been able to attain my goals.

ASSESSMENT OF AZIMUTHAL VARIATIONS IN DEPTH MIGRATED MARINE WIDE-AZIMUTH DATA: WORKFLOW DERIVATION AND EXAMPLES FROM THE EAST BREAKS REGION OF THE GULF OF MEXICO

An Abstract of a Thesis Presented to

The Faculty of the Department of Earth and Atmospheric Sciences

University of Houston

In Partial Fulfillment

of the Requirements for the Degree Master of Science

in Geophysics

By

Armando Sosa

December 2012

ABSTRACT

Current seismic acquisition geometries are designed to record a broader range of azimuths. While illumination of subsalt structures is a major factor when planning these surveys, azimuthal variations due to heterogeneity and anisotropy can also significantly impact the imaging of these targets if they are not well understood. This study presents a practical workflow for detecting and assessing the significance of azimuthal variations on wide-azimuth data, in an effort to start to better utilize the azimuthal aspect of this type of survey. The assessment itself was performed in depth migrated images of wide-azimuth data from the East Breaks region of the Gulf of Mexico, which were decomposed into azimuth-sectored angle-domain gathers post-imaging. This data domain provided great flexibility to the analysis of azimuthal moveout anomalies, as different subsets of common angle volumes were evaluated depending on their level of contributions to the imaging of a given geologic target. As the derived workflow was tested in different scenarios, it became clear that analyzing a variety of attributes, volumetrically or at specific interpreted horizons, delivered qualitative results that confirmed the presence of azimuthal variations and how irregular or chaotic these were, depending on the area of interest. Throughout this study, it was quite important to develop quality control plots that aid the validation of the propose techniques. Particularly significant were the cross-correlation azimuthal residual maps and the

attributes used to rule out whether an azimuthal anomaly was being induced by the migration models, since improving the fitting of the data by using a higher order of symmetry system was outside of the scope for this study. It was also concluded that while the resolution of the dataset used in this study was typical for depth migration images in the region, it was not ideal in terms of frequency and azimuthal sampling. However, this analysis did provide multiple insights into the intricacies of assessing azimuthal variations in image space.

CONTENTS

Table of Figures

1. Introduction

This initial chapter will explain the motivation behind this thesis topic, as well as the hypotheses to be tested, and the objectives that I'm trying to achieve. Additionally, section 1.4 (Exclusions) will cover the limits in the scope of this study.

Chapters 2 and 3 will cover the basic background information regarding the geology of the area of study, and how those data were acquired and processed prior to migration. Finally, Chapter 4 will be the crucial chapter, since it starts by explaining the migration used to produce azimuth-sectored angle gathers and the nature of azimuthal variations, follows with how the workflow to assess azimuthal variations was derived and tested, and concludes with the presentation and discussion of results obtained after applying the derived workflow in several subsets of the test area.

1.1 Motivation

The motivation for performing an azimuthal variations assessment on wide-azimuth migrated images, was to attempt to extract additional information from these types of datasets. Not only do recently acquired marine exploration surveys tend to have improved azimuthal sampling and broader bandwidth, but with today's computer resources, the imaging of complex geologic structures with algorithms like reverse time migration is done considerably more routinely. These elements create an opportunity to

develop workflows to better utilize today's data and technology, with the purpose of gaining further understanding of the geologic properties of a particular region.

1.2 Hypotheses

With the increase of azimuthal sampling by wide-azimuth marine acquisition geometries, data corresponding to a wider range of opening angles and source-receiver azimuths ought to show azimuthal moveout differences due to heterogeneity and anisotropy, if the geologic scenario in question does present these complexities. Likewise, if regional azimuthal variations are recorded, these should be detectable in pre-stack depth migration images.

1.3 Objectives

This study focuses on assessing azimuthal variations associated with differential moveout across azimuths. In order to achieve this type of evaluation, an efficient data analysis workflow was derived and tested on a wide-azimuth dataset that has potential to exhibit these variations, based in the regional geologic setting. Additionally, recommendations on the suitability of a dataset for this type of analysis were included in the scope of this study.

If possible, it would also be of interest to correlate regional moveout patterns to ongoing geological processes, and to generate measurements of how consistent these are throughout an area. Depending on the magnitude and distribution of results, observations on the potential image-quality uplift to be obtained from either migrating with a higher order symmetry system, or applying residual moveout corrections to improve stacking response (or both), will be of great value.

1.4 Exclusions

For this study, the use of azimuth-sectored angle gathers will be limited to studying the disparities on moveouts across sectors, not the differences in amplitudes or illumination across sectors.

Also, the derivation of updated models through inversion or any additional model building work will not be included in the scope of this study.

2. Geologic Setting

2.2 Overview

Publications by Galloway *et al*. (2000), Rowan *et al*. (2004) and McDonnell *et al* (2008) on how today's northern portion of the GOM evolved explain the regional geological features that can be observed throughout most of the area considered in this study (see Figures 2-1 and 2-2).

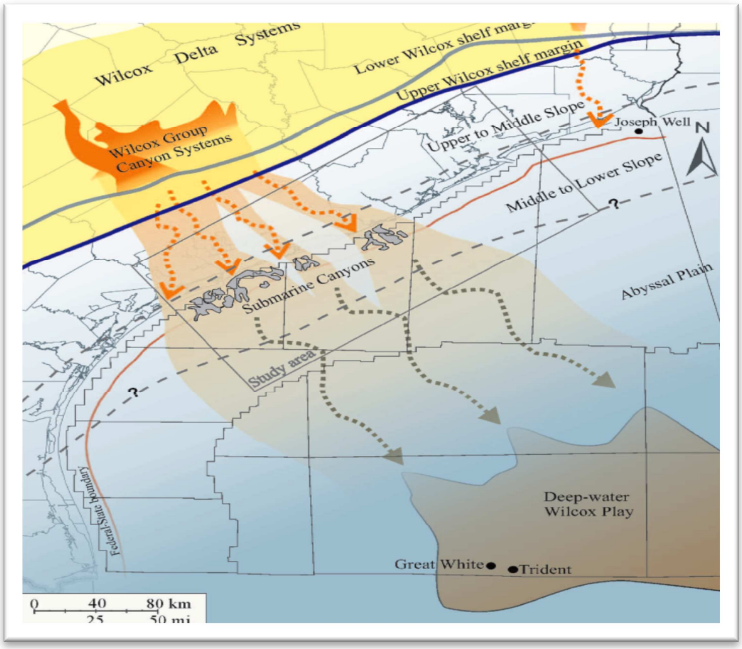

Figure 2-1. Schematic diagram for Western GOM depositional systems. Modified from McDonnell et al. (2008).

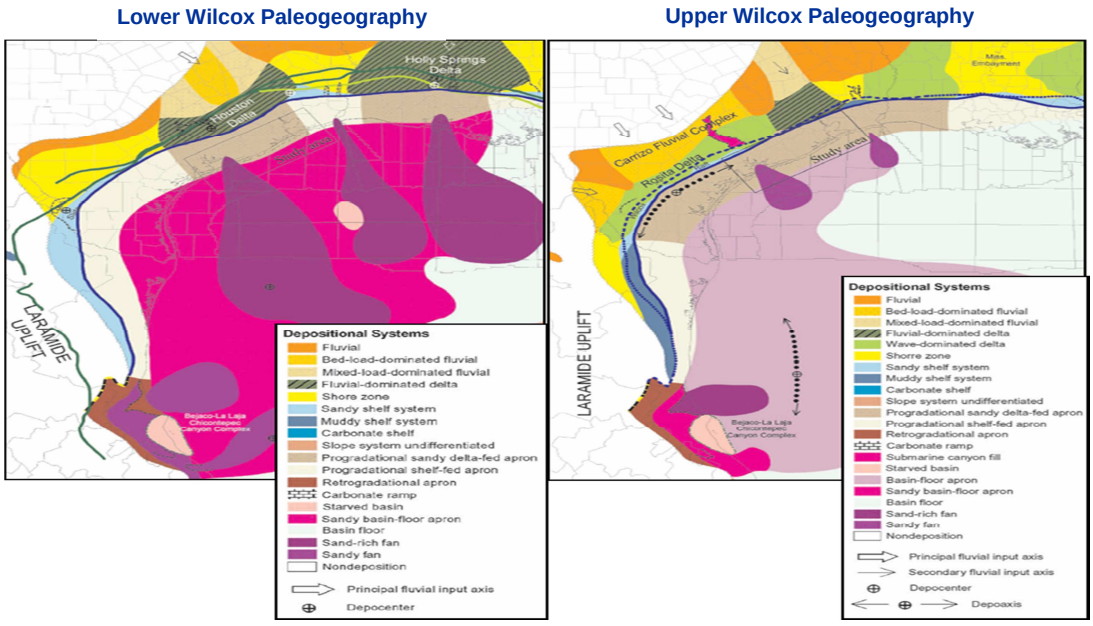

Figure 2-2. Western GOM Paleography map indicating the different depositional systems for the Lower and Upper Wilcox. Modified from Galloway et al. (2000)

The basic geologic scenario consists on a shallow portion of relatively young clastic sediments, possibly Plio-Pleistocene in age, underlain by a regional unconformity. Below this unconformity, there is a relatively thick and mostly transparent Oligocene Shale section (Figure 2-3), which shows extensive folding due to ongoing tectonic processes. The reflectivity of these shales varies throughout the area, as internal reflectors come and go due to the presence or absence of sands being deposited at a particular location and time. This Oligocene Shale section extends down to the top of salt.

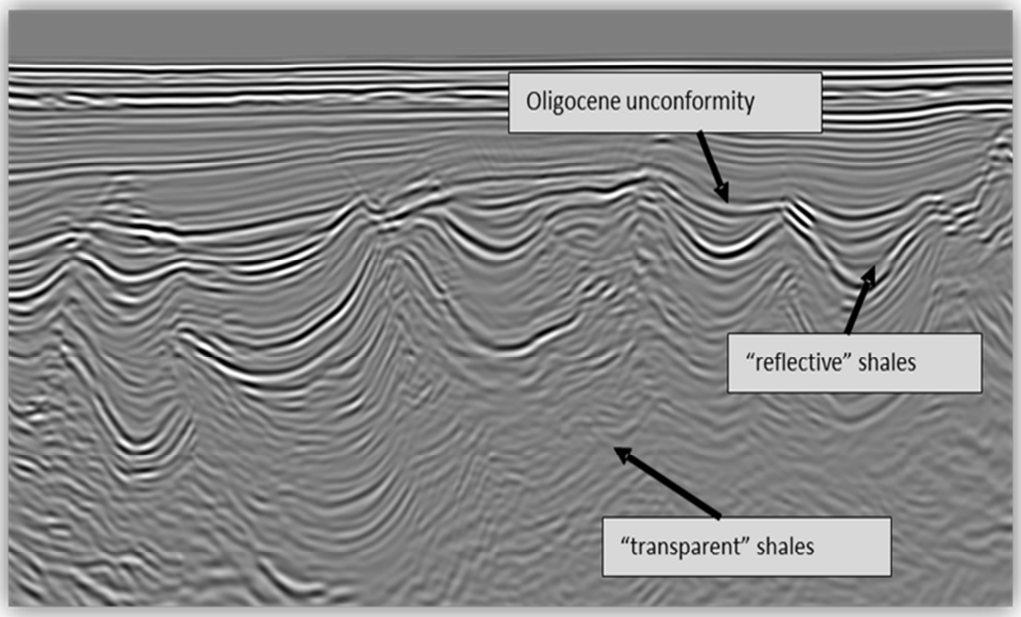

Figure 2-3. Shallow RTM stack showing a close-up of the interpreted Oligocene shale section.

As shown in Figure 2-4, the salt for this particular test area is part of a large canopy system, with the top of the unit being considerably rugose and containing multiple overhangs. This allochthonous salt perhaps moved down regional dip by extension and differential loading of the Oligocene shales. Up-dip, portions of the system are dominated by salt evacuation, which most likely was the driving mechanism to inflate the salt canopy system located in our area of interest. At some locations, the salt has actually evacuated completely and only a salt weld or salt detachment has been interpreted.

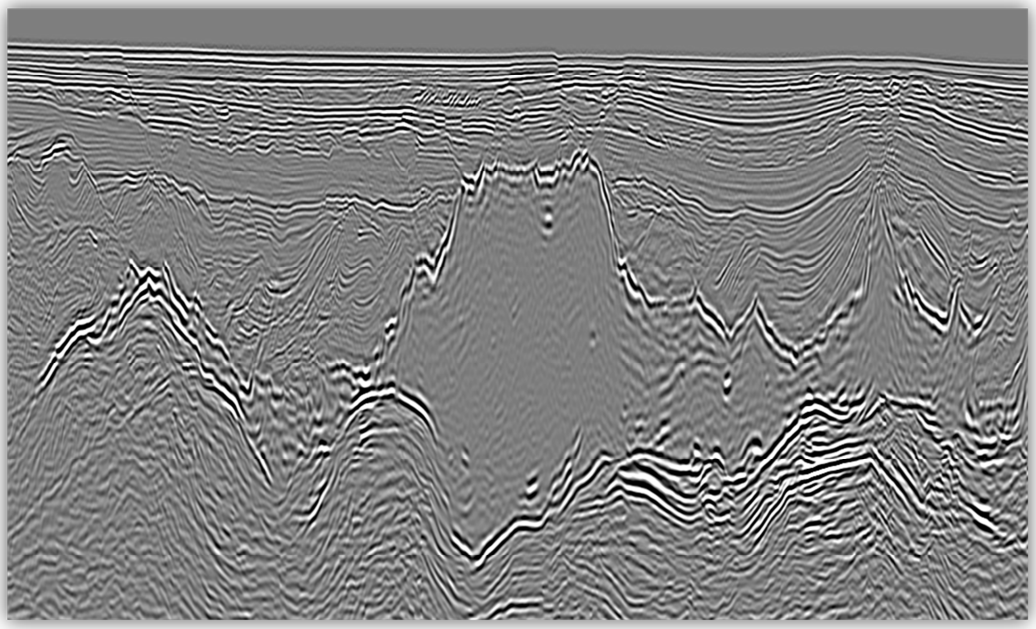

Figure 2-4. RTM stack displaying a close-up of a strike line that intersects the large salt canopy system.

However, other portions of the survey exhibit different salt-geometries. Figure 2-5 displays a salt stock with a relative flat shallow top and hints of a pinched-out or out of plane feeder system.

Below the salt bodies or salt detachment, there appears to be lower Paleogene clastic rocks, underlain by the top of the Cretaceous unit, but this study will concentrate on the analysis of the Plio-Pleistocene clastic sediments, down to the Oligocene Shale section.

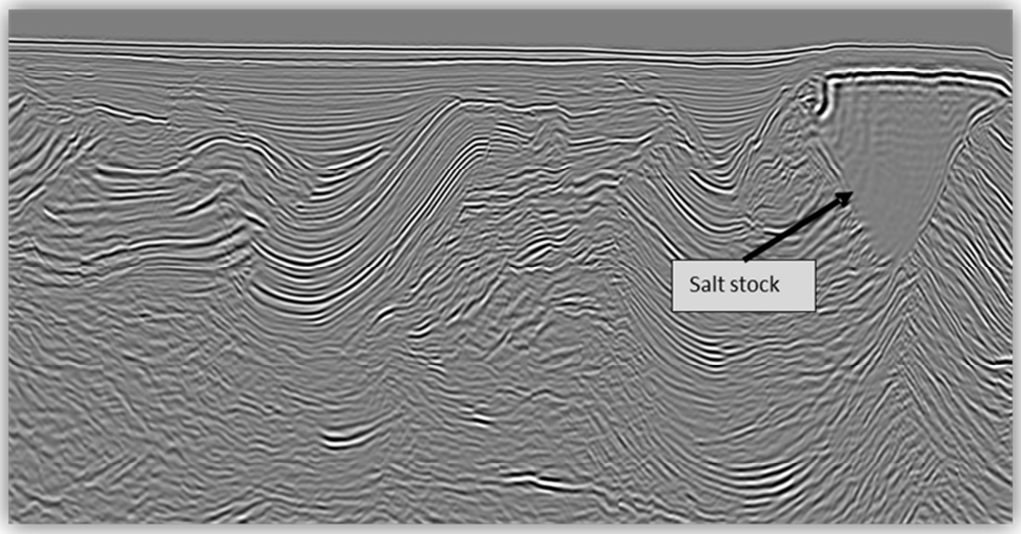

Figure 2-5. RTM stack image displaying a salt stock to the right hand side of the image.

A general overview of the geological picture can be demonstrated with Figures 2-6 and 2-7. These consist of displays of seismic stack sections corresponding to one representative strike line (inline) and one dip line (crossline) line through approximately the central portion of the dataset, with their respective V_{tilt} (velocity along the assumed tilted symmetry axis) and regional geologic interpretation overlays.

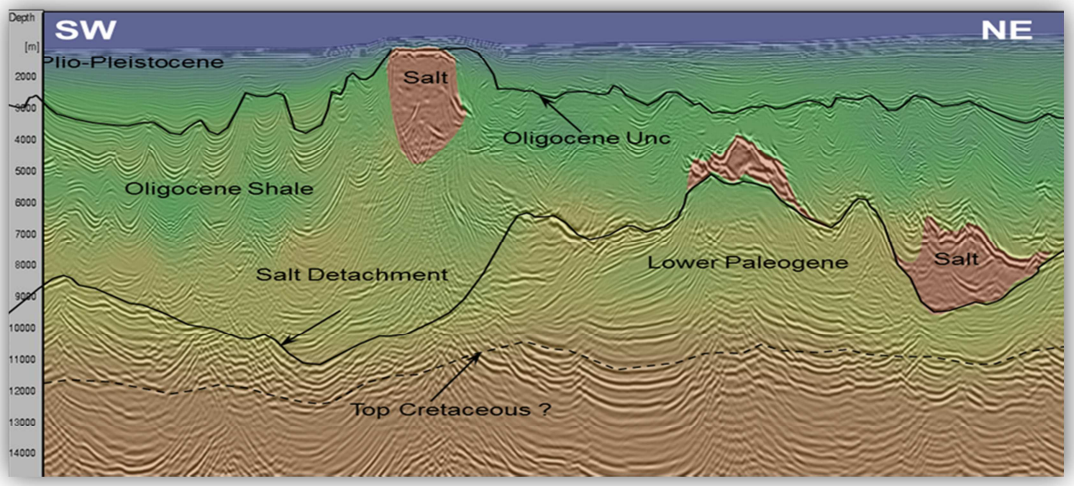

Figure 2-6. Sample inline display with regional (strike) interpretation overlay. The seismic corresponds to a Beam migration on the final TTI models, while the velocity overlay corresponds to Vtilt. Modified from PGS Crystal III processing report.

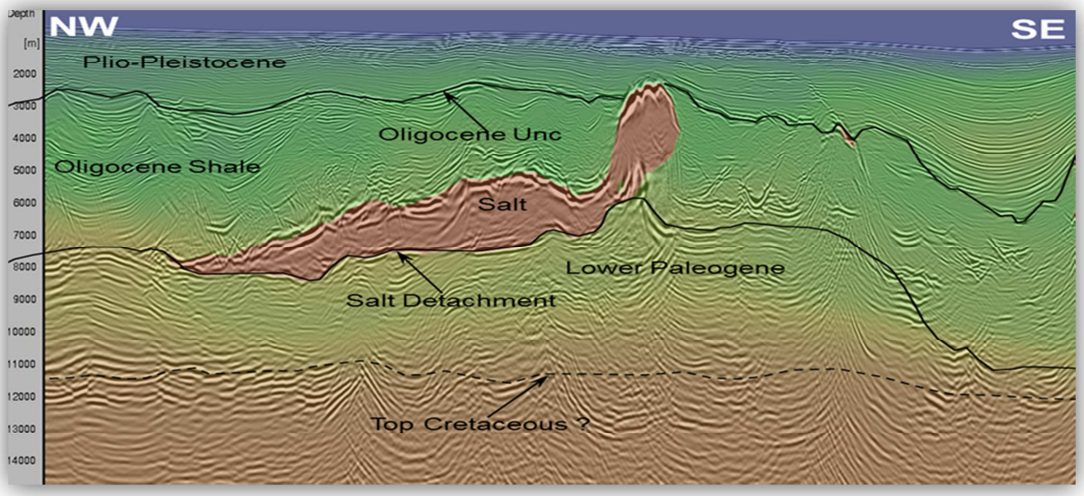

Figure 2-7. Sample inline display with regional (dip) interpretation overlay. The seismic corresponds to a Beam migration on the final TTI models, while the velocity overlay corresponds to V_{tilt}. Modified from PGS Crystal III processing report.

2.3 Geologic Sources of Azimuthal Variations

This section will describe the main potential geologic sources of azimuthal variations. While it is challenging to differentiate between azimuthal patterns caused by complex heterogeneity or anisotropy, certain contributors are more likely to produce an azimuthal bias due to anisotropy than others.

A geologic regime with substantial presence of shale, young clastic sedimentary rocks, tilted and finely layered media, and allochthonous salt, ought to have multiple geologic sources that can induce azimuthal variations. The question is to which extent these patterns are observable at the selected seismic scale, sampling criteria and a given survey geometry.

In terms of heterogeneity, in areas where the geology is relatively simple and the models are accurate and smooth, these should not induce azimuthal variations. However, in complex geology, the limited resolution or errors associated with these models could result in azimuthal deviations, if the heterogeneity is not fully accounted for.

While shales and thin layers in general are widely known for their polar anisotropic effects, faulting and folding are indicative of ongoing compression and extension due to unequal regional stresses (Figure 2-8). Relatively shallow flat sediments tend to exhibit azimuthal anisotropy, as young unconsolidated sediments are compliant and in presence of large regional stresses will tend to exhibit azimuthal variations (Cary *et al*.,

2010). For this study, azimuthal variations related to anisotropy are expected to result primarily from regional stresses and preferentially oriented fractures, as these fit plausible geological models, for Plio-Pleistocene sediments.

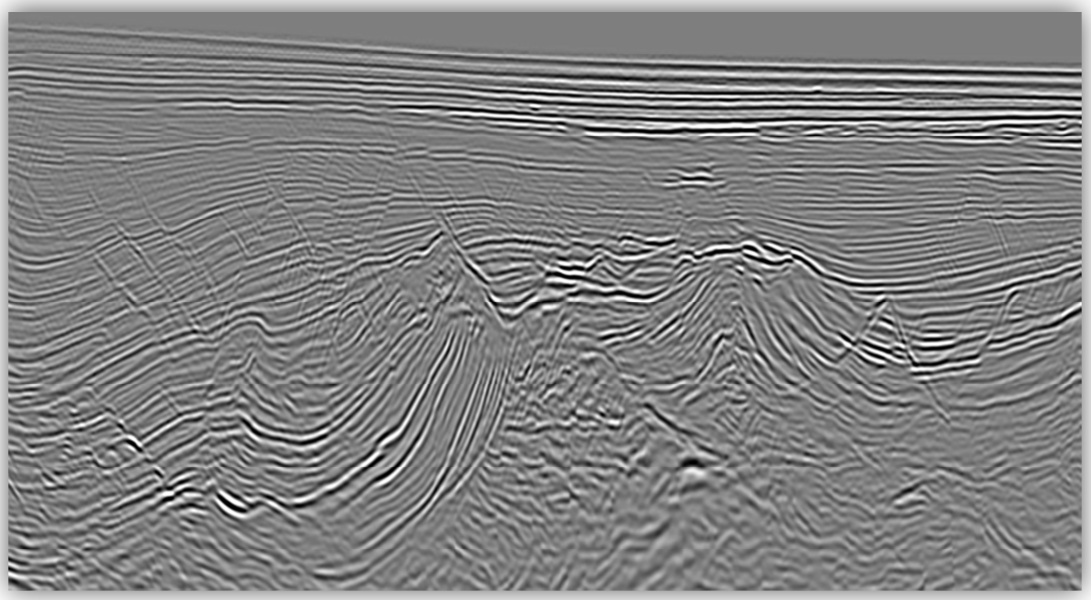

Figure 2-8. Shallow RTM stack section displaying various examples of faulted and folded sections through Plio-Pleistocene sediments.

There are also several salt bodies that are part of a large canopy system. As salt migrated and created complex structures, it could have induced azimuthal effects due to both heterogeneity and anisotropy, but the majority of these effects would depend heavily on the timing and magnitude of the salt evacuation. However, substantial stresses caused by salt displacement at a large scale will be considered part of the regional stresses previously mentioned.

3. Seismic Dataset

3.1 Wide-azimuth Towed Streamer Acquisition

Over the last decade in the Gulf of Mexico, oil and gas exploration has evolved towards drilling more complex structures in deeper water. Marine seismic acquisition has then progressed towards acquiring seismic data that illuminates a broader range of subsurface target events. Wide-azimuth towed streamer (WATS) type acquisition is one of the solutions that provides higher fold data with a larger range of continuous offsets and azimuths. The basic assumption is that the increase in fold, crossline offsets and azimuthal coverage, will aid the imaging of complex structures (Michell *et al*., 2006). Also note that the inherent redundancy in the recorded data tends to attenuate noise. Figure 3-1 summarizes the current main styles of marine seismic acquisition in terms of azimuthal coverage for exploration surveys.

WATS acquisition is characterized by repetition of shot locations while recording a broader range of offsets and azimuths by deploying multiple shooting and recording vessels simultaneously during acquisition. For cost-effective reasons, the shot density is typically relatively low with respect to narrow-azimuth (NAZ) surveys, due to a relatively coarse shot-point grid, with shot intervals usually in the range of hundreds of meters. Moreover, while wide-azimuth surveys are typically designed for imaging complex subsurface features, like subsalt plays, deep carbonate structures or autochthonous salt,

these datasets also provide significantly larger distribution of crossline offsets and azimuths throughout the data.

Marine Acquisition Scheme	Description
Narrow-azimuth	Single vessel towing both source(s) and streamers.
Multi-azimuth	Multiple narrow-azimuth type surveys acquired along different orientations.
Wide-azimuth	Multiple vessels simultaneously towing either or both sources and/or streamers.
Rich-azimuth	A combination of the multi-azimuth and wide-azimuth patterns.

Figure 3-1. Marine towed streamer acquisition schemes, categorized by azimuthal coverage.

While additional azimuthal coverage can be achieved by a combination of 2 or more acquisition patterns (Figure 3-2), WATS is one of the few cost-efficient methods that by itself provides a significant amount of continuous azimuthal coverage for marine towed streamer acquisition. Over the last 5 to 10 years, marine seismic acquisition has evolved and will keep progressing; the sketches on Figure 3-2 are only a representation of the fold and acquisition geometries for a generic but representative model of each particular type of acquisition.

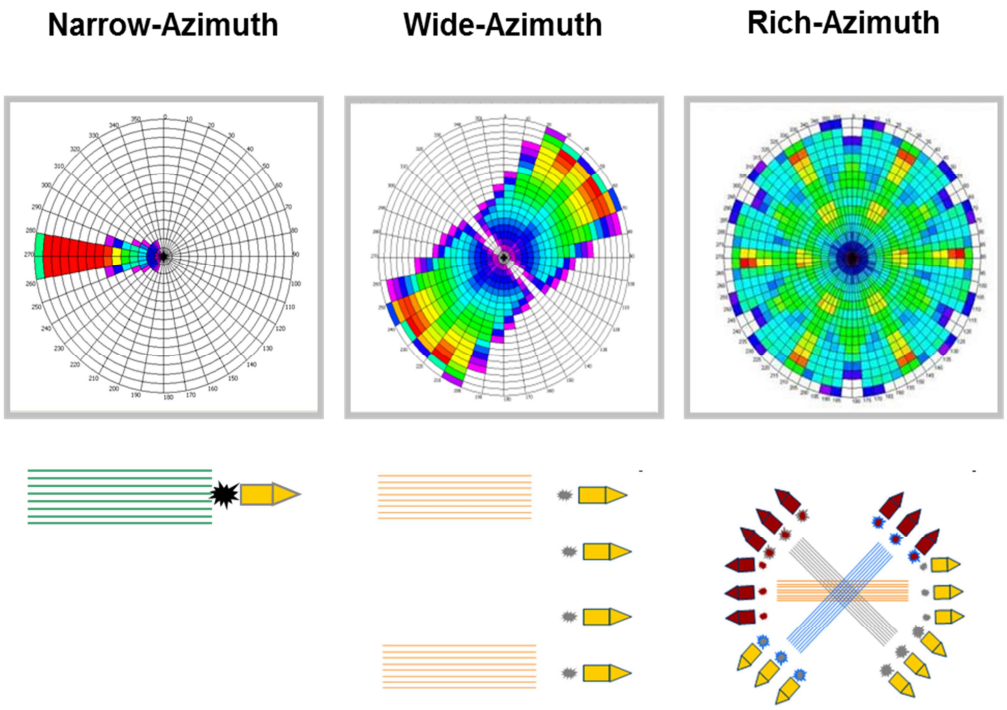

Figure 3-2. Rose diagrams and acquisition geometry sketches for narrow-azimuth, wide-azimuth and rich-azimuth marine acquisitions. Note the higher fold bands, represented by hot colors, are recorded along the direction in which the seismic vessels are travelling. Courtesy of PGS.

3.2 Dataset Description

This study will use a subset of the *Crystal III WATS* dataset to better utilize the broader azimuthal sampling in an attempt to evaluate azimuthal variations throughout the dataset. This particular survey was acquired by PGS during 2009 in the East Breaks and Alaminos Canyon regions of the Western Gulf of Mexico (Figure 3-3).

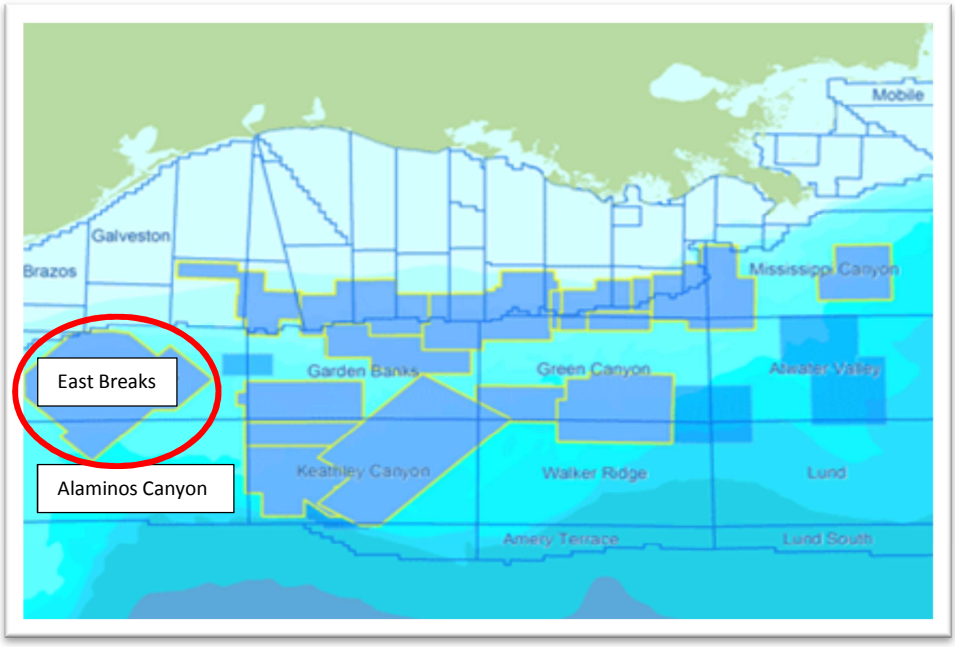

Figure 3-3. Regional Northern Gulf of map highlighting the Crystal III WATS survey with a red oval, south of Galveston, Texas. Modified from PGS Online.

Designed to generate 4 tiles of WATS data or an equivalent of 4.2 kilometers of crossline offsets and approximately 7 kilometers of inline offsets, this survey ought to contain a sufficient range of azimuths and offsets for evaluating regional azimuthal variations. The survey was acquired with a nominal fold of 184, and natural common mid-point bins of 6.25 by 60 meters. Figure 3-4 shows a schematic diagram of the 4 source vessels, with 2 of them also acting as recording vessels. Note that there was 1200 meters of separation between each boat and sail-lines were acquired in a parallel and anti-parallel alternating fashion every 600 meters. This provided the desired symmetric coverage along the North-East/South-West and South-West/North-East directions.

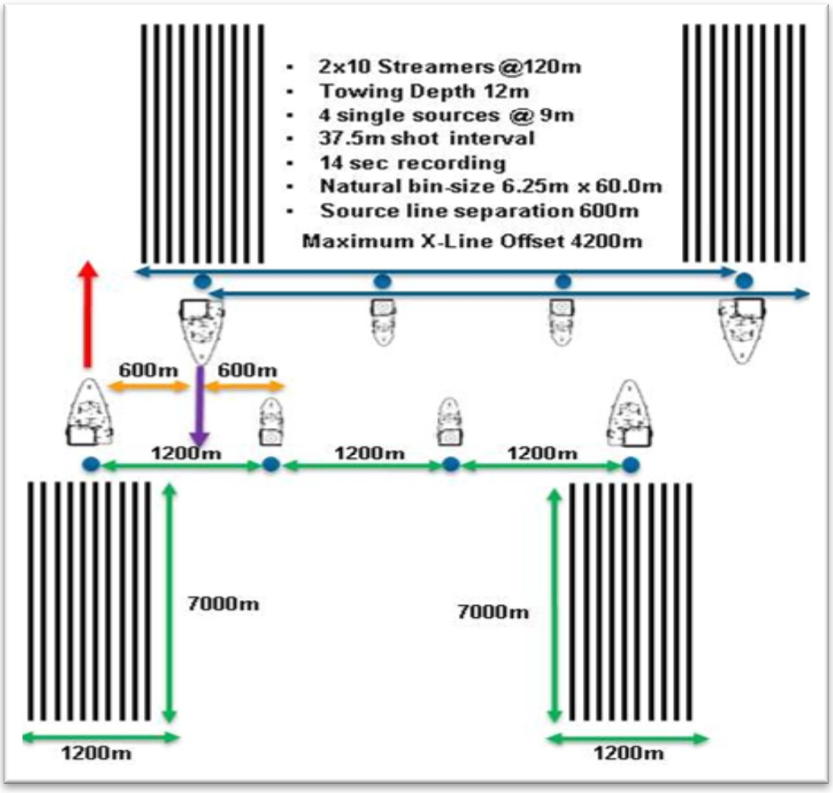

Figure 3-4. Shooting geometry representation of the Crystal III wide-azimuth acquisition. On each pass the vessels are separated by 1200m, while every 600m a line is acquire in a parallel-antiparallel alternating fashion. Courtesy of PGS.

For this survey, the streamers were towed at 12 meters, while the source array depth was 9 meters. The effective shot density was a coarse grid of 150 by 600 meters. Along the defined x (or sail-line) direction, the sources were fired every 150 meters, with distance between adjacent sail-lines being 600m. Finally, each shot point location should have effectively been shot a total of 4 times.

3.3 Pre-processing

3.3.1 Processing Sequence

Next is a summary of the key processing steps performed during the pre-processing of the data (Figure 3-5):

Processing Step	Description
Designature	A model-based minimum phase designature filter was applied globally to the data.
Debubble	A global filter was design to attenuate bubble effects in the data.
Spherical Divergence	A gain equal to t^1.5 was applied
Noise Attenuation	Noise attenuation was applied on different domains to mitigate swell, seismic interference and strum noise.
Data Regularization	Due to the relative sparseness of WATS acquisition, no regularization step was performed.
Multiple Attenuation	Surface related multiples were mitigated by adaptably subtracting the derived multiple model from the data (SRME technique).
Q Compensation	A Q value of 100 (phase only) was applied to compensate for attenuation.

Zero Phase Filtering	A filter was applied to take the data to zero phase.
Water Column Statics	Existing water column timing differences between sail-lines were minimized by statics shifts.

Figure 3-5. Brief summary of data pre-processing.

Note that the input data to the shot grouping was also resampled to 8 msec. since the target maximum frequency was in the 15-20Hz range.

3.3.2 Shot Grouping

The wide-azimuth geometry favors shot migrations like reverse time migrations. This is because, ideally, multiple shots should overlay the same geographic location, and the number of traces per shot would not vary the runtime associated with migrating any given single shot. Shots within a specified distance from each other can be grouped together into what will be referred as a supershot. For this particular survey, the acquisition of 4 tiles of data resulted in 4 clustered shots around the intended shot position and seven receiver patches associated with those shots (Figure 3-6). This means that for a given supershot, there is an associated receiver spread of 7 by 8.4 kilometers, or an equivalent area of 58.8 square kilometers.

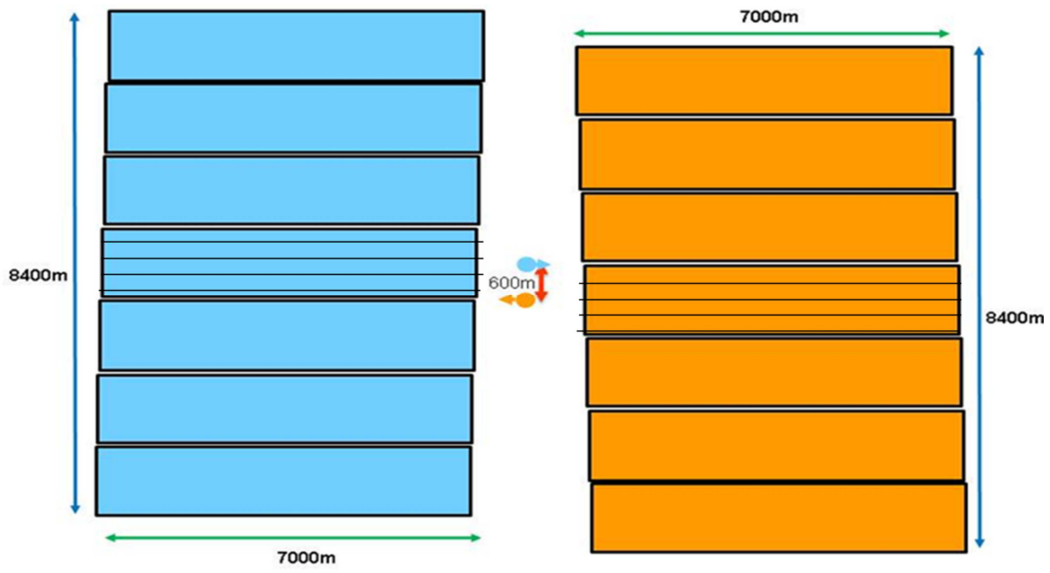

Figure 3-6. Example of 2 adjacent supershots and their associated receiver patches. Note that for this acquisition pattern, the shooting alternates between parallel and antiparallel acquisition lines, and the center patch highlighted by solid black lines is effectively double fold. Courtesy of PGS.

To take advantage of this redundancy in the acquisition geometry, and to lower the migration costs, shot grouping was performed to combine the 4 shots associated with each shot point location. The new shot-x and shot-y locations were calculated by averaging all of the contributing shot coordinates, and then shots were moved to the new assigned location by using differential normal moveout while adjusting receivers and midpoints accordingly. The shot grouping resulted in supershots every 600m along the inline direction and 150m along the crossline direction.

3.4 Considerations

To follow are a few thoughts on how the different pre-processing steps can potentially impose an azimuthal bias to the data, or introduce artifacts that will be problematic for the purpose of this study:

When grouping shots into supershots, the average distance shots were moved by differential normal moveout was on average less than 30m. The assumption here is that for such distances, moving the data by differential normal moveout will not result in significant distortion of the final images, and specifically will not introduce an azimuthal bias.

Surface-related multiples will only be attenuated below the first water bottom multiple, therefore for this deep-water survey the shallow data will not be biased by this pre-processing step.

A surface-consistent water-column statics solution was necessary to minimize crossline timing differences between sail-lines. The resulting solution provided a more continuous water bottom surface (as shown in Figure 3-7 and Figure 3-8), which is consistent with the expected geology and should lessen artifacts along the crossline direction.

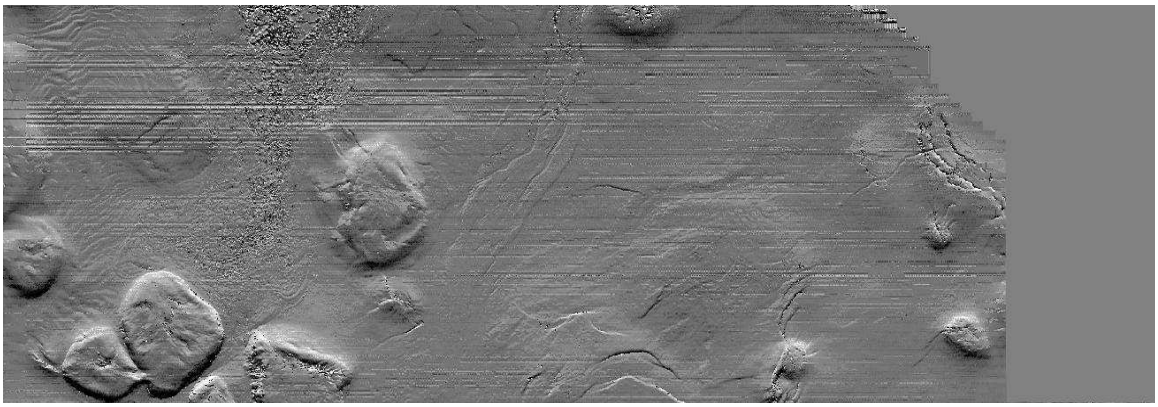

Figure 3-7. Example of water bottom surface without water column statics.

Quite a few of these pre-migration processes are applied trace by trace, without any azimuthal discrimination that could exacerbate azimuthal variations present throughout the data. For example, global filters affect all traces equally, and therefore do not induce an azimuthal bias. Finally, the most important assumption is that this WATS dataset will possess enough azimuthal sampling to observe and analyze regional azimuthal patterns at the target locations.

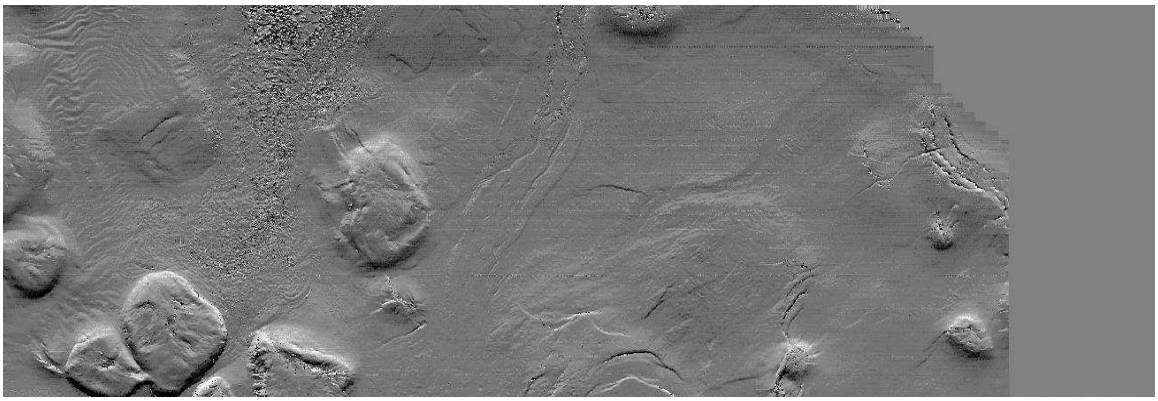

Figure 3-8. Example of water bottom surface with water column statics.

4. Methodology and Results

For this chapter, the first sections will cover the necessary background and details concerning migration and azimuthal variations, while the main portion of the chapter will be dedicated to explaining how to effectively analyze the data and the discussion of the results obtained.

4.1 Migration

Since the majority of the data to be used throughout this study correspond to azimuth-sectored angle-domain common image gathers (ADCIG's) generated by a tilted polar anisotropic implementation of reverse time migration, the following subsections will briefly cover: (1) the approximations taken in migration algorithm itself, (2) the models used in the migration and (3) the angle-domain output generated for this study.

4.1.1 Pre-stack Depth Migration

Pre-stack depth migration is the ideal choice when dealing with high velocity contrast between rocks with complex structures. Within depth migration algorithms, reverse time migration has recently been the premier choice for imaging steep dips and complex geologic targets. This particularly applies to Gulf of Mexico datasets, due to the frequent presence of complicated salt bodies with steep flanks.

Geologically complex regimes tend to be significantly anisotropic, and therefore imaging algorithms in such cases should account for some degree of anisotropy. Nowadays in the Gulf of Mexico, vertical polar anisotropy (also known as "Vertical Transverse Isotropy", VTI) and tilted polar anisotropy (TTI) models are routinely used in pre-stack depth migrations. Throughout this study, the data will be migrated with tilted polar anisotropic models.

The study area presents numerous salt bodies with very different geometries, mini-basins with dipping stratigraphy, faulted and folded clastic sediments, and interleaved shale and sandstone sequences. While the convergence of all of these features calls for an anisotropic pre-stack depth migration, such migration will only be an approximation of the true subsurface and ideally account for the heterogeneity at the target seismic scale.

4.1.2 Reverse Time Wave Propagator

The data used throughout this study was recorded using hydrophones that only record changes in pressure. This pressure data is associated with reflected compressional waves (P-waves) rather than shear waves (S-waves) and their respective mode conversions. Because only reflected P-waves are recorded as signal and for

computational efficiency, the wave propagator used throughout is an approximation to the full TTI equations.

$$\begin{aligned}\omega^4 &= \left[(V_{px}^2 + V_{sz}^2)(\hat{k}_x^2 + \hat{k}_y^2) + (V_{pz}^2 + V_{sz}^2)\hat{k}_z^2\right]\omega^2 \\ &- V_{px}^2 V_{sz}^2 (\hat{k}_x^2 + \hat{k}_y^2)^2 - V_{pz}^2 V_{sz}^2 \hat{k}_z^4 \\ &+ \left[V_{pz}^2 (V_{pn}^2 - V_{px}^2) - V_{sz}^2 (V_{pz}^2 + V_{pn}^2)\right](\hat{k}_x^2 + \hat{k}_y^2)\hat{k}_z^2\end{aligned} \qquad \text{(I)}$$

Papers by Fowler et al. (2010), Etgen and Brandsberg-Dahl (2009), and Chu et al. (2011), discuss in detail the acoustic approximations done for anisotropic P-wave propagation. Equation I represents the general dispersion relationship used for TTI media, where V_{PZ} is the P-wave velocity along the symmetry axis, V_{PX} is the P-wave perpendicular to the symmetry axis and V_{SZ} is the S-wave velocity on the symmetry axis. Additionally V_{PX} and V_{PN} are defined as functions of V_{PZ} and the Thomsen parameters δ and ε:

$$V_{px} = V_{pz}(1+2\varepsilon)^{1/2} \qquad V_{pn} = V_{pz}(1+2\delta)^{1/2}$$

Note that these TTI equations are based on VTI relationships that are then rotated according to the measured tilt angle θ and azimuth φ. The necessary rotations are shown below in Equation (II):

$$\begin{bmatrix}\hat{k}_x \\ \hat{k}_y \\ \hat{k}_z\end{bmatrix} = \begin{bmatrix}\cos\theta\cos\phi & \cos\theta\sin\phi & \sin\theta \\ -\sin\phi & \cos\phi & 0 \\ -\sin\theta\cos\phi & -\sin\theta\sin\phi & \cos\theta\end{bmatrix}\begin{bmatrix}k_x \\ k_y \\ k_z\end{bmatrix} \qquad \text{(II)}$$

Additional approximations are then taken to numerically solve these equations, but the particular details were considered to be outside the scope of this study. However, even though these approximations are not ideal, they are still considered to provide a suitable description of the wave propagation through the subsurface for the scale and purpose of this exercise. Ramos-Martinez et al. (2011) compared wavefield snapshots using the same wave propagator with exact traveltimes from solving ray equations, and at least for relatively small Thomsen parameters, both results reasonably agreed.

4.1.3 TTI Migration Models

In practice, a total of five parameters are used by the RTM code described above to image data at their respective migrated locations. Figure 4-1 presents a table with these models and a short description of each one.

The required velocity for tilted polar migrations V_{tilt}, was derived through reflection tomography and interpretation of high velocity geobodies like salt. It is important to mention that the symmetry plane is always assumed to be parallel to the bedding and therefore structurally conformant, although in the presence of stresses this might not be the case.

Parameter Name	Description
Tilt Velocity **(V_{tilt})**	The equivalent to the vertical velocity, but along the tilted symmetry axis.
Delta (δ)	Thomsen's parameter for near offset moveout corrections in weak anisotropy, referred to the tilted axis.
Epsilon (ε)	Thomsen's parameter for far offset moveout corrections in weak anisotropy, referred to the tilted axis.
Inline Slope	Reflector dips measured on stack data along the inline direction.
Crossline Slope	Reflector dips measured on stack data along the crossline direction.

Figure 4-1. Polar anisotropy models and their respective short-definitions.

The δ model was initially based on mis-ties between interpreted events in well-logs and their equivalent positions in an isotropic migration section. Then a regional smooth function that honored these trends was derived and hung from the water bottom for a spatially variant δ model. Following the δ field derivation, ε scans were performed to evaluate the significance of polar anisotropy at the far offsets through several areas. Throughout this area, it was observed that a simple and regional $\varepsilon = 2x\delta$ smooth model was a good compromise for this frontier region.

As a validation tool, sonic well-logs where plotted against the derived V_{tilt} model profiles (Figure 4-2). Although there are not many available wells in this particular area, and these tend to be relatively shallow, the displays at least provided a first order quality control of the obtained results.

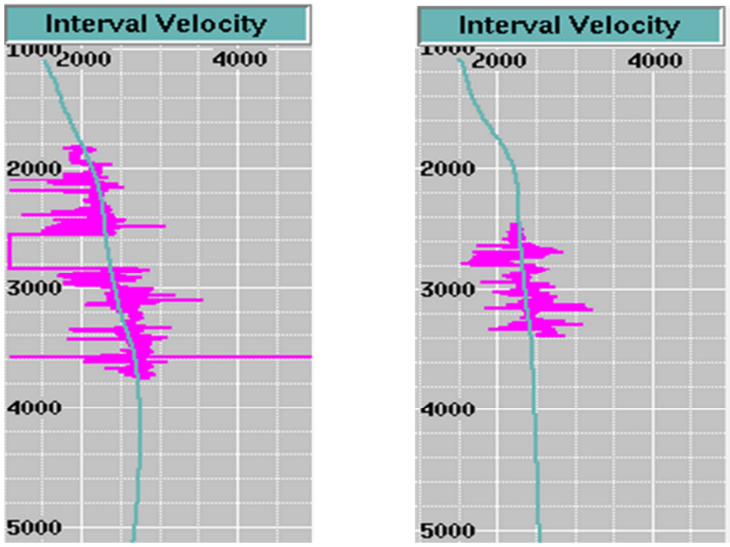

Figure 4-2. QC display of two well locations inside the test area. The blue line shows the derived Vtilt, while the magenta curve represents the sonic log for the corresponding location.

In order to derive the tilt and azimuth models for a tilted polar migration, a picking routine was used to measure attributes of all seismic events from a given stack image. This was done by decomposing all tilts and azimuths into inline and crossline direction slopes that were then preconditioned and input to the migration.

To follow are examples of the distribution of the previously described parameters (Figures 4-3 through 4-7):

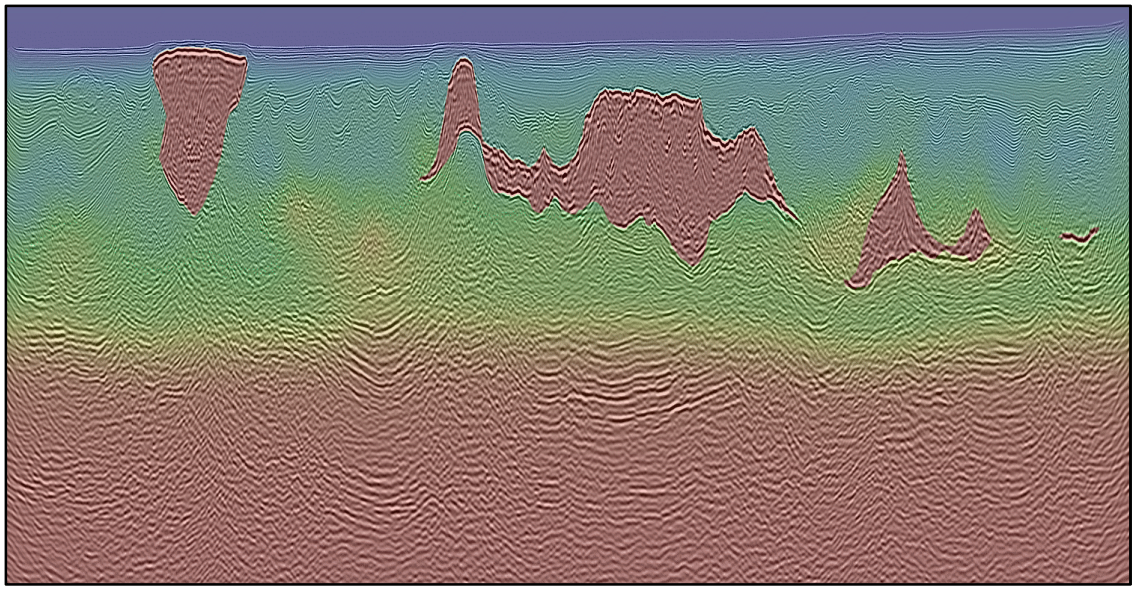

Figure 4-3. Tilt velocity overlaid on regional seismic stack image. The velocity ranges from approximately 1,500 m/s (blue) to 4,500 m/s (red).

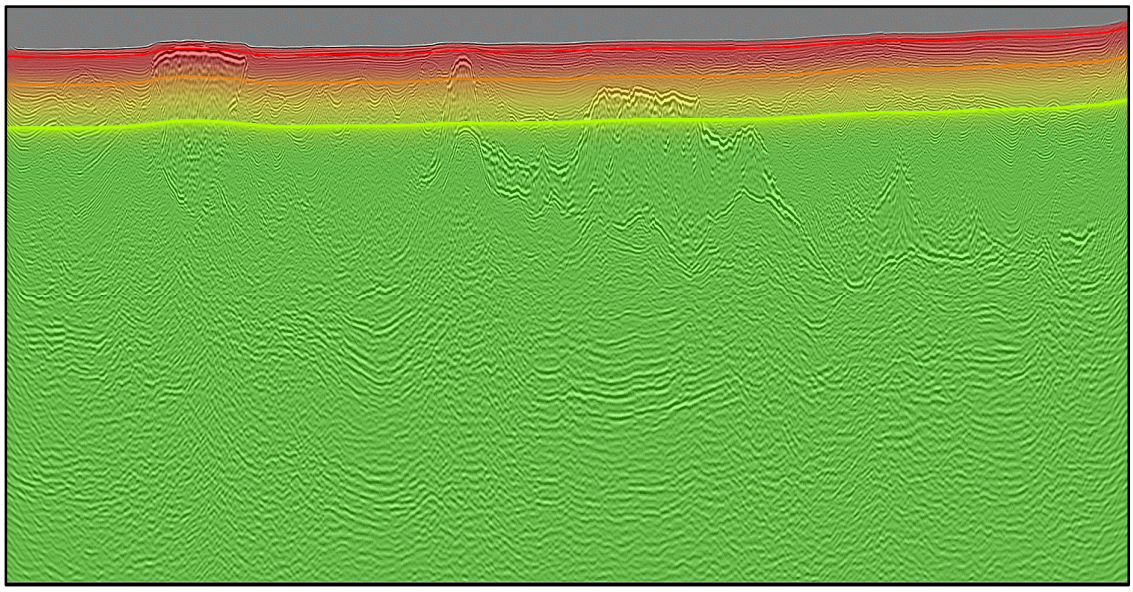

Figure 4-4. Thomsen's δ parameter overlaid on regional seismic stack image. The δ model for this survey ranged from 0 to 6% (green).

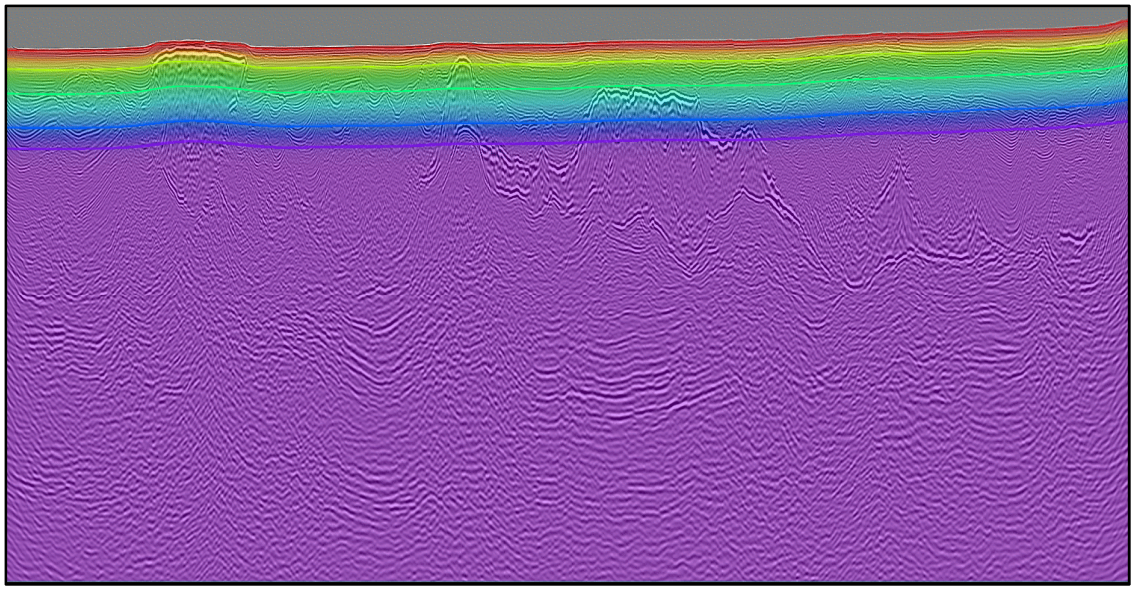

Figure 4-5. Thomsen's ε parameter overlaid on regional seismic stack image. The ε model for this survey ranged from 0 to 12% (purple).

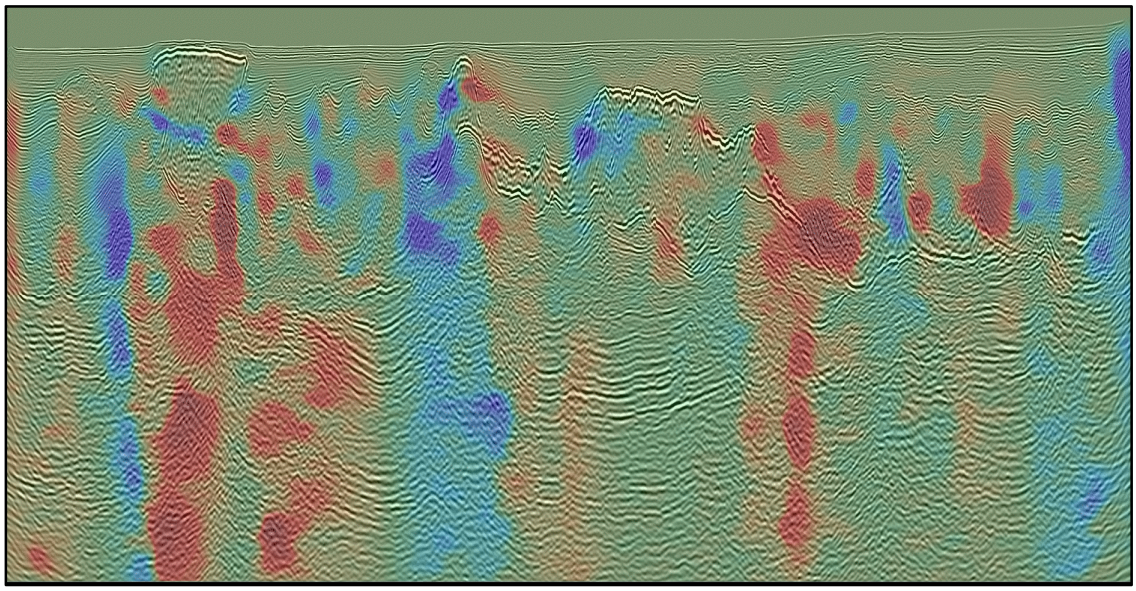

Figure 4-6. Inline slope field overlaid on regional seismic stack image. The slope values (dz/dx) were allowed to vary from -2 (blue) to +2 (red), or +/- ~63°.

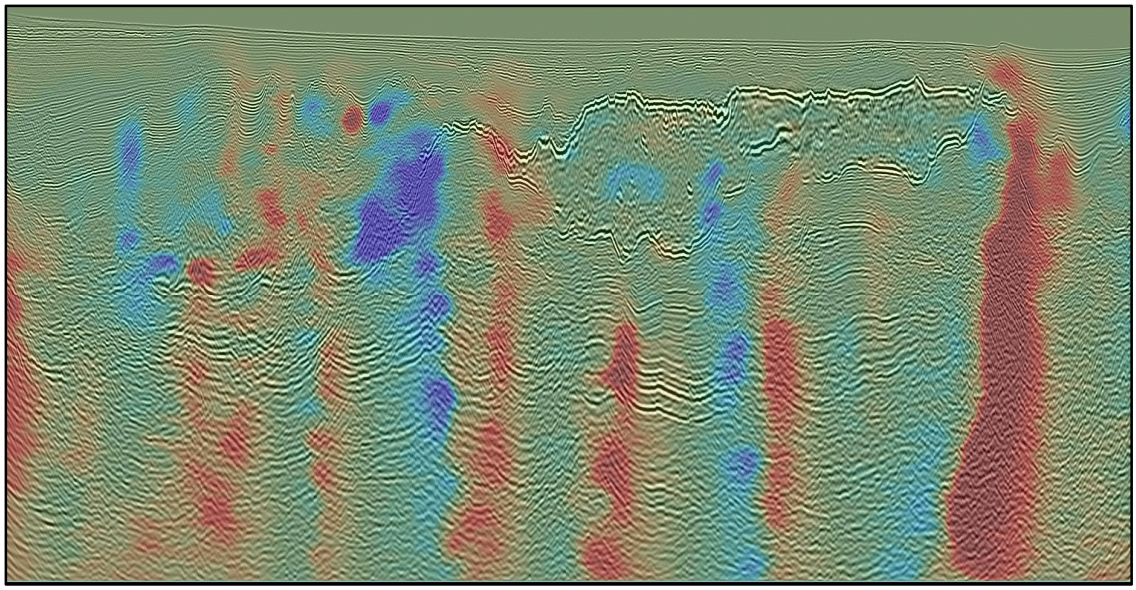

Figure 4-7. Crossline slope field overlaid on regional seismic stack image. The slope values (dz/dy) were allowed to vary from -2 (blue) to +2 (red), or +/- ~63^{o}.

4.1.4 Angle-domain Imaging

Angle-domain imaging offers an intuitive way to decompose and analyze imaged data that is also natural for shot migration algorithms. While these migrations are more computationally intensive, they do not suffer from artifacts associated to multipathing and complex geology, unlike most ray-based methods (Biondi, 2007), and therefore present more accurate images of the subsurface. The basic idea in angle-domain imaging is to group the migrated images as a function of opening angles and depths for all image locations.

For this study, opening angles will be measured as the angle between the incident source Poynting vector (Dickens, et al., 2011) as an estimate of the propagation

direction for the dominant incident wavefield and the cross-product between the two slope fields, which is the normal local to the bedding (Figure 4-8).

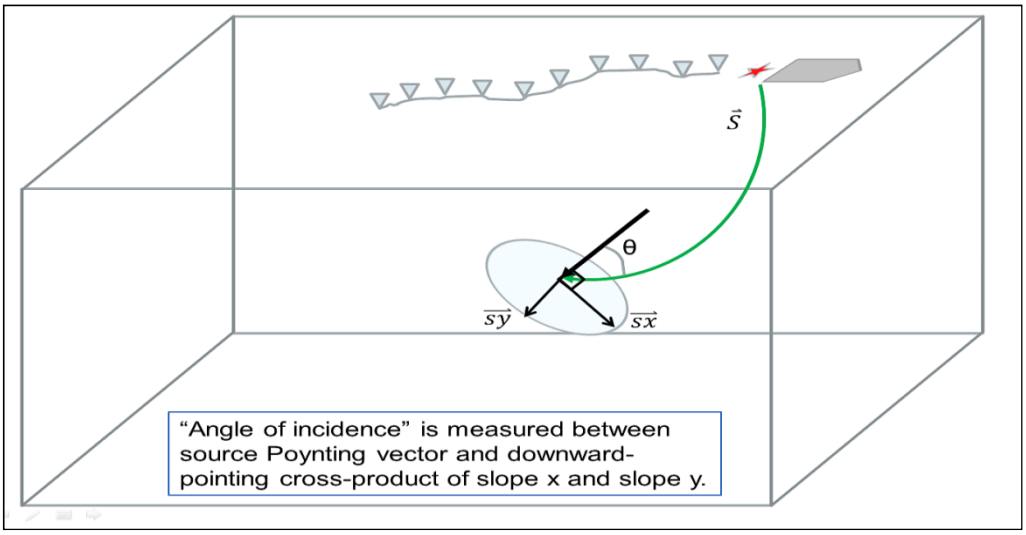

Figure 4-8. Sketch illustrating the opening angle or incidence angle definition used throughout this study.

These angles can also be subdivided into sectors associated with different azimuth ranges that exist within a given dataset. Note that these imaged azimuths are defined according to the angle between the measured projection of the outgoing source Poynting vector (at the reflector) into the x, y plane, referred to the inline, *i.e*. the sail-line direction (Figure 4-9) of the survey. This is different from the azimuths in the shot-record domain, that are usually defined as a function of the angle between the surface-vector joining a given source-receiver pair.

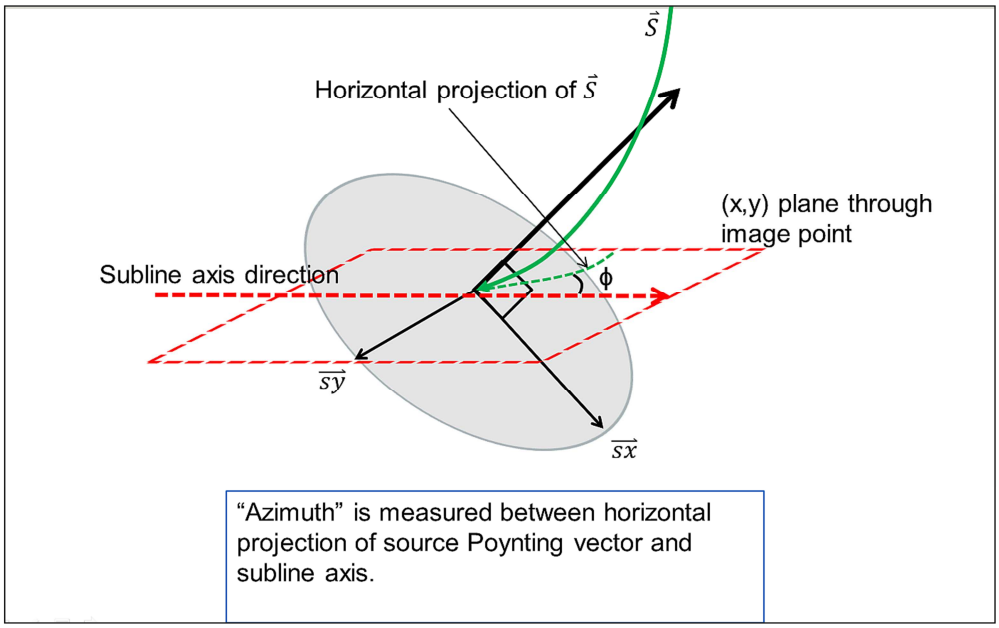

Figure 4-9. Sketch illustrating the azimuth definition used throughout this study.

It is worth mentioning that the reverse time migration algorithm used for this study allows the user to simply select a range of opening angles and azimuth sectors, into which all migrated traces will be then binned during migration. This is a different approach from other studies, like Zhu *et al*. (2010), where the division or binning of the data for two overlapping land surveys into several azimuth sectors happens pre-migration.

While marine wide-azimuth acquisitions still have a limited range of azimuths inherently acquired in the data, they provide significantly more azimuthal information than a somewhat equivalent narrow-azimuth dataset. To put things in perspective, the wide-

azimuth acquisition that generated the dataset used throughout this study, had approximately 7 km streamers on two of the four boats, with these particular two recording vessels being 3.6 Km. apart. If we simply ignore the crossline length of each spread, the angle between one of the recording vessels and the end of the central streamers on the opposite boat comes out to approximately 30 degrees, which is an increase of at least 3 to 6 fold in azimuthal coverage, compared to common narrow-azimuth acquisitions. This increase naturally results in events being recorded through a wider variety of angles and azimuths, thus providing a more complete representation of seismic events that should aid the analysis of azimuthal variations throughout this study. Due to the nature of this WATS acquisition, there is an associated limitation in opening angles and azimuths that are recorded in the data. Though WATS data contains significant additional azimuthal information (than the narrow azimuth towed streamer (NATS) acquisition), the associated coarse shot sampling creates gaps in the angular coverage of the subsurface. A classic marine narrow-azimuth survey might have a 37.5m sail-line shot spacing, while a typical WATS geometry will have a somewhat equivalent 150m shots pacing. Note that the sparse shot sampling does not necessarily limit the ability to record certain angles, but it will affect how often these can be recorded.

Narrow opening angles can only be recorded by relatively small source-receiver half-offsets. At shallow depths, this can be challenging, as receivers are always placed a certain distance away from the source. However, narrower angles can be acquired at

deeper depths, because for the same half-offset, deeper events will correspond to reflections from smaller angles.

Figure 4-10 shows how deeper events can still provide the same angles, as long as the half-offset distance increases proportionally for a simple 2D case containing only flat constant velocity layers. This is demonstrated by the dark blue and red ray pairs. Also, an example of narrower angles being recorded for deeper events for a given half-offset can be shown by comparing the dark blue and cyan rays.

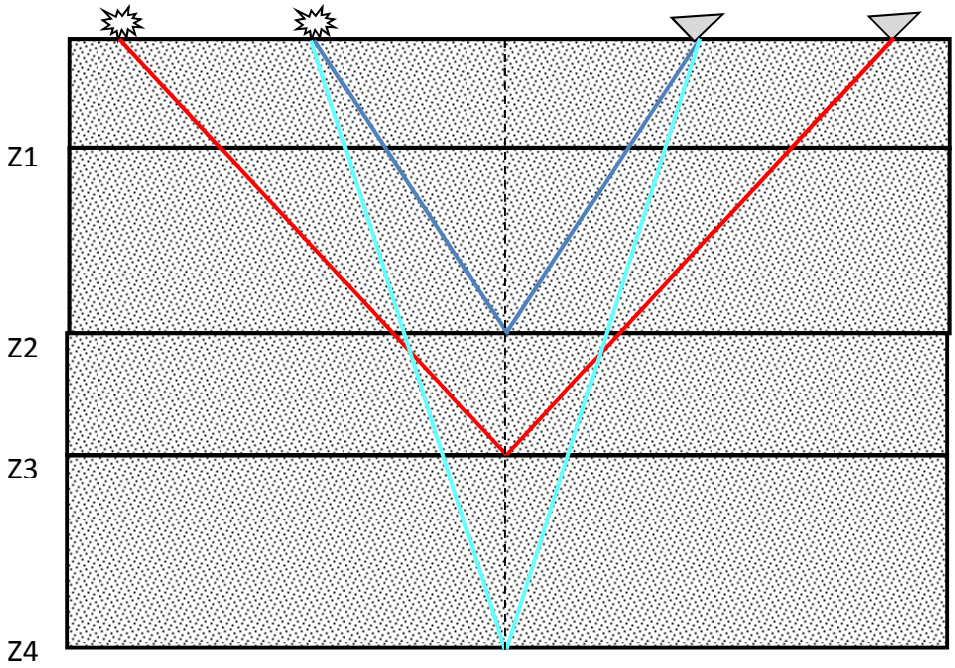

Figure 4-10. Simple sketch of a constant velocity four layer half-space. The red, blue and cyan lines represent straight rays for different combinations of reflectors and source-receiver offsets.

If each of the layers in Figure 4-10 were assigned different velocities, and assuming that the same red, cyan, and dark blue rays were traced following Snell's law for specular reflections, it would result on the sketch presented on Figure 4-11. This figure provides a more realistic sketch of how the energy could propagate throughout heterogeneous media.

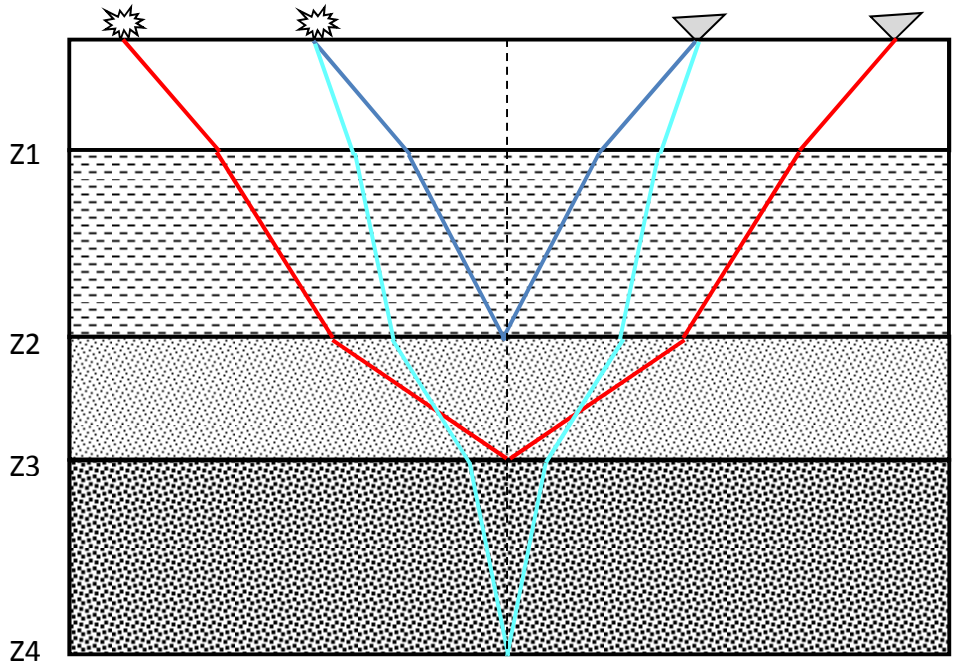

Figure 4-11. Sketch of a variable velocity four layer half-space. For this particular case, the velocity is constant within each layer but it decreases in the second layer, increases for the third and decreases again for the fourth one. The red, blue, and cyan lines represent approximations of rays for different combinations of reflectors and source-receiver offsets.

While the geological model in Figure 4-11 introduces complexity by varying velocity through the media, the one in Figure 4-12 adds to it by incorporating dip, or structure. In the presence of dipping reflectors, greater source-receiver offsets are required to record the same opening angle deeper and along the same layer boundary; this can be demonstrated by comparing the red and dark blue rays.

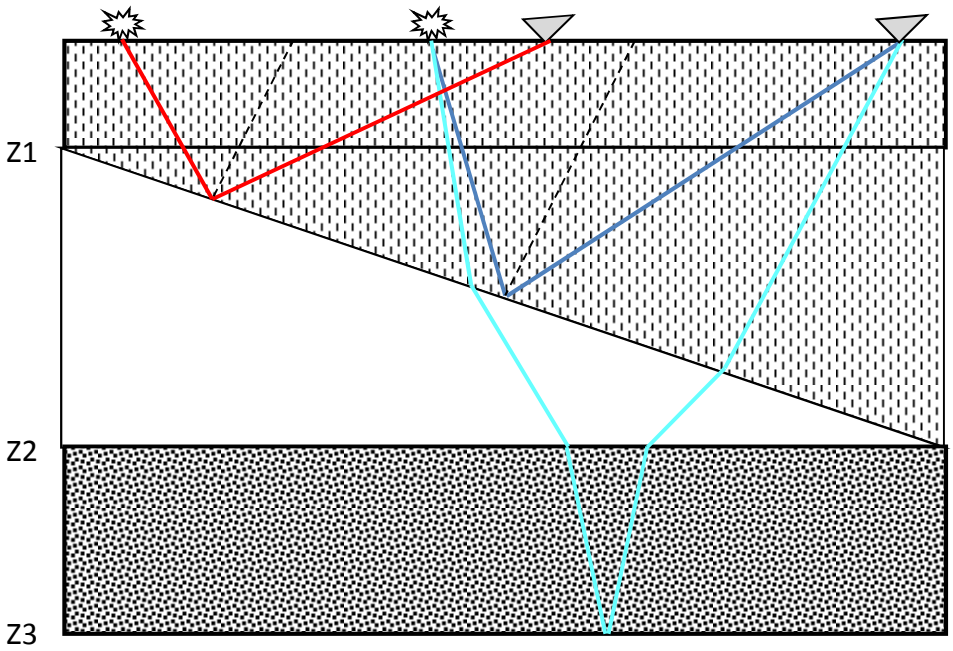

Figure 4-12. Similarly to the previous figure, this sketch presents of a four layer half-space but introducing a dip component at the boundary between the second and third layers. Again, the red, blue and cyan lines represent three ray pairs for different combinations of reflectors and source-receiver offsets.

Interestingly enough, for the same half-offset a more complex ray (cyan) can be sketched, showing how radically differently the retuning leg of this ray can be, as it travels through more complex media. Note that these are basic concepts that are almost intuitive, but their understanding will be key, when trying to understand how a given target is being imaged in the angle-domain.

Finally, working with azimuth-sectored angle gathers provides insights into which particular azimuths or reflection angles are predominately contributing to construct the image of a particular seismic event. Assuming that the migration velocity model is accurate and that the media is homogeneous and strictly isotropic, dividing these images into azimuth sectors will only show how the energy is being divided throughout the sectors, with no differences between the moveouts of a given seismic event for each azimuth. However in azimuthally anisotropic media, the partitioned data ought to show recognizable patterns varying across several azimuth sectors, depending on the particular orientations of regional stresses, fractures and errors throughout the data.

4.1.5 Migration Run Parameters

Using the legacy tilted polar anisotropic models, a subset of approximately 800 km^2 was migrated with RTM. For this study, the RTM output was designed to be decomposed into 20 opening angles ranging from 0 to 60 degrees, every 3 degrees for each azimuth sector. These parameters were selected keeping in mind the size and memory

requirements of the resulting 5D dataset, while maintaining reasonable sampling of azimuth and opening angles for the target migration.

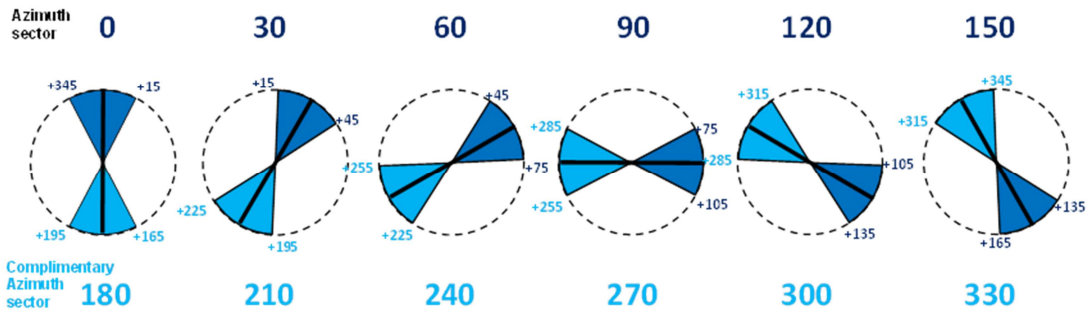

Figure 4-13. Diagram of the 6 azimuths sectors to be used on this study. Each sector consists of two complimentary 30 degrees subsectors.

Regarding azimuths sectors, the data was binned into 6 sectors of effectively 60 degrees as sketched in Figure 4-13. Note that each sector is composed of a range of up to 30 degrees of azimuths and their complementary opposite subsector. For example, the azimuth sector labeled as 30 degrees includes a subsector of azimuths of 15 to 45 degrees and its complementary subsector ranging from 195 to 225 degrees.

Figure 4-14 illustrates the amount of moveout variations between for a shallow ADCIG analysis location. It is worth pointing out that for this example, some events appear to be imaged with velocities which are both too fast and too slow, for different azimuth sectors.

Note that, to some extent, smearing of events will happen on these outputs due to the relative sparse sampling, but the analyses should still be valid since the targets of this study are regional azimuthal velocity variations on relatively long wavelength data.

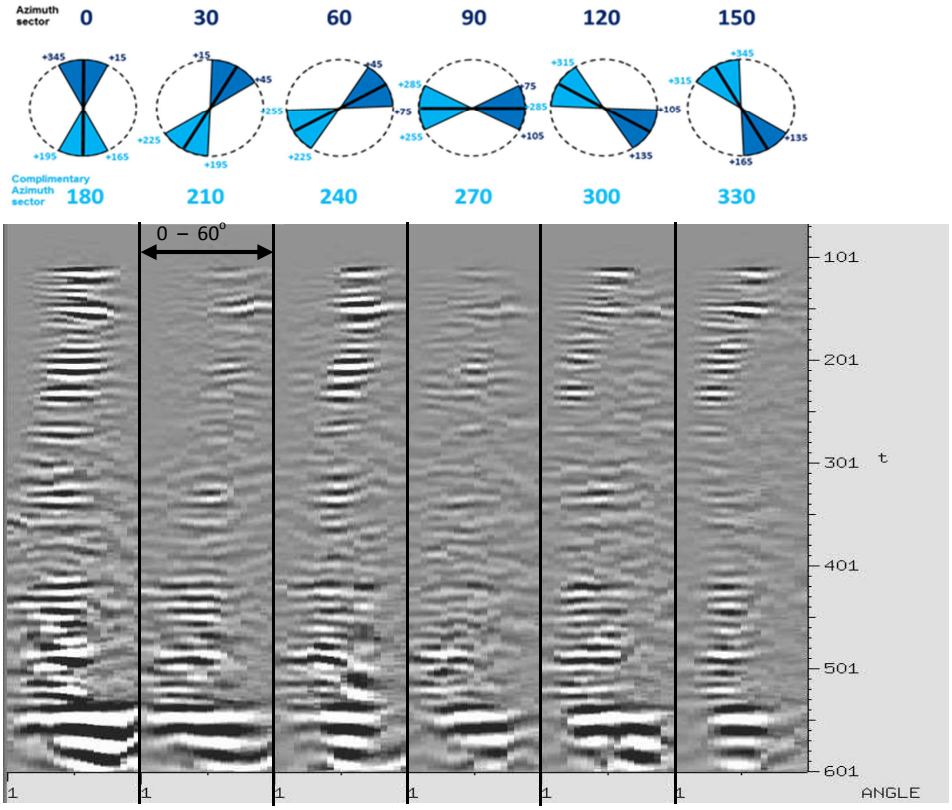

Figure 4-14. Example of (1) RTM azimuth-sectored ADCIG analysis location.

Other than the defined output bins and sampling for the opening angles and azimuth sectors, additional migration parameters like: maximum frequency, half-aperture, output depth, spatial sampling, and vertical sampling were chosen after evaluating the objectives, data specs and geologic scenario for this study. A relatively low maximum-frequency of 15Hz was chosen for practical reasons, and because regional azimuthal

variations are expected to gradually vary throughout the dataset. To define the inline and crossline half-apertures and well as the maximum output depth, an imaging box of 14x14x12km around each shot was selected, effectively making the inline and crossline half-aperture equal to 7km and limiting the output to 12km of depth. These values were based on the dips and locations of potential target events and their surroundings. Finally, the spatial and vertical sampling rates of all outputs were selected in accordance to the aliasing criteria for 15Hz, this resulted in gathers every 50m along inline and crosslines, with each trace vertically sampled at 20m.

4.2 Azimuthal Variations

Now that the migration details have been covered, this section on azimuthal variations will describe the main expected sources of azimuthal variations and how they should affect the data.

4.2.1 Seismic Scale Considerations

Since this study will focus on relatively low frequency PSDM images, the seismic wavelength will be in the order of hundreds of meters. Contemporary reverse time migrations on the GOM target relatively low maximum frequencies, generally between 15 to 20Hz, for subsalt plays. Throughout the test area, the derived velocities ranged from roughly a water velocity of 1,500 m/s to a salt velocity of 4,500 m/s. This velocity

range corresponds then to wavelengths of approximately 100m near the water bottom, up to 300m through salt bodies for a frequency of 15Hz. Therefore, only regional scale azimuthal variations will be targeted in this study, as these tend to be much larger and more consistent than local anomalies and thus, considerably more noticeable over the longer wavelength data and relatively sparse azimuthal sampling.

4.2.2 Types of Azimuthal Variations

Azimuthal velocity variations at a given image point can be caused in several ways. Throughout this study the goal is to identify and analyze azimuthal variations that are regionally consistent and geologically related, rather than anomalous local patterns due to inaccuracies in the migration models, or their relatively low resolution. To follow are descriptions and examples of the main potential sources of these variations.

4.2.2.1 Heterogeneity

If we define heterogeneity as a function of how non-uniform a material is, geologic heterogeneity will be then related to the varying nature of rocks within a given geologic unit. In complex geologic regimes, a particular arrangement of these units could easily produce an azimuthal variation signature. For example, if the model displayed in Figure 4-15 is representative of the media for layers A and B, no azimuthal variations should be observed from a ray travelling from East to West or its reciprocal ray, travelling West to

East. However, if the true velocity of the media is the model presented in Figure 4-16, but the data are migrated with the first model (Figure 4-15), the incorrect lateral velocity gradient in Layer B will result in an anomalous azimuthal moveout, due to erroneous velocities in the East portion of Layer B.

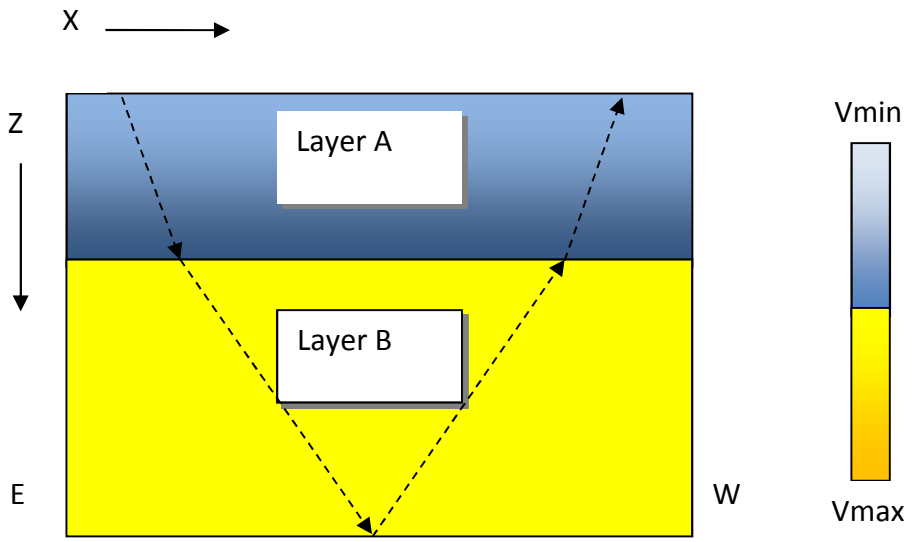

Figure 4-15. Simple two layer model, where color indicates the velocity of the medium and dashed arrows indicate a sample ray-path. Note that there is a vertical velocity gradient for Layer A, while Layer B has a constant velocity. For simplicity all rays were drawn with straight lines.

Not accounting for heterogeneity in the case of lateral or vertical velocity changes, whether it is related to contiguous but varying rock types, facies changes along a particular unit, unconformities, or other geologic processes, could introduce significant erroneous azimuthal variations throughout the data.

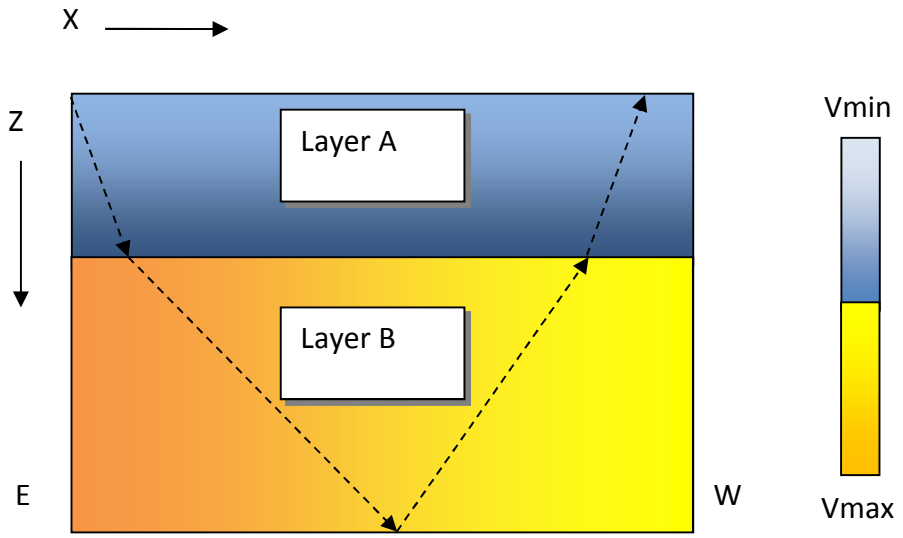

Figure 4-16. Two layer model, where color indicates the velocity of the medium and dashed arrows indicate a sample ray-path. Note that there is a velocity gradient for each layer, for Layer A the velocities vary vertically, but for Layer B they only vary horizontally, but for simplicity all rays were drawn with straight lines.

When migrating data, the expectation is that the velocity models used in the migration will have enough detail to account for the resolvable heterogeneity at the targeted seismic scale. This could be validated by inspecting the migrated CIG's and checking that there is minimal moveout left throughout the data in areas of reliable data quality.

4.2.2.2 Dip

Tilted layers associated with dipping seismic events are also an example of heterogeneity that can cause azimuthal variations. This key case will be discussed separately for a better understanding of its effects.

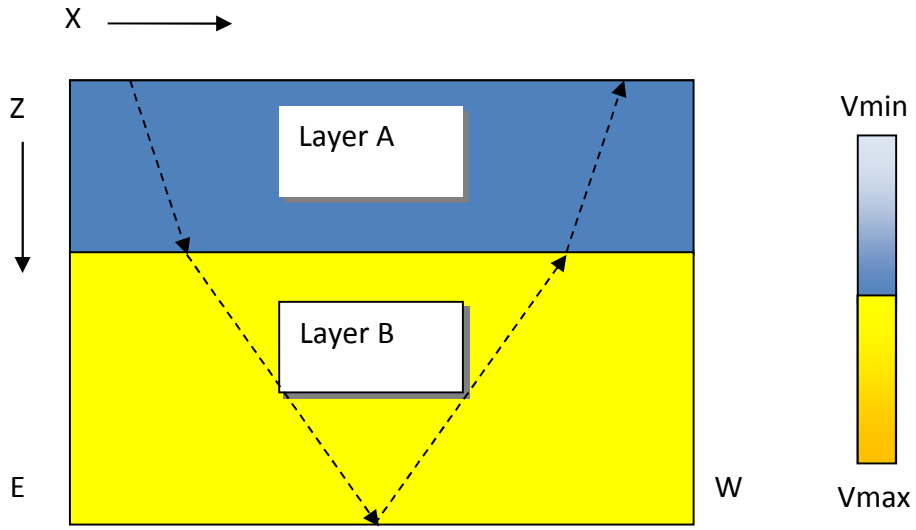

Figure 4-17. Basic two layer model, where color indicates the velocity of the medium and dashed arrows indicate a sample ray-path. Note that both layers are flat and the velocity for each layer is constant.

If the dip of the events is not accounted in the migration models, timing errors will be introduced and the resulting migrated images will show artificial azimuthal variations. The trivial two layer homogeneous model displayed in Figure 4-17 consists of flat layers of different thicknesses, while the model in Figure 4-18 has Layer B dipping at approximate 45 degrees. If data that agrees with the model in Figure 4-18 is migrated

without accounting for the dipping layer, it will yield an apparent azimuthal velocity variation related to wrong reflector dip and velocity for Layer B.

The migration velocity model should be derived with such resolution that dipping layers of imaged events are resolved, at least at the selected seismic scale. This will avoid dip errors that could end up being interpreted as azimuthal variations.

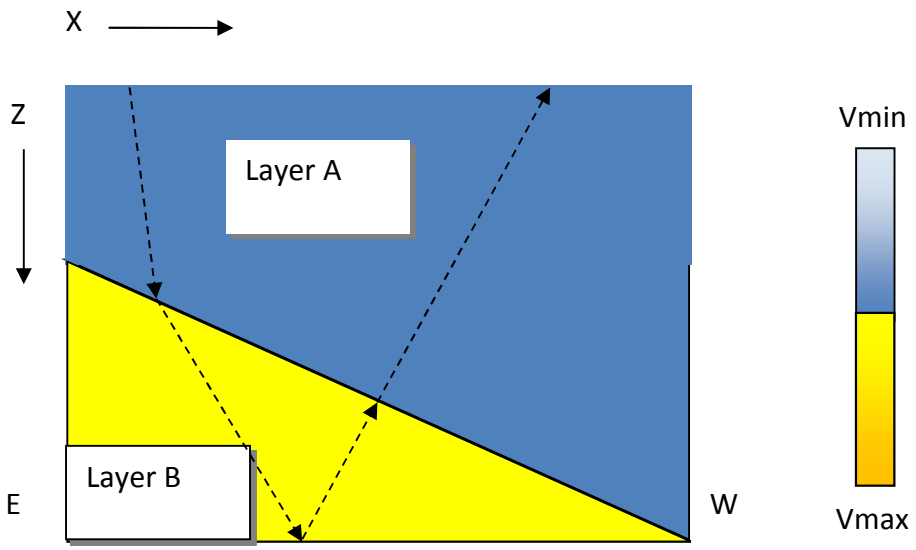

Figure 4-18. Two layer model consisting of a constant velocity flat layer down to a dipping plane, where color indicates the velocity of the medium and dashed arrows indicate a sample ray-path.

4.2.2.3 Anisotropy

The third and perhaps most interesting factor that could highly influence azimuthal patterns, is velocity anisotropy or directional velocity dependence. Intrinsic and extrinsic anisotropy, or their combination, can introduce azimuthal variations depending on how they vary through the data. For this study, intrinsic anisotropy will be considered as the

anisotropy component related to internal rock properties like certain symmetry in their crystal structure, while extrinsic anisotropy will be the component caused by of external factors, such as regional stresses or fractured media.

Since all migrations for this study used tilted polar anisotropic models and its respective propagator, only tilted polar anisotropy and azimuthal anisotropy will be discussed in terms of azimuthal variations. Note that while the velocity discrimination along the tilt axis will be the greatest correction towards properly imaging a given event, δ and ε will act as a second order adjustment. Finally, azimuthal anisotropy is typically estimated to be smaller in magnitude than polar anisotropy (Michelena *et al*., 2011). In this case, it is also expected that the observed azimuthal effects will be relatively smaller than its tilted polar counterpart.

4.2.2.3.1 Tilted Polar Anisotropy

Just as in the vertical transverse isotropy case, intrinsic anisotropy in tilted layered media can create velocity anomalies of waves travelling through it, referenced to a tilted axis of symmetry instead of the vertical axis, which typically corresponds to flat finely layered media. Figure 4-19 shows a simple example of tilted polar anisotropic media, in which the velocities along perpendicular axes A and B differ, due to the presence of a sequence of thin tilted layers. This media is effectively less compliant or slower for waves travelling across the thin beds, or along Axis A.

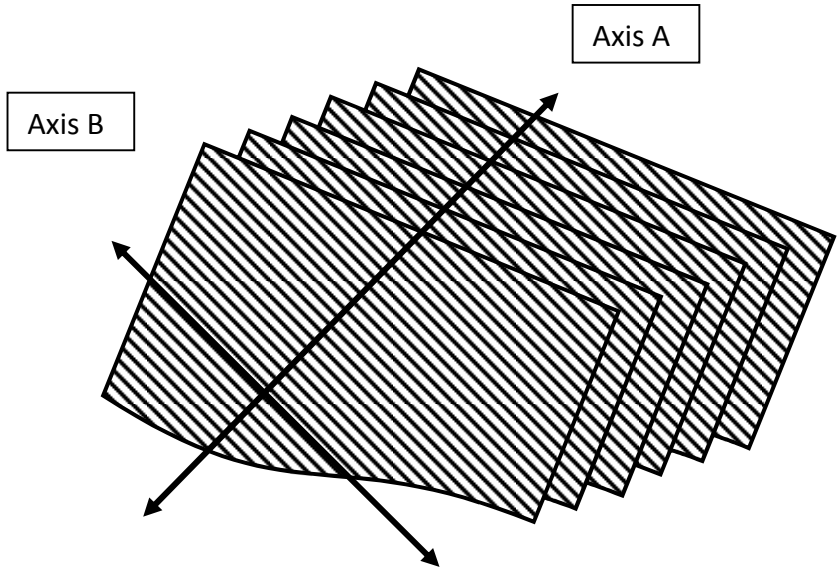

Figure 4-19. Illustration of tilted polar anisotropic media, where each panel represents slices of thin tilted layers. Axis A goes across a sequence of contiguous thin beds, while Axis B goes along the dipping thin beds.

If done correctly, compensating for tilted polar anisotropy itself will not introduce azimuthal variations effects on truly tilted polar anisotropic media. However, errors in the anisotropic migration models could introduce an azimuthal bias. While very simple and smooth δ and ε models will not affect azimuthal variations, introducing a high level of detail into these models, when incorrect, could lead into local anomalies that will have an impact on the positioning and moveout of events for different azimuths at a particular image location. Likewise, tilt fields for a given tilted polar anisotropic migration will also impact the position and moveout of data. But again, depending on how widespread errors in these models are, the migration results at a particular

erroneous location will have an imposed azimuthal biased or not, with respect to the surrounding data. Note, that if smooth anisotropic models like the tilt fields are consistently wrong through a particular region of the data, no azimuthal bias due to the erroneous tilt models would be observed, since all azimuths will be affected by the same error, making this a constant bias for all the data.

4.2.2.3.2 Azimuthal Anisotropy

Extrinsic anisotropy related to differential regional stresses, or preferential alignments of fractures or cracks, can generate azimuthal variations dependent on rock properties of a particular area by causing the velocity of a layer to deviate, depending on the azimuthal direction for which a given energy packet is travelling. Figure 4-20 presents an example of azimuthally anisotropic media. In this case, a set of fractures for a 3D cube of a given single rock material will change the originally isotropic velocity of the medium to be dependent on the associated overall trend of fractures or cracks within the volume (Thomsen, 2002). This happens because a P-wave travelling along the fracture direction will have a faster velocity than if it were moving across the fractures (Figure 4-21). As the waves interact with the media, a given packet travelling from East to West will cut across all fractures, which will effectively slow the waves due to the higher amount of void space, while waves moving in the orthogonal direction will be less affected by the presence of fractures.

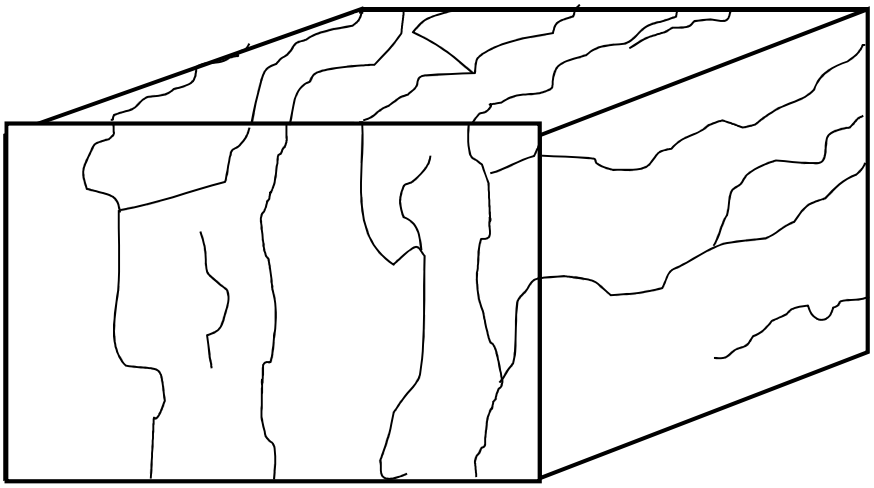

Figure 4-20. Illustration of a fractured cube of originally isotropic media. Note that the fractures were intentionally drawn following a general trend that will simulate a more realistic case.

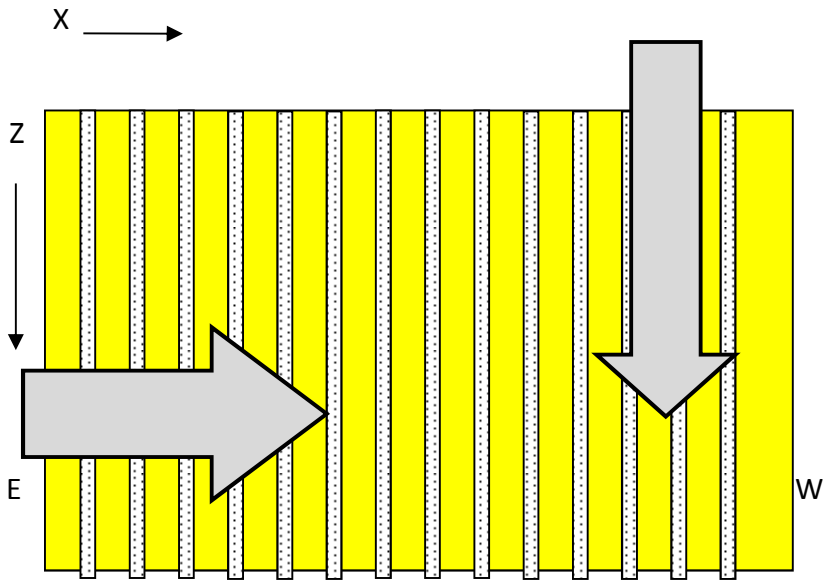

Figure 4-21. Diagram of homogeneous media (yellow) with regular vertical fractures (white dotted strips). Grey arrows indicate the two extreme scenarios, where compressional waves will travel either along fractures, or across them. Also, it is worth mentioning that the arrows were purposely drawn thick, because fractures are expected to be relatively smaller than the wavefronts traveling through them.

Other type of extrinsic anisotropy supported by a plausible geological model, is the one resultant from regional anisotropic stresses, as these can change over time and will impact rock properties and the associated velocity trends with azimuth. As stated by Thomsen (2002), P-wave velocities should be analyzed in terms of elliptical variations in azimuth. This is usually done by fitting data with an elliptical model that consist of a fast velocity axis, a slow velocity axis and a reference angle; these correspond to the two main axes of an ellipse and an orientation angle shown in Figure 4-22.

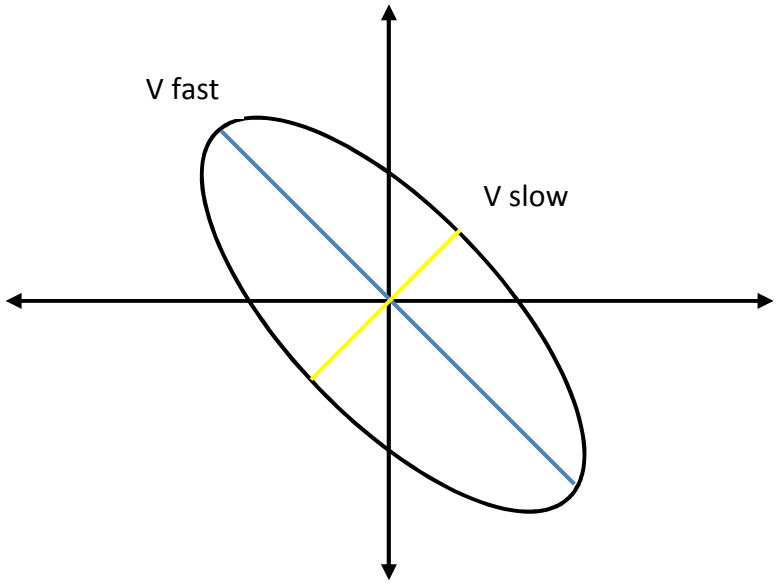

Figure 4-22. Sketch of a generic elliptical azimuthal velocity model. The slow velocity axis is displayed in yellow, while the fast velocity axis is displayed in blue. Note that the ellipse was drawn at an angle to indicate that its orientation is also a variable in the model.

Finally, orthorhombic anisotropy (Figure 4-23) presents a symmetry that is perhaps more representative of real world geology. While it can account for intrinsic anisotropy in sediments, it also takes into account extrinsic anisotropy sources like vertical fractures or fine layering along different axes. Note that a natural extension of this symmetry will be a tilted orthorhombic anisotropic model, as it will also account for tilted layers, similarly to how tilted polar anisotropy is effectively also an extension of the vertical polar anisotropy case. Though there are more complex types of symmetries that can potentially better describe real data in terms of azimuthal variations, this study will be limited to only the polar and orthorhombic cases referenced above.

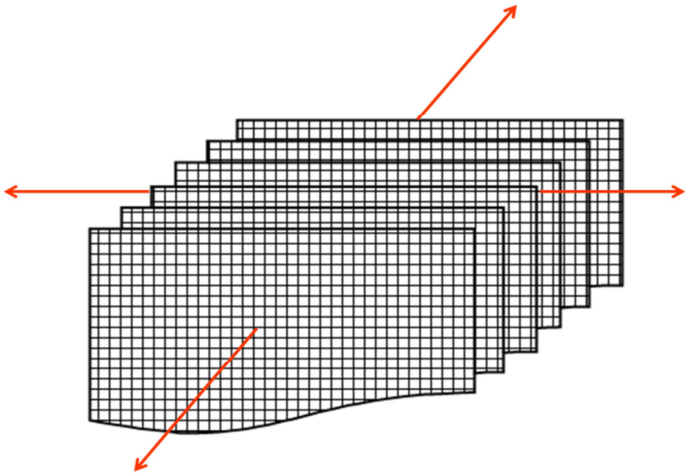

Figure 4-23. Illustration of ideal orthorhombic anisotropic media, where each panel represents slices of thin layers with evenly spaced vertically aligned fractures.

Keep in mind that part of the motivation for this study, is to investigate if there are significant azimuthal variations that will call for a higher-order symmetry system than

the tilted polar anisotropy on this type of somewhat common wide-azimuth acquisition, often used for relatively low frequency reverse time migrations.

Lastly, all of the factors mentioned in the migration and azimuthal variations sections will greatly influence the azimuth-sectored angle gather results generated for this study. Therefore, the understanding of these aspects, before moving into the data analysis section, was considered to be a key.

4.3 Data Analysis

The goal at the beginning of the data analysis phase will be to quickly iterate through a subset of the data and derive an applicable workflow that would aid the understanding of azimuthal variations and their severity for a particular geologic scenario. Afterwards, this derived flow will be applied to several subsets of the test dataset in an effort to then validate how appropriate it is for different geologic scenarios.

4.3.1 Workflow Derivation

This section will explain how the workflow for assessing azimuthal variations was derived and tested. When evaluating the produced azimuth-sectored ADCIG's, it became clear that the analysis of super-gathers containing all 20 opening angles and 6 azimuth sectors will be quite complicated due to the character changes between near, mid and far opening angles, on top of the observed azimuthal variations. Depending on the depth and dip of the target, seismic events will be imaged by contributions from a narrow or a wider set of opening angles.

Within section 4.1, the subsection on angle-domain imaging covers the basics on how opening angles vary with depth and dip. Below, Figure 4-24 shows examples of two different depth slices, one at 1.6 km and other at 3.5 km both showing a closed basin. Note that the shallower depth slice is noisy, and presents a high level of horizontal banding related to the poor angular coverage at this depth, due to the inherent acquisition design. However, as expected, the deeper depth slice is better populated, and while it is not noise-free, one is able to track seismic events all around the basin without additional processing.

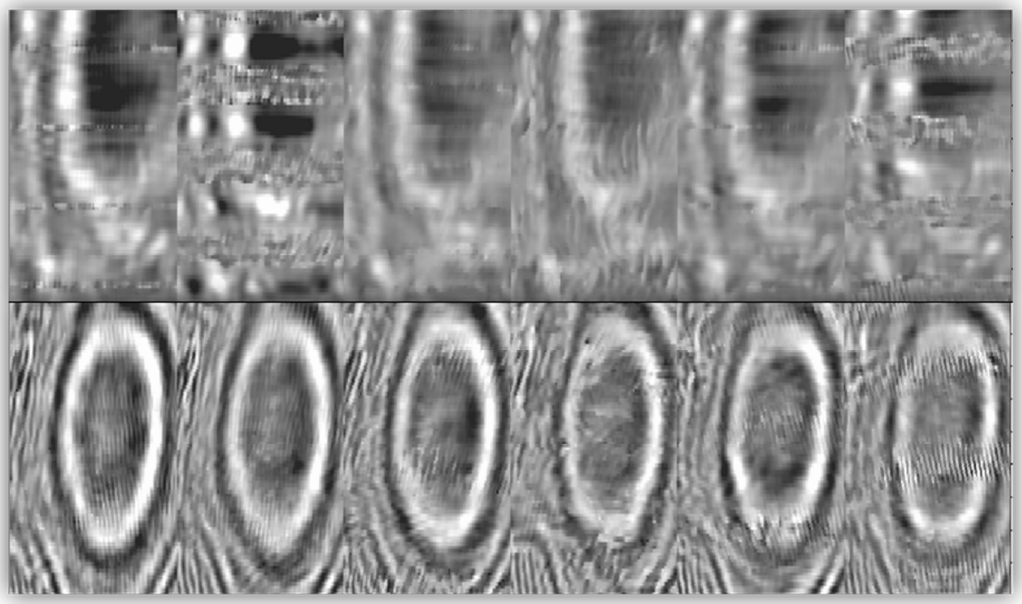

Figure 4-24. Depth slices at 1.6 km and 3.5 km of all 6 azimuth sectors for a single opening angle of 30 degrees.

An important point, is that by limiting the analysis to a certain opening angle that is both well populated, and possessing decent signal-to-noise ratio at the target level, it was possible to carry meaningful tests in an efficient matter, by minimizing anomalies not associated with azimuthal variations and processing a smaller portion of data. Also, this study focused on data from relatively wider opening angles, since narrow angle data will not have significant azimuthal sampling.

While working with a single opening angle but all 6 azimuths, common-angle azimuth gathers (Figure 4-25) were constructed by simply extracting all traces contributing to the selected angle bin, and sorting them so that for each location there is effectively a gather consisting of 6 traces, one per corresponding azimuth sector.

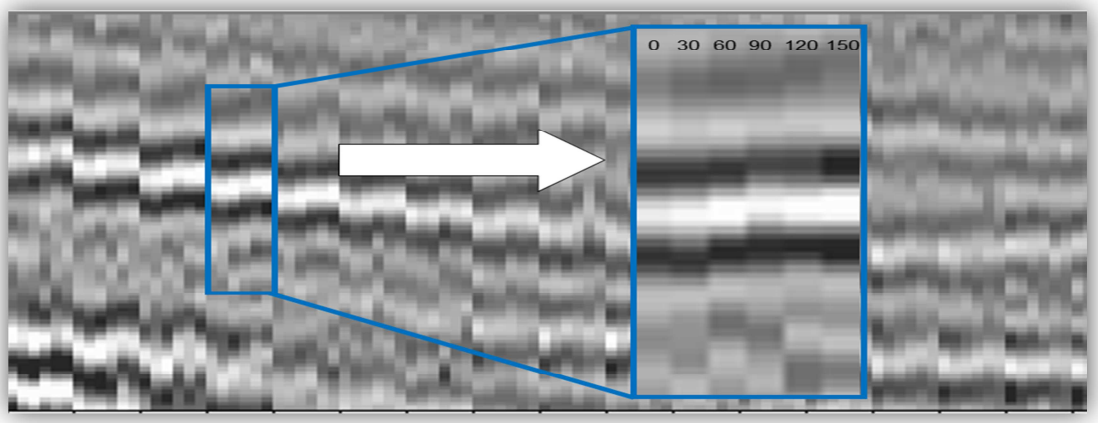

Figure 4-25. Example of a set of azimuth gathers reconstructed by selecting only contributions from the opening angle bin centered around 30 degrees.

4.3.1.1 Angle Gather Preconditioning

Several processing procedures were applied in order to aid the detection of regional azimuthal variations in moveout throughout the data. The applied processing can be divided into three categories: denoising, amplitude balancing, and sorting. Note that these procedures were parameterized in such a way that the moveout patterns of the primary energy in the azimuth-sectored CIG's were not altered, as this could bias the results of this study. Moreover, all preconditioning steps were applied, in order to aid the tracking performed by the cross-correlation algorithm, since this process heavily relies on wavelet character differences on a trace by trace basis.

4.3.1.1.1 Amplitude Balancing

A somewhat mild ensemble balance was used to better balance the amplitudes of traces across the different azimuth sectors for all image points. This process partly compensated for amplitude variations with azimuth resulting from limited data acquisition, heterogeneity, anisotropy, illumination differences, etc.

This type of amplitude balancing was achieved by selecting a relatively short depth window and only balancing amplitudes across single gathers composed of the six different azimuth sectors (Figure 4-26).

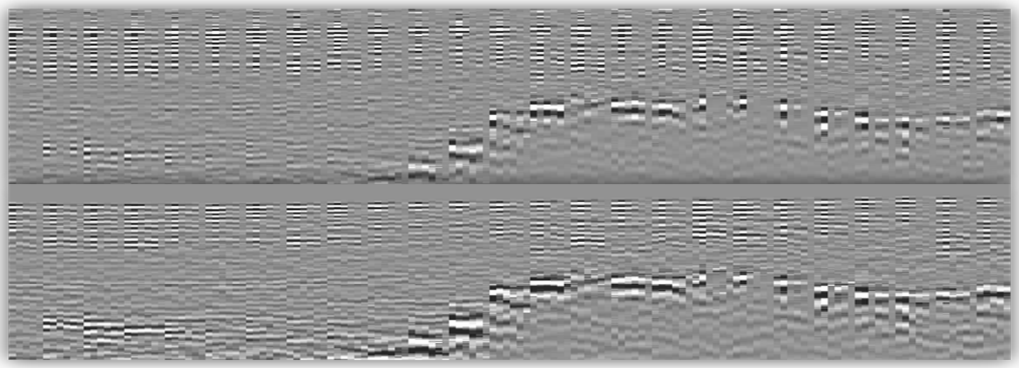

Figure 4-26. Common-angle (30 degrees) azimuth gathers, illustrating the level of amplitude balancing achieved pre-stack with post-processing.

To QC the results of the amplitude balancing, inlines, crosslines, and depth slices of subsets of the data were compared before and after the ensemble balance processing step. Figures 4-27 and 4-28 show examples of the level of balancing at the stack level.

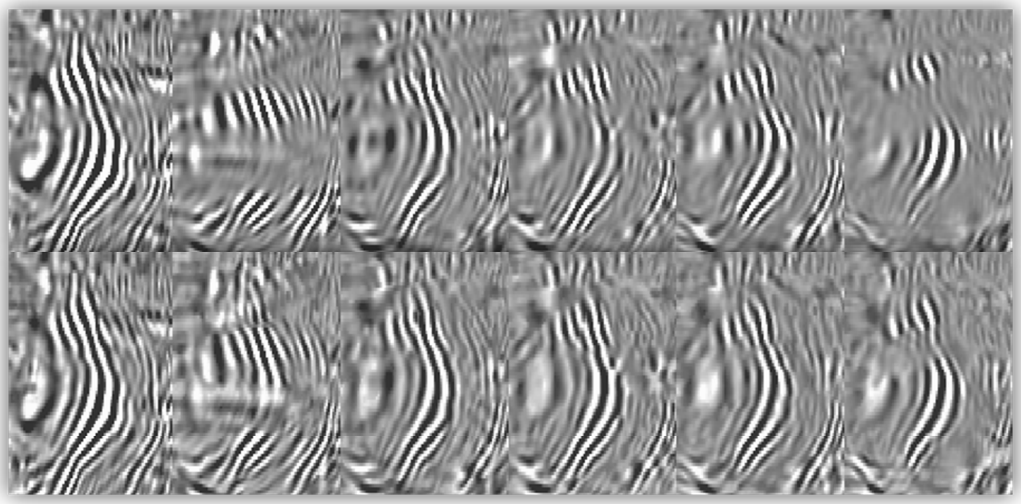

Figure 4-27. Depth slice at 5 km of depth demonstrating the level of amplitude balancing achieved with post-processing at stack level for 30 degrees of opening angle.

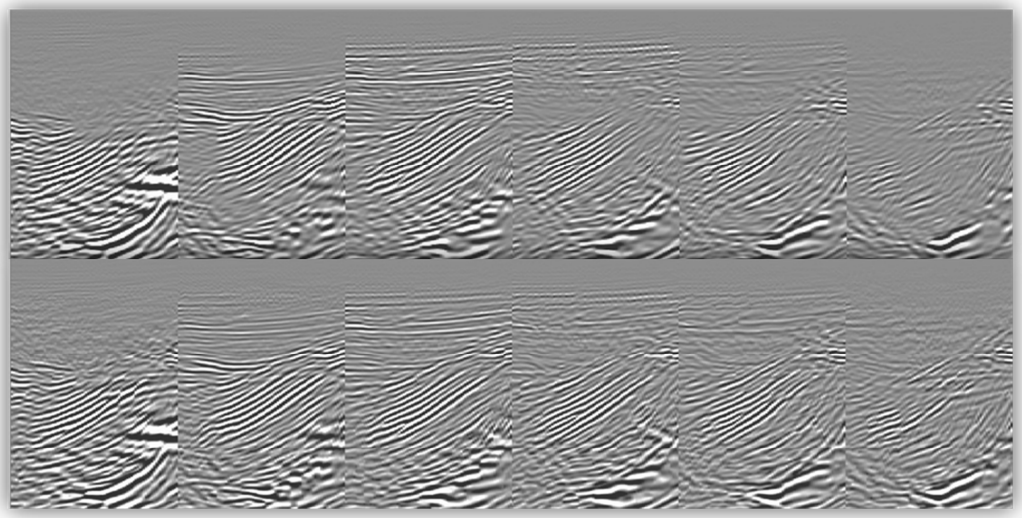

Figure 4-28. Inline example demonstrating the level of amplitude balancing achieved with post-processing at stack level at 30 degrees of opening angle.

4.3.1.1.2 Denoising

First, a lowcut wavenumber filter was applied to remove the backscatter low wavenumber RTM artifacts associated with the top of salt. This filter was parameterized to attack low wavenumbers associated with near vertical energy, taking advantage of the dip and character discrimination between the noise and the post-salt sediments, since these sediments tend to have higher wavenumber content and not be as steep.

Additionally, selective wavenumber reconstruction was performed on common-azimuth stacks. The stacks were denoised by effectively only reconstructing the main wavenumber components of an image inside the given analysis window, therefore mitigating the presence of random noise. Note that the targeted noise is assumed to be

random and thus it can be thresholded in the wavenumber domain. Examples of the stack level of denoise achieved by this technique can be seen in Figures 4-29 and 4-30.

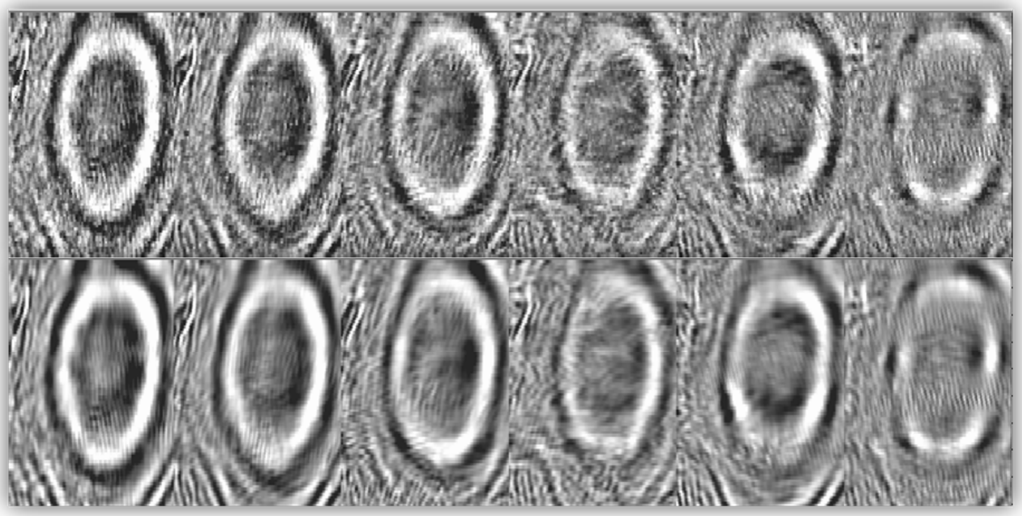

Figure 4-29. Depth slice at 3.5 km of depth demonstrating the level of denoising achieved through the selective wavenumber reconstruction on a common angle stack, in each of siz azimuth sectors. Top row is without denoising; bottom row is with denoising.

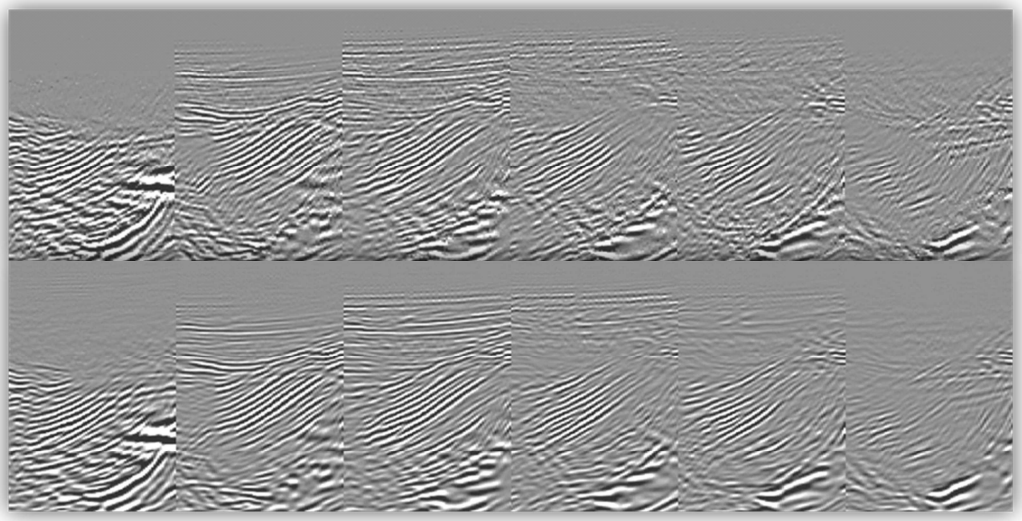

Figure 4-30. Inline cross-section example demonstrating the level of denoising achieved in each azimuth sector, through the selective wavenumber reconstruction on a common angle stack. . Top row is without denoising; bottom row is with denoising.

4.3.1.1.3 Sort Order

For the analysis of azimuthal variations, super-gathers consisting of 20 opening angles for each azimuth sector were constructed on a 50x50m grid. This implies a sort order of either INLINE/CROSSLINE/AZIMUTH/ANGLE, or INLINE/CROSSLINE/ANGLE/AZIMUTH where inline is the slowest changing axis, crossline is the 2nd slowest changing axis and so on. An example of these two types of sorted super-gathers is shown in Figure 4-31.

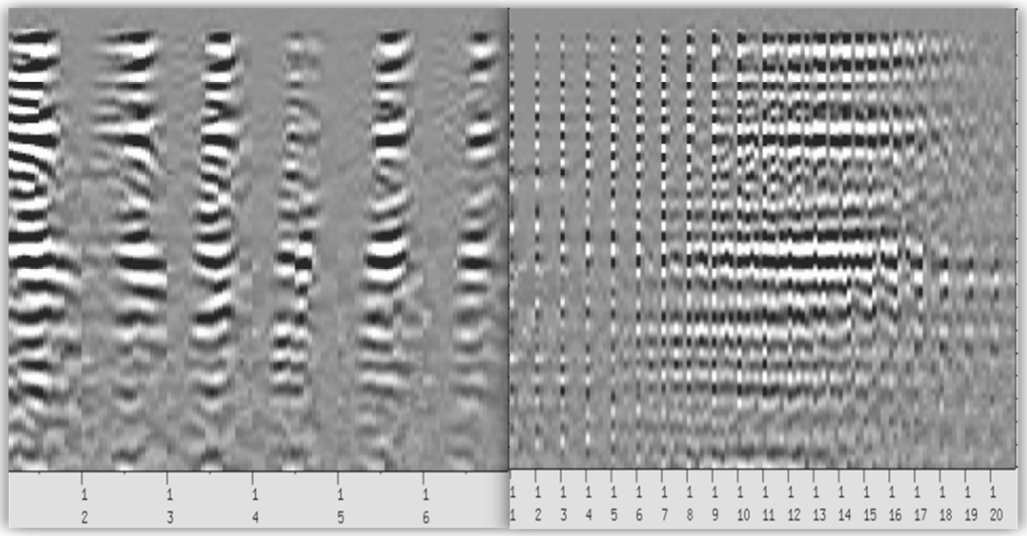

Figure 4-31. The left-hand side portion of the figure shows 6 mini-gathers, one per azimuth sector, each containing all 20 opening angles. On the right, the same traces are sorted to display 20 mini-gathers, each one consisting of 6 traces, one per azimuth sector.

Of these two types of super-gathers, the natural sorting to study azimuthal variations was thought to be the one with 20 mini-gathers, since each gather is composed then of azimuth traces. As stated previously, the analysis of these gathers proved to be cumbersome, as too many of the contributing opening angles lacked sufficient information to aid the study of azimuthal variations. Instead, a common-opening-angle approach proved to be a much simpler and efficient way of evaluating the extent of azimuthal variations throughout the study area. Depending on the depth of targeted seismic event, a range of well-populated opening angles was picked for the analysis. Within that range, only a couple of angles were then selected and checked for gaps in

angular coverage. The resulting data was then sorted by INLINE/CROSSLINE/AZIMUTH, so that gathers of 6 traces per location were created as the input going forward.

4.3.1.2 Residual Moveout Picking Algorithm

Not all azimuthal variations in real data result in moveout patterns that follow known curves or moveout equations. To pick such patterns, a cross-correlation algorithm was used to detect the deviations from the anchor trace for all input gathers, which in this case was the azimuth sector along the sail-line direction. The algorithm will track the moveout of events across traces of a given gather, by picking the closest maximum from the zero lag of the cross-correlation function, while keeping track of how many samples it has moved up or down from the anchor trace. These deviations will effectively be a measure of the vertical shifts required to flatten or align all the samples that compose a given event within a gather. Note that since cross-correlation techniques can be susceptible to cycle skipping, the corresponding lags and window lengths were optimized on a case by case basis, depending on the amount of residual moveout for the particular area of interest.

4.3.1.3 Residuals QC

In order to evaluate how good the residual picking results were, some quality control was needed. One can start by applying the measured shifts to the gathers that were

input into the cross-correlation routine, and checking if these have been reasonably flattened. By toggling back and forward between the input and the flattened gathers (Figure 4-32), one should be able to get a feel for how reliable the picked shifts are. Also, one can overlay the residual picks on top of the input gathers and evaluate how well the curve associated with the picked shifts track the moveout present on the gathers.

Another option is to input the flattened gathers into the cross-correlation picking analysis again, and verify that the new calculated shifts are close to zero, meaning that the gathers are already flat and therefore, the residuals have been measured appropriately.

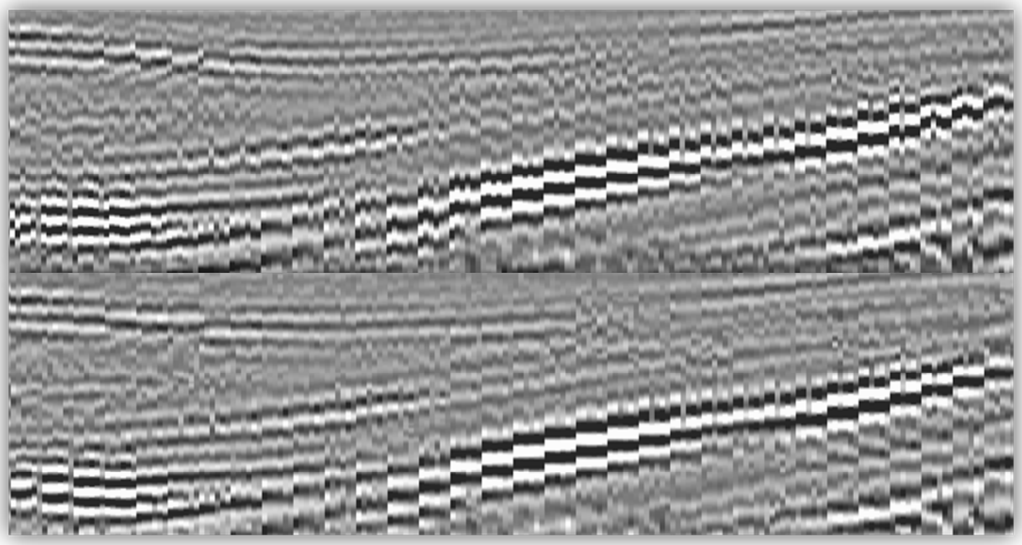

Figure 4-32. The top panel displays the azimuth gathers for 30 degrees of opening angle that were input into the cross-correlation picking routine, while the bottom panel presents the same gathers, but with the residuals applied.

Finally, by comparing the stack response of the gathers with and without the calculated shifts, not only can the advantages of a residual moveout correction can be shown by the (tentatively) enhanced imaging, but if the shifts consistently improve the alignment of the gathers, it can be used as a global measure for how well the residuals were picked.

4.3.1.4 Horizon-based Targeted Distribution of Residuals

The cross-correlation routine used throughout this study was parameterized to pick a very dense set of spatial and vertical samples. The algorithm also decides which events to pick based on attributes like peak amplitude, so that the picks correspond to significant reflections. This allows one to generate horizon surfaces representing key seismic events, and then be able to slice the volumes corresponding to the shifts at each azimuth sector with these surfaces. The ultimate goal is to generate maps of the shifts along horizons for each azimuth, since one can then limit the data analysis to particular events of interest, such as unconformities, and top and bottom of layers, where rock properties tend to vary the most.

Several horizons associated with geologic events were interpreted as needed throughout the test areas. These were then converted to maps to extract attributes along these horizons. For instance, one can not only intersect the horizon with the cross-correlation shift corresponding to a certain azimuth sector (in order to assess if

the magnitude of the moveout is significant), but one can also intersect the same surface with the velocity model or an anisotropic parameter (in order to further evaluate the nature of these azimuthal variations). Figure 4-33 shows an example of a map of raw shifts for the second azimuth sector, so negative or positive values will be associated with the amount of meters that one will have to shift the respective sample to line it up with the anchor trace.

For all the examples related to shifts from the cross-correlation picking step, the anchor trace will always be the first azimuth sector, which again represents the azimuth along the sailing direction and could be thought of as a somewhat narrow azimuth equivalent. So, if done correctly, these shifts correspond to the deviations in moveout as azimuth varies.

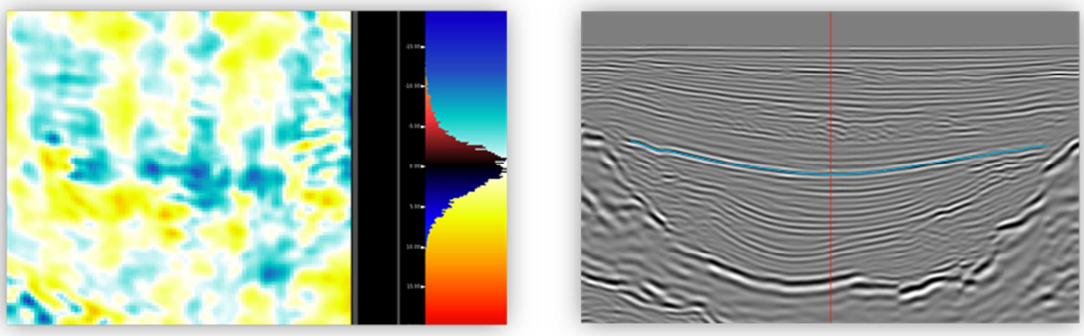

Figure 4-33. To the left, an attribute map of the picked residuals for the 2nd azimuth sector (centered around 30 degrees of opening angle) is shown with its respective color scale. Note that the scale reflects the magnitude and sign of the residual, while the histogram shows that the majority of the residuals are within +/-10m. To the right, there is a stack section displaying the location of the interpreted horizon used to generate the map of residuals.

The apparent acquisition artifact present in Figure 4-33 (and in Figures 4-34,35) is discussed further in section 4.3.3.1.

Figure 4-34 shows the same type of residual moveout attribute map, but for four different azimuth sectors. This display was thought to be useful when trying to understand how the residuals vary with azimuth along a given target horizon.

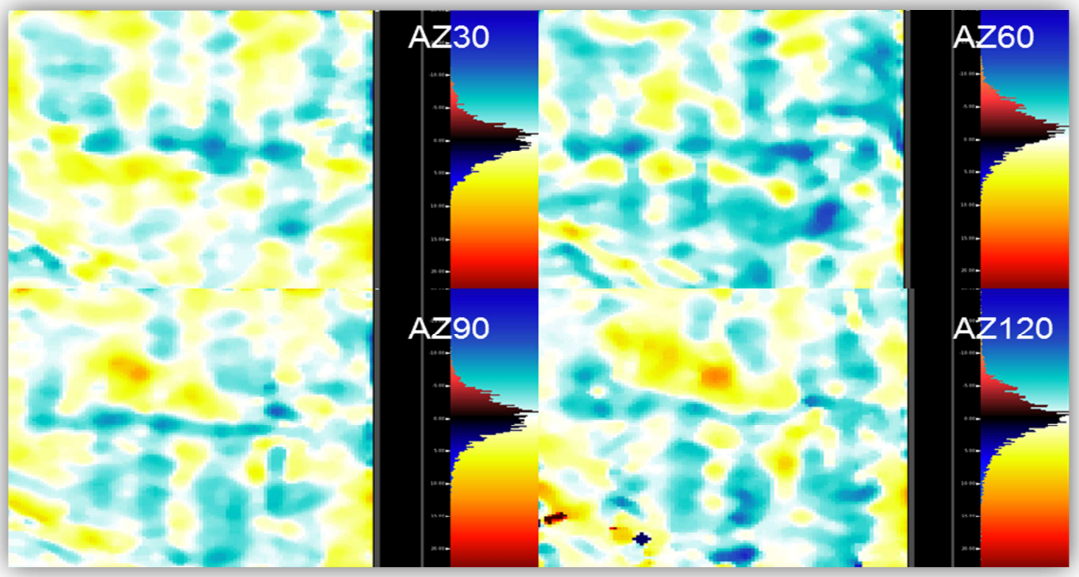

Figure 4-34. Smooth attribute maps of vertical shifts representing residual moveouts for different azimuth sectors at angle bin centered around 30 degrees of opening angle, with their respective color scales and histograms to the right of each of the four maps.

4.3.1.5 Smoothing of Residuals

After the residual moveout picking, it was of interest to remove localized anomalies or any noise that did not correspond to regional moveout patterns. From a statistics

perspective, this can be achieved by smoothing the residuals. If the length of the smoother is approximately the size of the smallest anomaly to be considered resolvable as signal, all smaller variations will be filtered out, minimizing their impact.

In order to accomplish this, the vertical shifts calculated from the cross-correlation picking were effectively smoothed by using a trend estimation routine that fits the data according to a specified radius around each live sample, with a second order local polynomial function. By using this technique, one can consider the results of the second order polynomial-fitting as the signal representing the trends throughout the data, while the remainder can be thought of as noise present in the data that needs to be removed.

Note that the noise or residuals that are not honored by the polynomial fitting typically have a relative higher frequency character and this separation will be dependent on the radius chosen for the local fitting.

In addition, due to the chaotic or unordered patterns observed in the relatively simple test area, a five-point or 250m median filter was also applied in an effort to aid the recognition of large scale features of hundreds of meters. An example of the resulting smoothing is shown next in Figure 4-35.

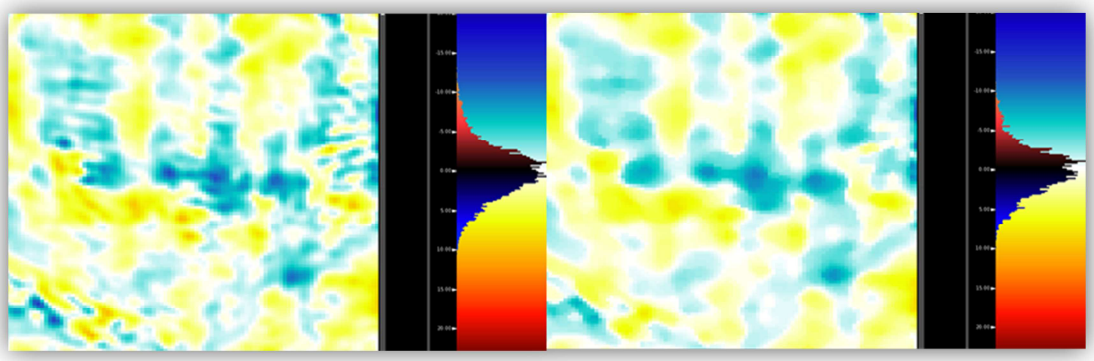

Figure 4-35. Comparisons between the unsmoothed (left) and smoothed (right) attribute maps corresponding to the second azimuth sector, and 30 degrees of opening angle. The respective color scales correspond to the magnitude and sign of all shifts, and are being overlaid by a histogram of the estimated shift values along a test surface horizon.

A key point is that the magnitude of the actual measured residual will be diminished by this filtering. But since the main target is to identify patterns that can be related to plausible geologic scenarios and not invert for small scale rock properties, it was considered appropriate to apply these smoothers. Also, this fits with the seismic scale of the experiment. At 15Hz, energy travelling at 2750 m/s will have a correspondent wavelength of approximately 183m. In this case, 2750 m/s corresponds to an average velocity for the shallow unconsolidated sediments, but since the velocity typically increases with depth due to compaction, there will only be larger wavelengths to deal with at depth.

4.3.1.6 Additional Attributes Maps, Plots and QC's

In order to better understand the azimuthal variations in question, additional attribute maps of different properties can be generated. Starting with the models used in the tilted polar migration, Figure 4-36 illustrates four different horizon maps corresponding to the intersection of each anisotropic model and the interpreted horizon. Note that δ and ε gently increase toward the deeper portion of the horizon (center of the mini-basin), while the changes in the slopes throughout this horizon are minimal and vary symmetrically across the center.

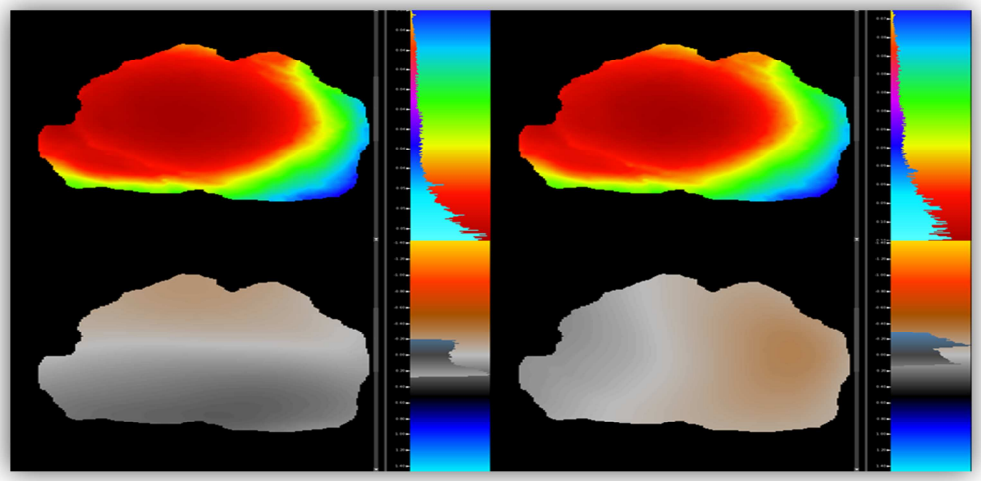

Figure 4-36. Attribute maps of δ (upper left), ε (upper right), slope X (lower left) and slope Y (lower right). δ ranged from 4% to 5% and ε varied from 8% to 10%, while slope X ranged from approximately -12° to 12° and slope Y from -17° to 10° .

If any of the observed patterns within the attributes resembles the patterns in the residual maps across azimuth sectors, this will be indicative of either model induced

anomalies or perhaps variations related to heterogeneity, since these models are effectively trying to compensate for it during the migration.

Other attributes to evaluate are the V_{tilt} model and the stack amplitudes at the interpreted horizon level (Figure 4-37). Again, these maps can aid the understanding of certain azimuthal anomalies, in the case that there is correlation between these attributes and the measured residuals. Since the first test area was selected due to its simplicity, in order to try to limit the analysis to azimuthal variations related to regional stresses or preferential alignments patterns in the area, these sets of attributes corresponding to a simple mini-basin do not help the analysis, but rather confirm that observed azimuthal variations are not being introduced by the models. These types of attributes will be more useful when evaluating complex areas, where one can at least rule out that a given anomaly is being induced by a model or strong heterogeneity.

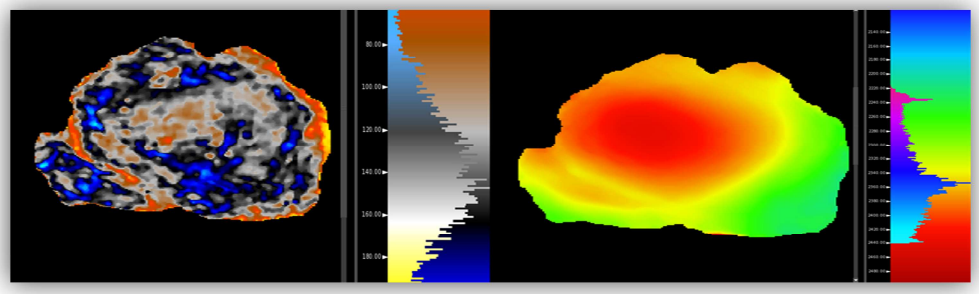

Figure 4-37. Attribute maps corresponding to the stack amplitude (positive values corresponding to an increase in impedance) and V_{tilt} (the green color represents velocities around ~2,250m/s, while the red color equates to ~2,400m/s) at the interpreted horizon.

Perhaps a better way to verify if an anomaly is being introduced by a combination of the migration models is to generate impulse responses with the same migration algorithm. One can then analyze depth slices of these images at the target level and determine if these patterns follow or not any of the features in the models. If there is no correlation between the impulse response and the features observed in the model, one can rule out the possibility that a given azimuthal anomaly was solely introduced by a component of the model. Figure 4-38 shows an impulse response with the V_{tilt} model overlaid on top of the depth slice image. The V_{tilt} overlay was chosen because it is usually the model that presents the most features. In this case, the anisotropic models δ, ε, slope X and slope Y were all quite smooth, but if any of the migration models exhibit significant features, this type of display can be utilized to assess their impact on the respective migrated images.

Finally, another way to quickly evaluate azimuthal variations throughout an area is to plot pseudo-depth slices of azimuth gathers as tiles. For these displays, one can specify the number of inlines, crosslines, azimuths and depths to analyze, and their respective increments, extent and sort order in a plotting routine so that detailed tiling of these results can be achieved.

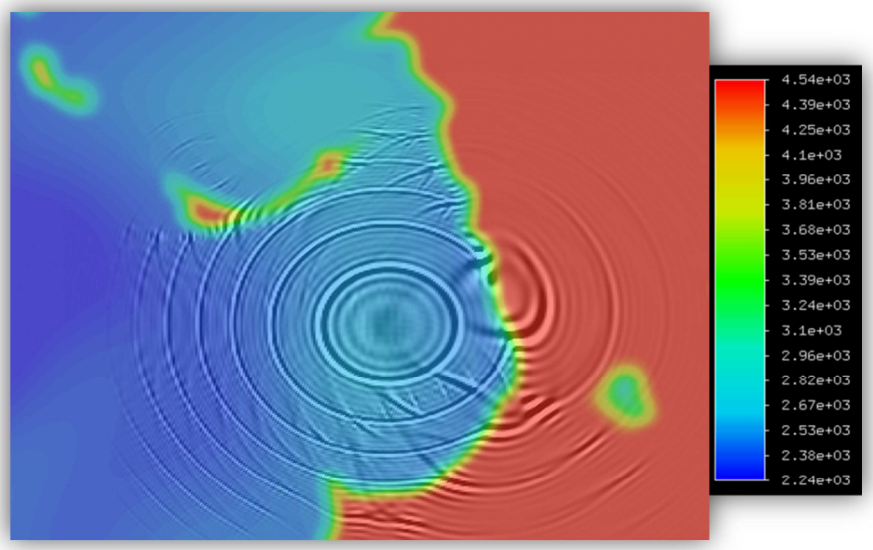

Figure 4-38. Depth slice of impulse response at target level, with V_{tilt} overlay.

An example of this type of plot is shown in Figure 4-39, where inlines and azimuths are plotted vertically, and crosslines and depth slices horizontally. This plot can be used to aid the understanding of spatial patterns of azimuthal variations within a target area, without having to rely on picking residuals that are then mapped as an attribute along a given horizon. Alternatively, one can apply the picked residuals to the gathers, and generate the same kind of plot, in order to easily perform visual quality control by comparing plots before and after their application.

Note that this display is a much more efficient way of qualitatively evaluating the residual moveouts of a target area without having to scroll through numerous gathers, line by line. However, the only downside to this method is that, depending on the

parameters used to generate these plots and dip at the target level, it can result in an extremely large plot, or it might be biased by higher or lower sampling in a particular direction. Therefore, careful parameterization of these plots is key when trying to assess the significance of a given anomaly.

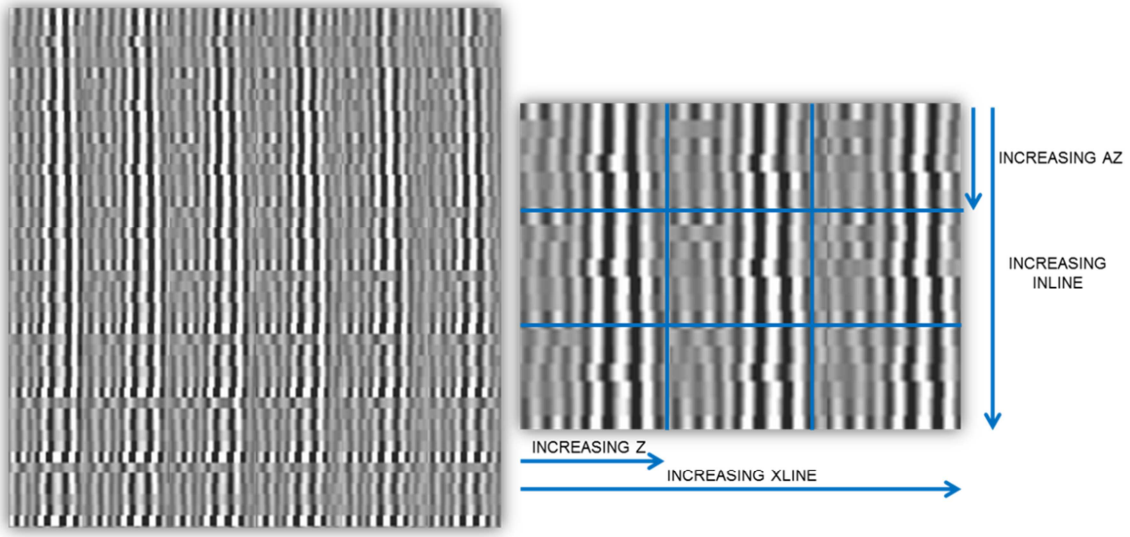

Figure 4-39. Example of tiles being plot to efficiently evaluate the spatial distribution of azimuthal moveout through a given area (left), and a diagram demonstrating the respective sort order for each axis (right) . Note that this particular area does not exhibit substantial azimuthal variations, as events within a given tile are predominantly aligned.

4.3.2 Targets

In order to efficiently evaluate the dataset with a limited amount of uncertainty, the targets selected for this study will include a simple proof-of-concept type scenario,

followed by a few more complex cases to help validate the derived workflow. All initial analyses and comparisons were carried over a relatively small and simple 150 km^2 test area (Figure 4-40). This area was selected because of the presence of relatively flat, well behaved young sediments, and although there is an obvious structure component to this area, the shallow and middle portions of this fairly symmetric mini-basin are not greatly affected by dip. These features, and the fact that the mini-basin resulted in flat full-azimuth gathers, but presented small azimuthal variations across azimuth sectors when migrating with relatively smoothed and simple tilted polar anisotropic models, validated that this area constituted a somewhat controlled setting that was suitable for the workflow derivations tests.

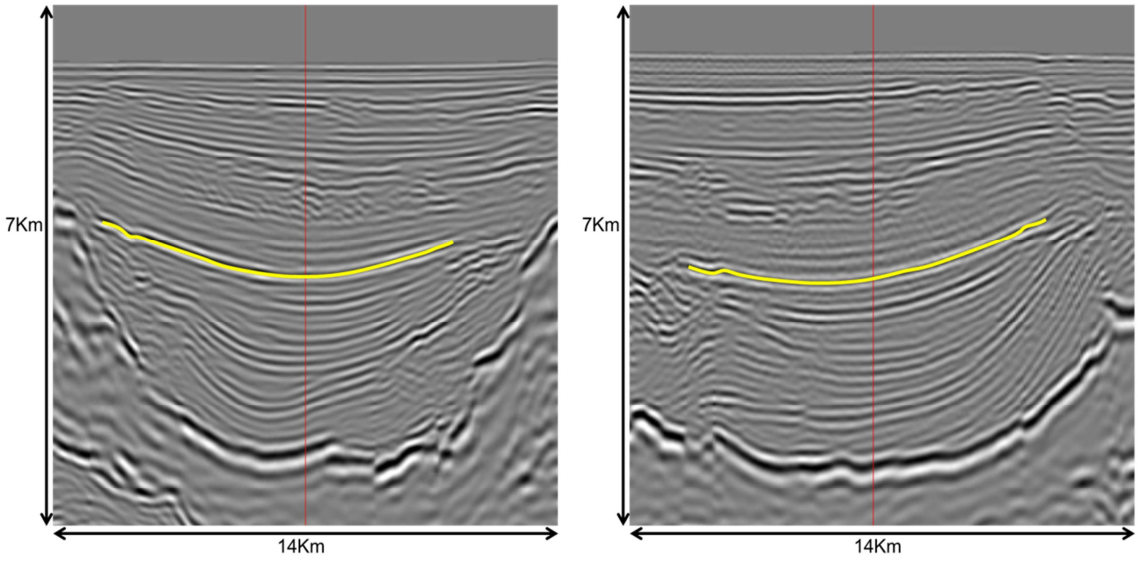

Figure 4-40. Inline (left) and crossline (right) displays of the initial quasi-symmetric mini-basin test area. The red lines indicate the respective location for the displayed inline and crossline.

The second test area corresponds to a mini-basin somewhat similar to the first test area, but tilted along the inline direction (Figure 4-41). This particular area was also chosen due to its apparent higher shale content and its proximity to both semi-transparent shale bodies and salt canopy features.

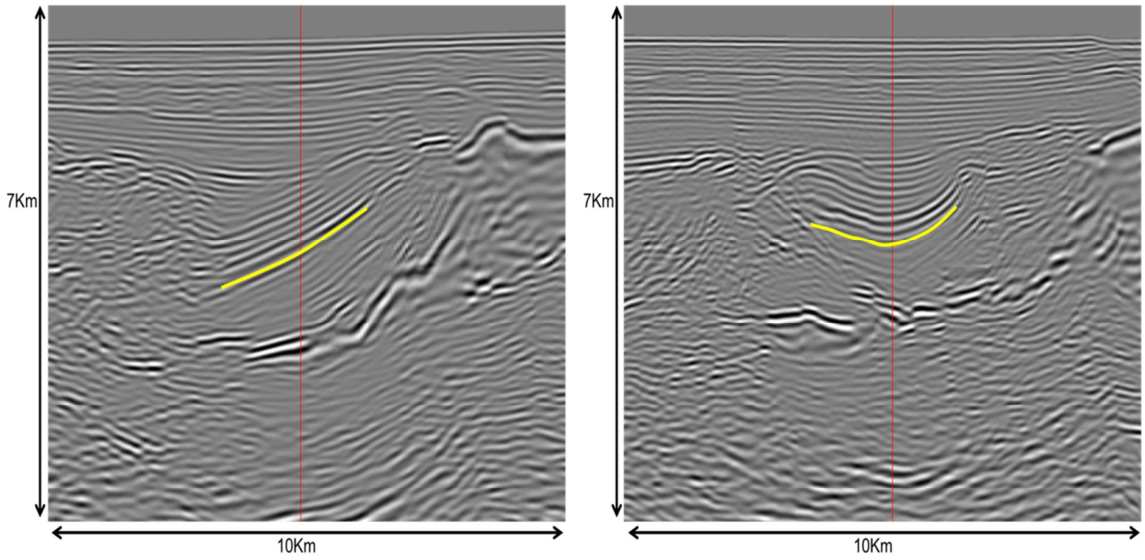

Figure 4-41. Inline (left) and crossline (right) displays of the second test area. The red lines indicate the respective location for the displayed inline and crossline.

Next, a more complex case was selected as the third test area. This 70km^2 subset presented a strong azimuthal anomaly along a bright subsalt reflector, which presented a radically different setting with respect to the other studied targets. Figure 4-42 shows inline and crossline through the central portions of this test area. Note that this particular case will be particularly challenging to understand, due to the intricacy of the raypaths that are contributing to construct such an image.

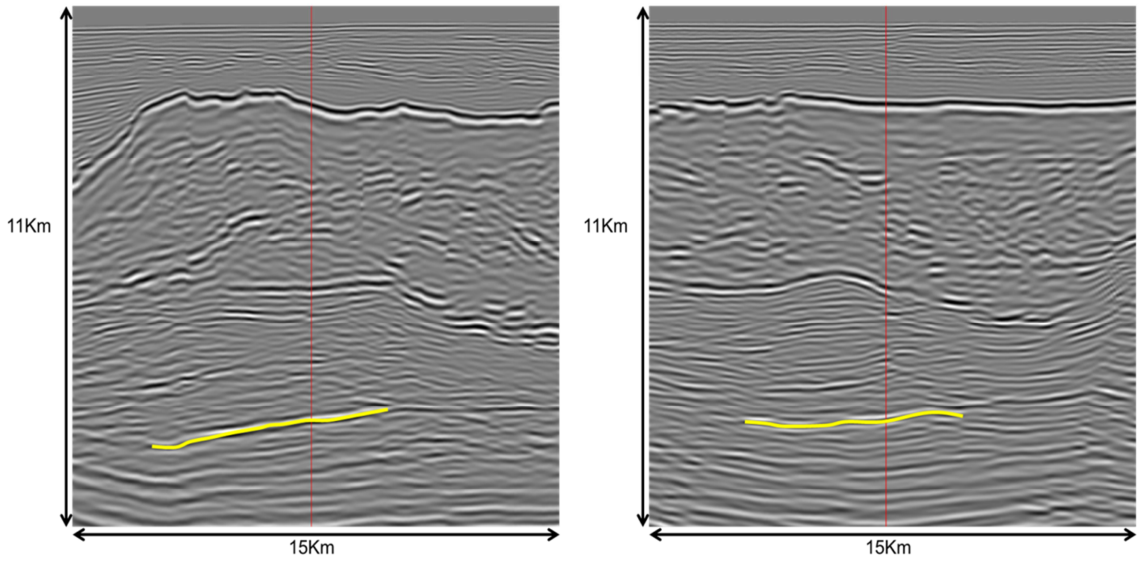

Figure 4-42. Inline (left) and crossline (right) displays of the third test area. The red lines indicate the respective location for the displayed inline and crossline.

4.3.3 Results

4.3.3.1 Test Area 1 – Shallow Symmetric Mini-Basin

After the final derived workflow was in place, several subsets of the dataset were put through the same workflow in order to study azimuthal variations throughout other areas, and also to validate how appropriate was the workflow for different geologic scenarios.

The initial results, where the geometry of the symmetric basin was thought to be simple enough that smooth tilted polar anisotropic models will deliver a good image, and large scale heterogeneity will be compensated for, primarily showed small residuals in the

order of 10 to 20m. After picking the cross-correlation shifts associated with residual azimuthal moveout, a horizon was interpreted at a strong amplitude event around 3.5 km depth. Then, maps of the calculated vertical shifts along this surface were extracted, plotted and smoothed accordingly. Even though this basin is partly surrounded by allochthonous salt features, which are potential sources of regional stress that could induce azimuthal anisotropy, the moveout patterns (Figure 4-43) were somewhat randomly distributed and relatively small in magnitude. While these residuals can possibly be used for minor enhancements to the overall stack response, there are no significant azimuthal variations that will call for additional model building work in the area.

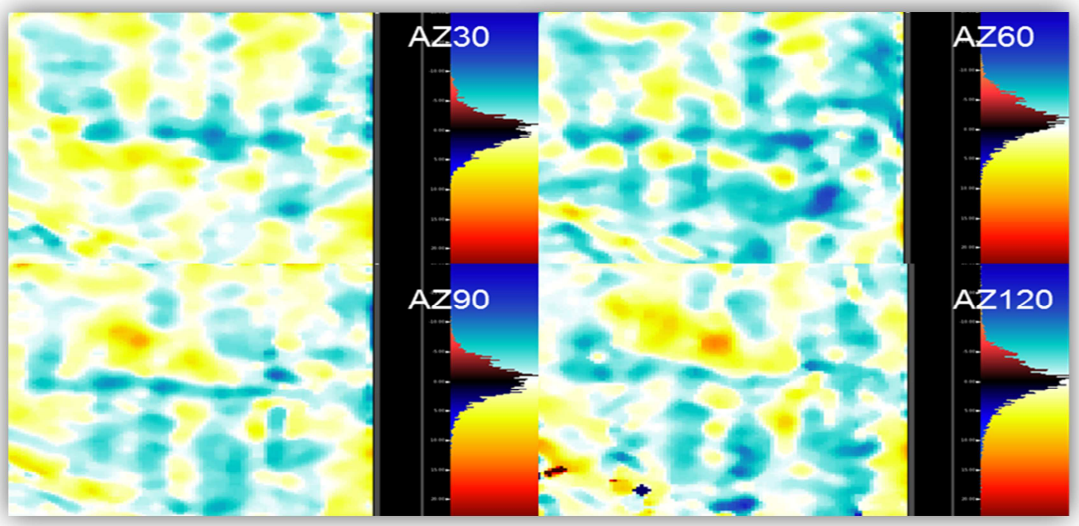

Figure 4-43. Comparison of smooth attribute maps of vertical shifts representing residual moveouts for different azimuth sectors at angle bin centered around 30 degrees.

However, it was interesting to notice that three of out the five histograms showed residual approximately distribute around zero. Only the azimuth sector centered around 60 degrees of azimuth revealed a slight bias towards negative residuals. While this trend could correlate to an azimuthal anisotropy anomaly, modeling work exercises would be necessary to check if the observed behavior is in fact a result of certain degree of directional order at the scale of this study.

The other interesting patterns observed in Figure 4-43 are linear features along both inline and crossline directions. Because these anomalies exactly parallel the grid axes, it is very likely that they are either migration or post-processing artifacts. While there is only one consistent lineation along the inline direction, multiple linear features oriented along the crossline direction appear approximately every 800m. This does not correspond with the expected acquisition footprint of 150m between shots along the sail-line direction or the window size used during either the denoising of the gathers or the smoothing applied to the residuals; while these anomalies are questionable, at this point there are no concrete explanations for their occurrence.

Finally, as previously stated throughout Section 4.3.1, several attributes and QC plots were generated to validate the simplicity associated with this initial test area, validating that it was a relatively unbiased geologic scenario where techniques to evaluate azimuthal variations could be initially tested. To avoid repetition, this section will focus

on the other test areas, where there will be a more detailed discussion of the results obtained.

4.3.3.2 Test Area 2 – Tilted Shallow Mini-Basin Adjacent to Transparent Shales and Allochthonous Salt

The second target also presented relatively small azimuthal moveouts. While similar residuals were picked in terms of magnitude, at least one significant trend where the azimuth gathers exhibited negative moveout (gathers curving up) was detected.

First, by looking at ADCIG's (Figure 4-44), the angular coverage was evaluated to determine which angle bin to use for assessing azimuthal variations. It was decided that 30 degrees of opening angle presented a good compromise in terms of signal to noise ratio, that it was a reasonably well populated bin, and therefore that it was suited for the testing of the workflow. Note that while narrower angles may have more information to work with, it is at wider angles that the energy has traveled longer paths and therefore there is a better chance to observe azimuthal variations.

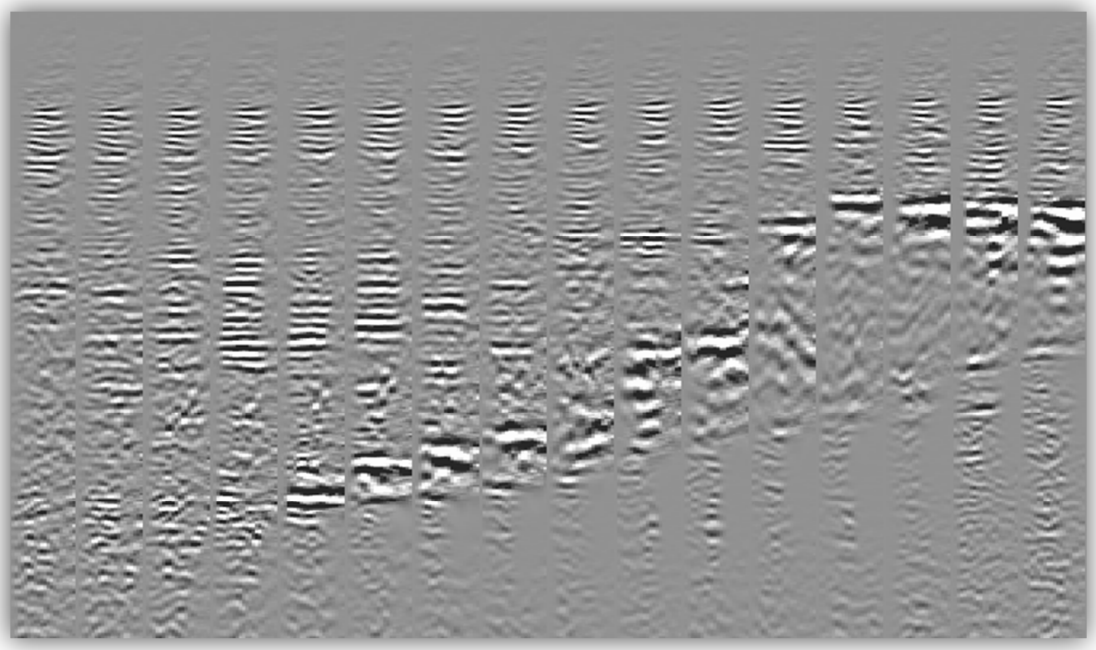

Figure 4-44. Full-azimuth angle gathers for the central inline of the second test area. For this display, the six different azimuth sectors have been stacked together to generate this full-azimuth gathers.

After running the cross-correlation algorithm to pick the azimuthal moveout residuals for the targeted horizon, an anomaly was clearly detected. This anomaly was approximately oriented along the inline direction and consistently showed the need for an effective speedup in velocities as the azimuth deviated from the acquisition direction.

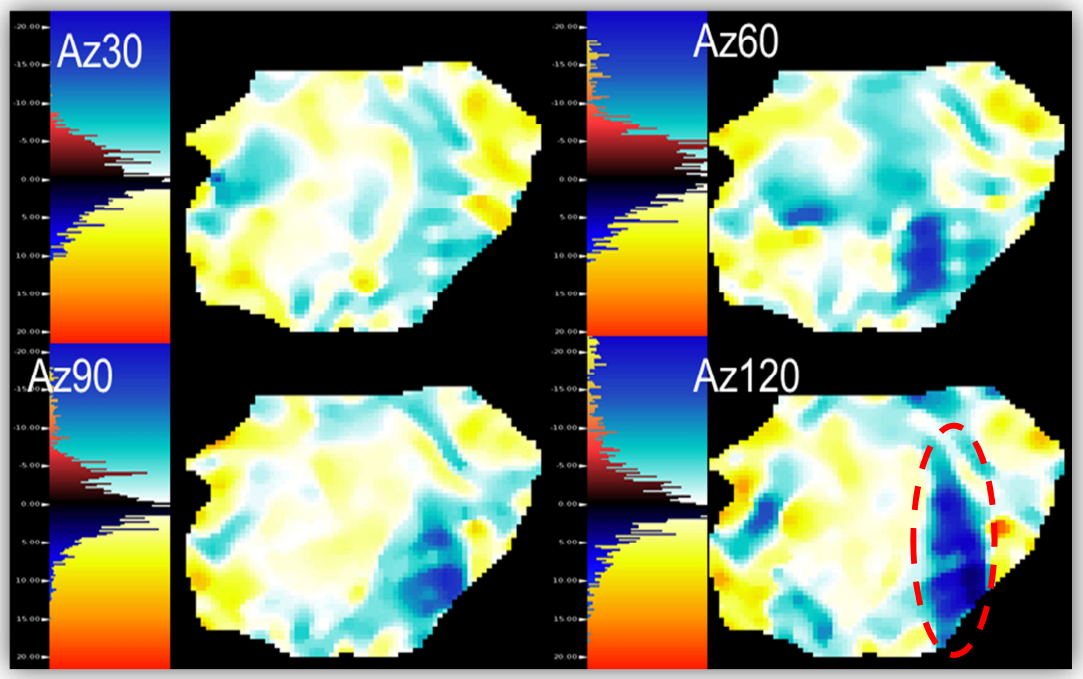

Figure 4-45. Comparison of smooth attribute maps of vertical shifts representing residual moveouts for different azimuth sectors at angle bin centered around 30 degrees. Note the red dashed oval highlighting the anomaly referenced throughout section 4.3.3.2.

As seen in Figure 4-45, the anomaly is most evident for the azimuth sector centered around 120 degrees, where it becomes approximately 400m wide along 2km. Next, attributes maps for the migration models and the stack amplitude were extracted and plotted along the targeted horizon.

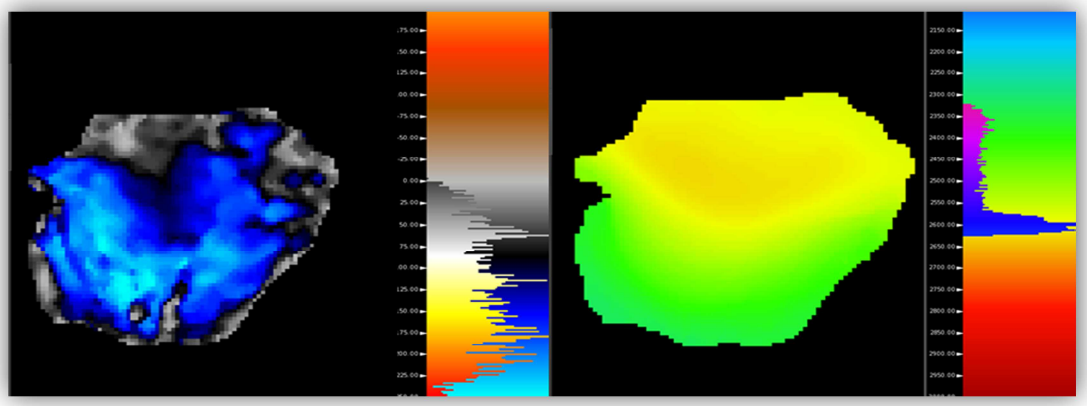

Figure 4-46. Attribute maps corresponding to the stack amplitude (positive values corresponding to an increase in impedance) and V_{tilt} (the green represents velocities around ~2,400m/s, while the yellow color equates to ~2,600m/s) at the interpreted horizon.

None of the attribute displays shown in Figures 4-46 and 4-47 showed any features that correlate spatially with the anomaly of interest (Figure 4-45). This was at least, a first indication that the azimuthal moveout was not being induced by a bias in the models.

Additionally, impulse response tests were run with the same migration algorithm and parameters for a few locations around this anomaly. The combined effects of all the tilted polar anisotropy models at this particular target were fairly well behaved. Figure 4-48 shows that taking a depth slice at the target level reveals quasi circular patterns in the center of the test area and not any particular irregularities that will induce this type of anomaly. This ruled out the possibility that the migration models were inducing this particular azimuthal deviation.

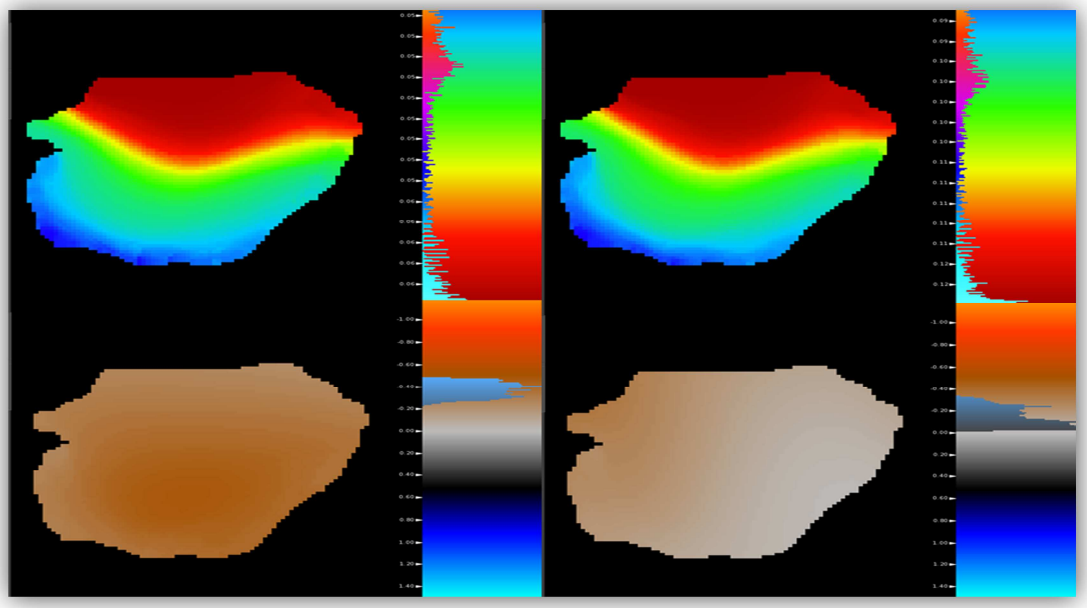

Figure 4-47. Attribute maps of δ (upper left), ε (upper right), slope X (lower left) and slope Y (lower right). δ ranged from 5% to 6% and ε varied from 10% to 12%, while slope X ranged from approximately -11° to -27° and slope Y from 0° to -20° .

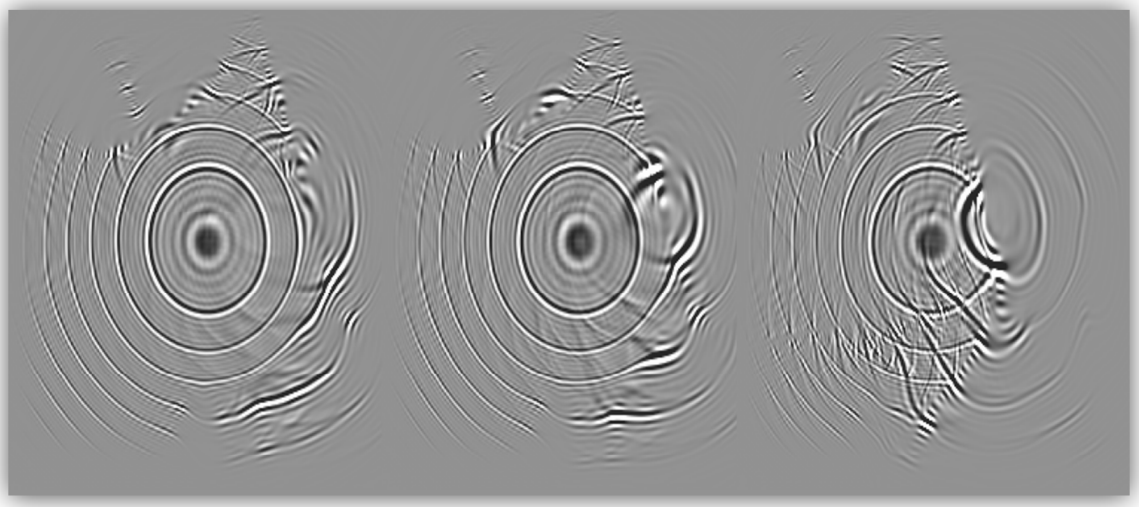

Figure 4-48. Depth slice of multiple impulse responses at the anomaly (left) and along the same inline as a salt flank is approached (center and right).

However, the interesting features to the right of each impulse response, correspond to the modeled reflections from the interpreted salt boundary, as demonstrated in Figure 4-49, where the red color represents salt velocity. Since the azimuthal anomaly parallels the edge of a salt body, one could speculate that it could be related to either heterogeneity that was not taken into account in these regional models, or induced anisotropy resulting from differential stresses caused by ongoing salt tectonic processes. Because the same anomaly is present in the residuals for all azimuth sectors it is more likely to be related to heterogeneity, not anisotropy. Further work to refine or add detail to the tilted polar models could confirm that this anomaly is related to inaccuracies in either the salt interpretation or the velocities directly adjacent to it.

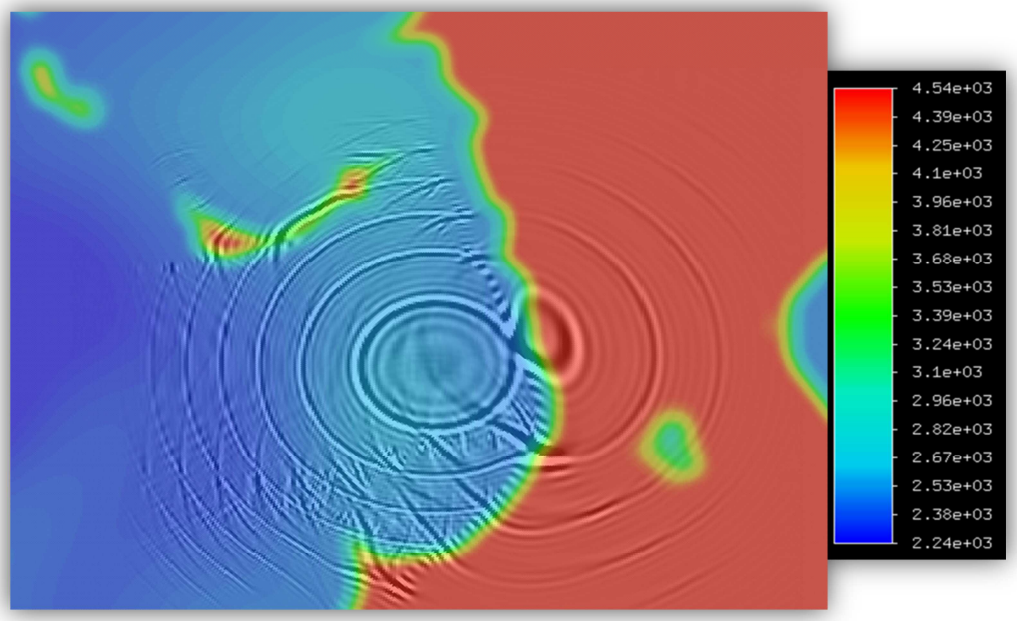

Figure 4-49. Depth slice of impulse response at target level with V_{tilt} overlay.

In order to validate the picked residuals, these were reviewed by applying the measured shifts back to the gathers. Figure 4-50 shows an inline example of this type of QC. Note that the bright dipping target reflector curves up with increasing azimuth sector in the top panel, but it is rather flat in the bottom one.

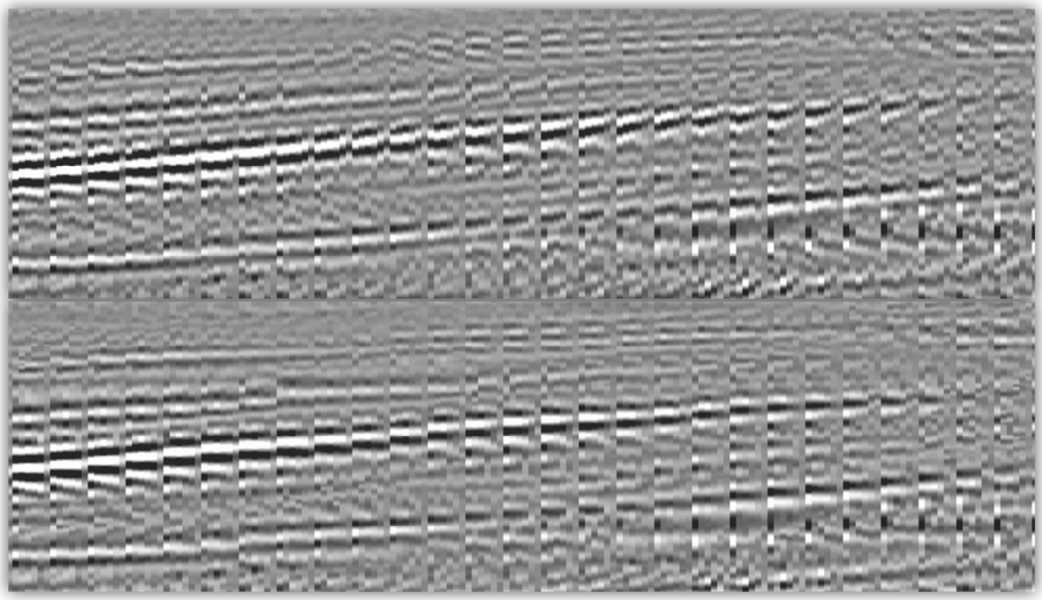

Figure 4-50. The top panel displays the azimuth gathers for 30 degrees of opening angle that were input into the cross-correlation picking routine, while the bottom panel presents the same gathers, but with the residuals applied.

As mentioned in section 4.3.1, spatial verification of the shifts over the area can be accomplished by plotting the azimuth gathers as tiles, in which azimuths and depth slices vary locally for a given inline and crossline pair. Figure 4-51 demonstrates the level of gather flatness achieved by the cross-correlation results in this area. As expected, the

identified anomaly shows towards the bottom right side of the left panel (blue square), corroborating the previously discussed results.

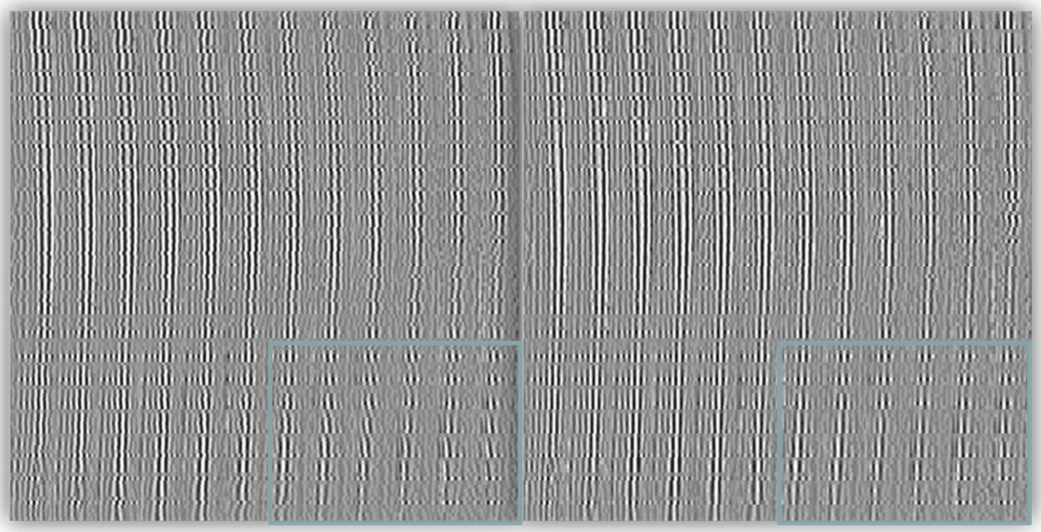

Figure 4-51. 3D spatial displays of depth slice azimuth tiles showing azimuthal moveout before (left) and after (right) applying the corrections, throughout the second test area.

4.3.3.3 Test Area 3 – Complex Subsalt Sedimentary Rocks

After the initial validation of the derived workflow done in the second test area, the entire dataset was scanned for substantial azimuthal anomalies, regardless of their location and associated complexities. A subsalt target at around 10 km depth, with relatively small dip, was thought to be of particular interest, since it showed a large but inconsistent amount of azimuthal moveout.

Salt velocity was modeled to be 4,500m/s; as such, this high velocity layer acts as a lens that tends to focus most energy towards the near opening angles. After evaluating full-azimuth angle gathers around the target area, it was decided that 15 degrees was a relatively high angle bin for the target level that still contained reliable data that could be used to evaluate azimuth deviations. Figure 4-52 shows an example of such gathers; note the dramatic decrease of energy at the far angle bins bellow salt.

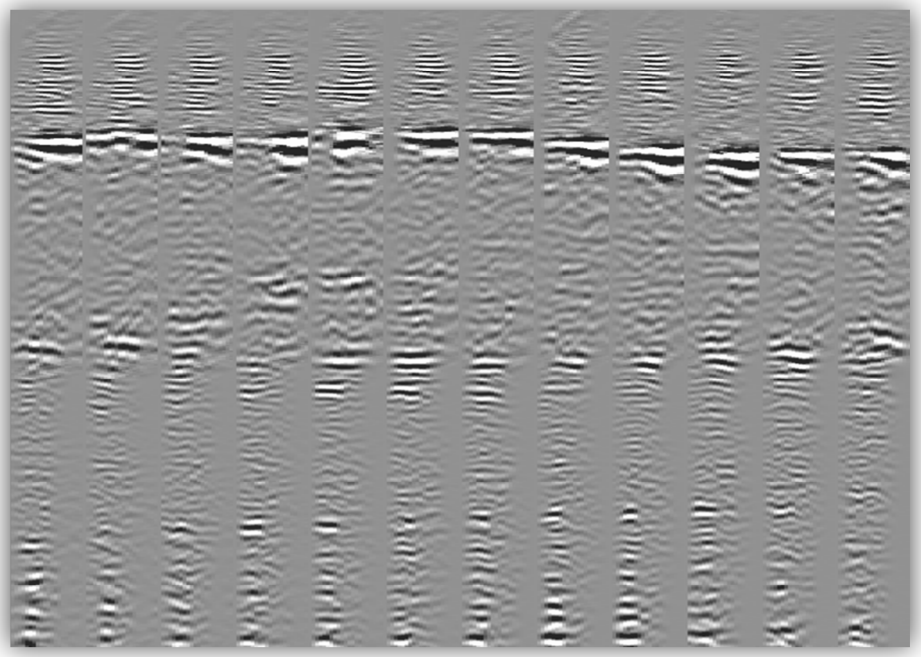

Figure 4-52. Full-azimuth angle gathers for the central inline of the third test area.

Figure 4-53 shows the same CIG location for both an angle gather with all azimuths stacked together and an azimuth gather for 15 degrees of opening angle, with only the latter exhibiting significant moveout.

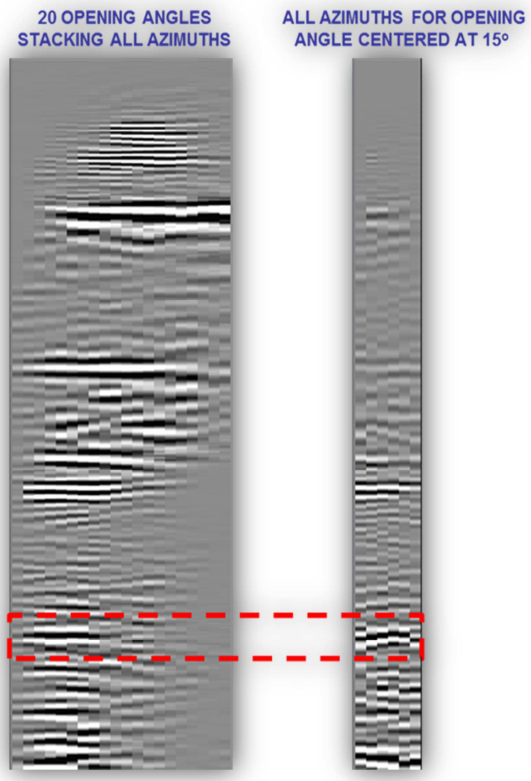

Figure 4-53. On the left is an ADCIG composed of 20 opening angles encompassing 0-60 degrees. On the right, the angle bin centered around 15 degrees has been decomposed into 6 different azimuth sectors.

After reconstructing azimuth gathers for the 15 degrees of opening angle bin, the cross-correlation routine was used to pick all residuals throughout the area. The lag and cross-correlation windows were optimized so that the algorithm was able to track the detected subsalt anomaly. Figure 4-54 presents the obtained results for four azimuth sectors. For this area, there are more significant anomalies in terms of the magnitude of

the measured shifts, but the vast majority of them still tend to be chaotically distributed. The only clearly identified patterns were that:

(1) overall this target presented a greater number of negative shifts consistently across all azimuth sectors, and

(2) contrary to what was observed in the second target area (where the shifts generally increase in magnitude with increasing azimuth sector), the shifts for this subsalt event tended to either change signs or not increase or decrease sequentially for all sectors more often.

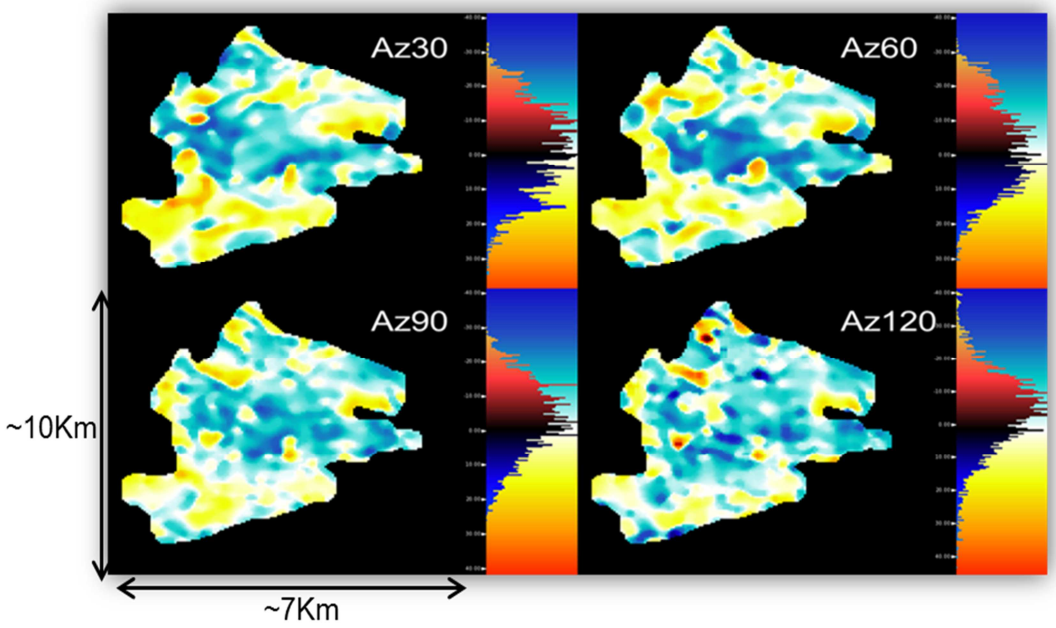

Figure 4-54. Comparison of smooth attribute maps of vertical shifts representing residual moveouts for different azimuth sectors at angle bin centered around 15 degrees of opening angle.

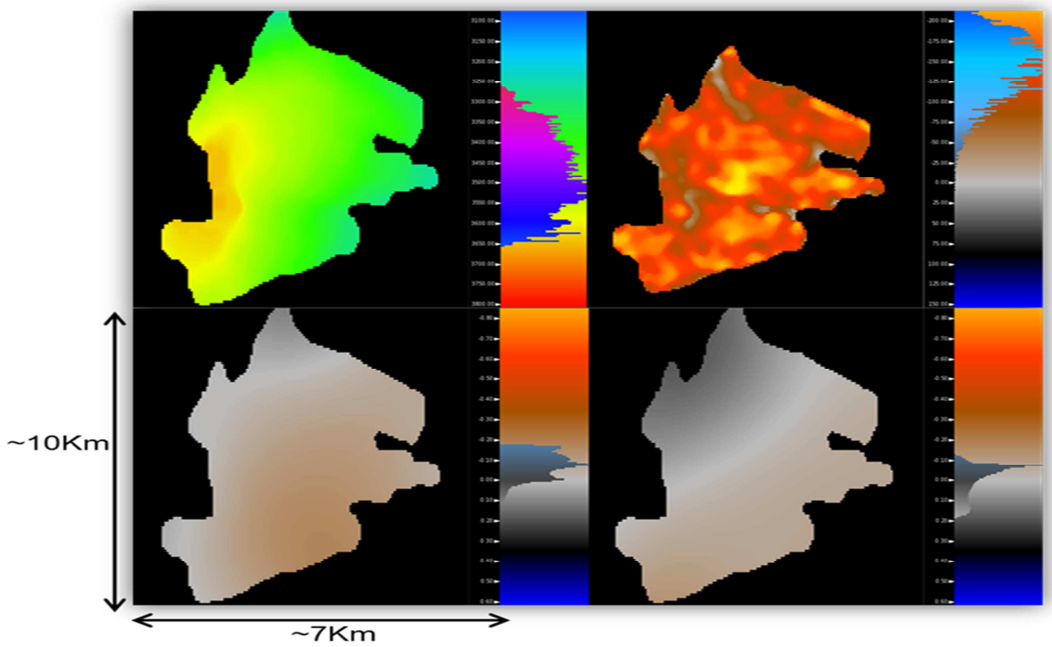

Figure 4-55. Attribute maps of V_{tilt} (upper left), stack amplitude (upper right), slope X (lower left) and slope Y (lower right) at the interpreted horizon.

For this scenario, attribute maps for δ and ε are not shown these models are clipped to their maximum values of 6% and 12% respectively. The only attribute that displayed similar patterns to the calculated residuals was the stack amplitude map (Figure 4-55). This is to be expected, since as the magnitude of the residuals increases meaningfully, amplitude anomalies of the resultant stack should exhibit a similar response due to the lack of alignment in the gathers. Perhaps this was not observed in the two previous cases because the magnitudes of the anomalies were small enough to be within the stack noise level.

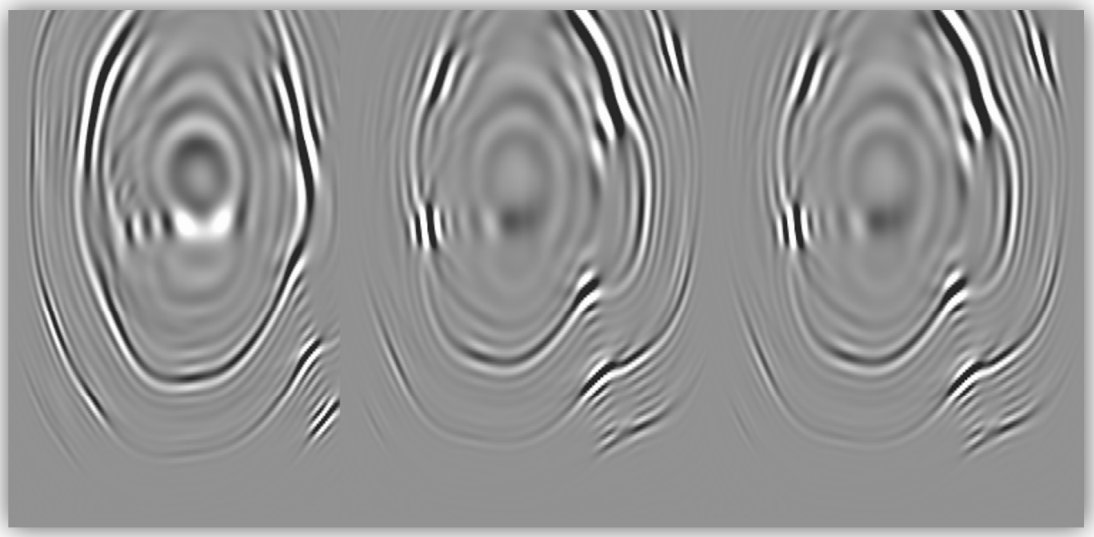

Figure 4-56. Depth slice of multiple impulse responses at the anomaly (left) and along the same inline toward an area without anomalies (left).

To try to better understand this azimuthal anomaly, impulse responses for several locations around the center of the target were migrated. Depth slices of these impulse responses showed a much more complex response. When comparing impulses at locations with substantial moveout or flat gathers (Figure 4-56), the patterns presented by these impulses did not vary significantly. Additionally, when overlaying the V_{tilt} model on top of a depth slice of an impulse response at the anomaly's location (Figure 4-57), no appreciable similarities were observed since the character of the model for this area was considerably smooth, but the impulse presented a much higher level of complexity. Given the nature of these results, it was concluded that at the target level, the impulse

responses are complicated to interpret, but at least there was no evidence that the migration models were inducing the anomalies.

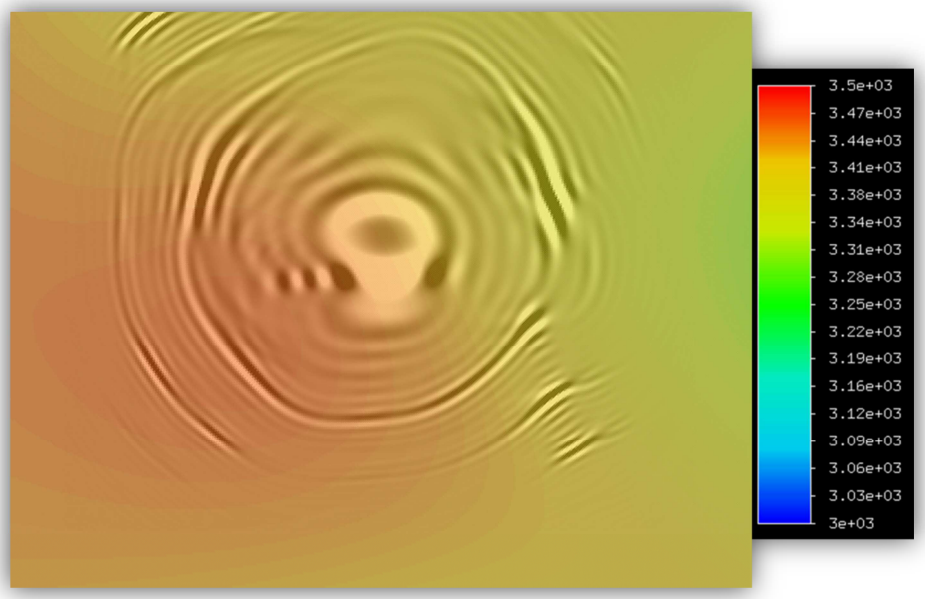

Figure 4-57. Depth slice of impulse response at target level with V_{tilt} overlay.

Figure 4-58 presents the inline display of azimuth gathers for data corresponding to 15 degrees of opening angle, before and after the application of the cross-correlation shifts discussed above. Note that, as many of the observed anomalies for this area, the extent of this particular one is relatively local, as it only extends a few hundred meters along (approximately) the inline direction. However, it was interesting to detect this type of anomaly, with significant amount of azimuthal residual that cannot be discovered by only looking at full-azimuth only gathers.

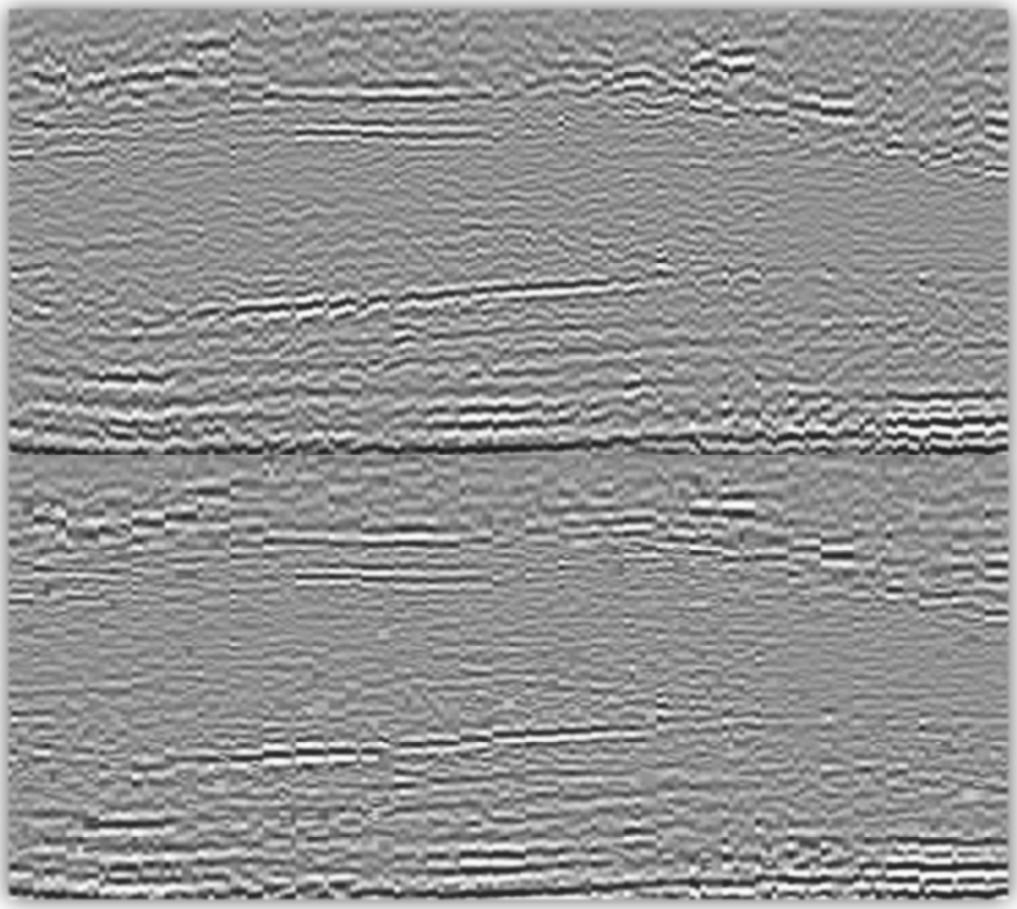

Figure 4-58. The top panel displays the azimuth gathers for 15 degrees of opening angle that were input into the cross-correlation picking routine, while the bottom panel presents the same gathers, but with the residuals applied.

Given the magnitude of the residuals, the flattened gathers were stacked to evaluate the impact from this residual moveout correction at stack level. Figure 4-59 illustrates this comparison, in which significant new structural features appear due to the better alignment of the respective azimuth gathers.

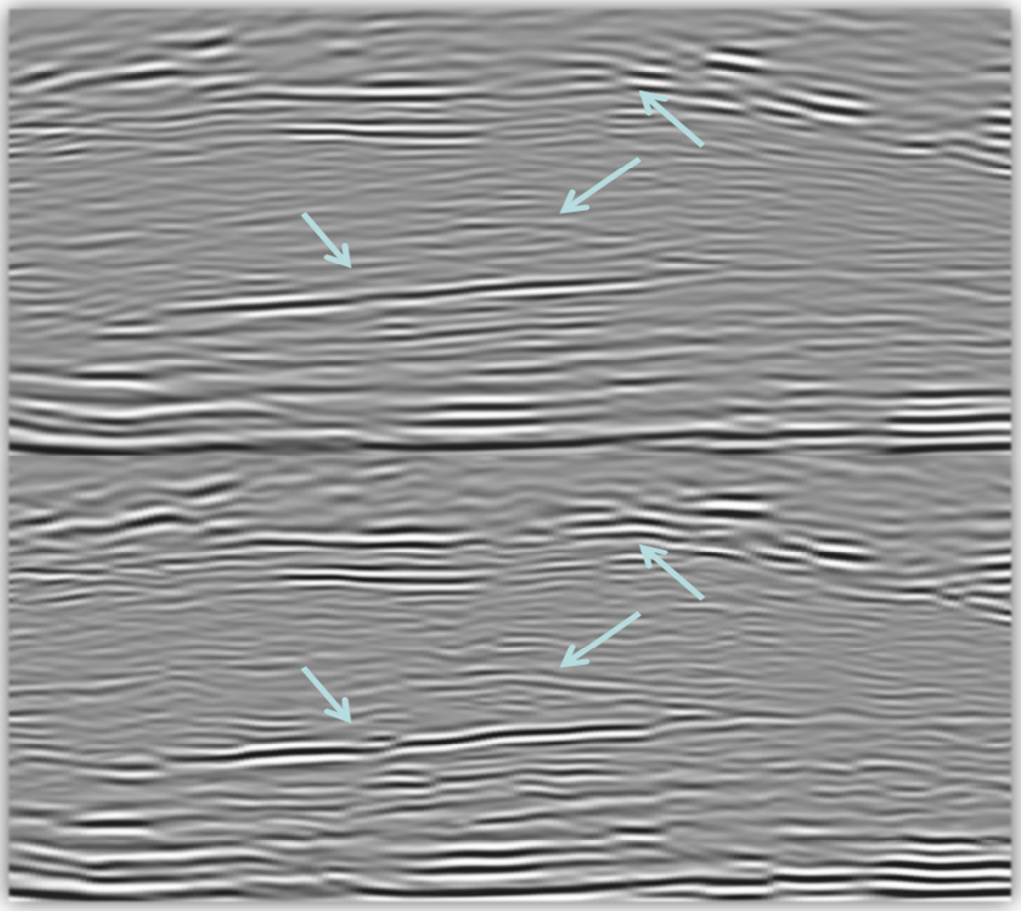

Figure 4-59. The top panel displays the full-azimuth stack for 15 degrees of opening angle from the gathers that were input into the cross-correlation picking routine, while the bottom panel presents the stack of the corresponding residual-flattened gathers. The arrows indicate key structural features that significantly changed after applying these residuals.

Another important point is that the majority of the moveout for all azimuth sectors corresponded to negative shifts; this suggested that most of the residuals are related to heterogeneity and not anisotropy. Regarding the relatively strong anomalies that correlated with the stack amplitude extractions features, looking at a few crossline

panels that run across them (Figure 4-60) demonstrates the degree of complexity and amount of relief at the base of salt event. Moreover, as shown in Figure 4-61, the base of salt map does not possess any particular features that can directly be related to the above anomalies.

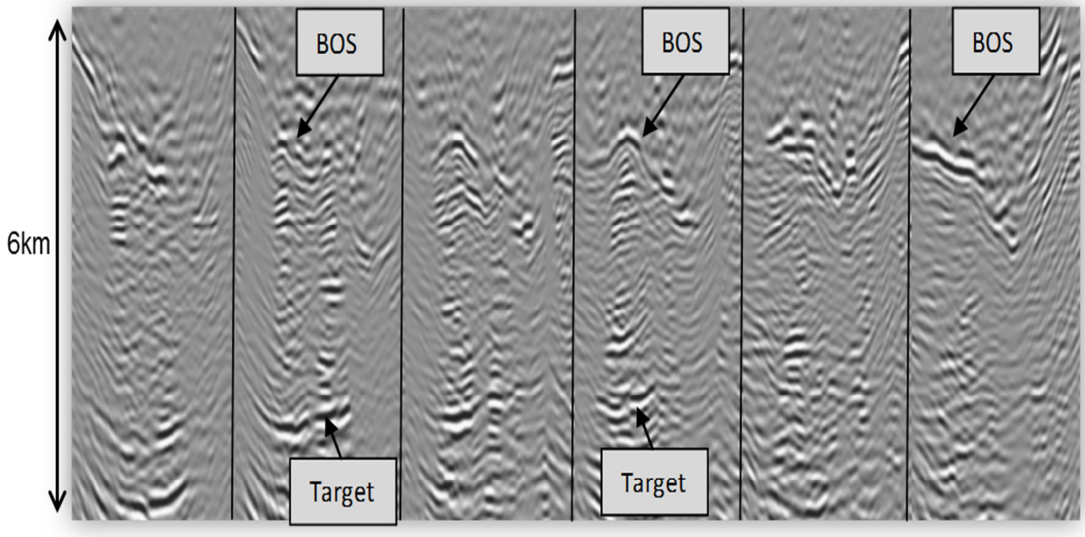

Figure 4-60. Six crossline panels for test area#3, with 1Km spacing between them.

While the argument for heterogeneity as the source of these azimuthal variations could be made, the varying change in signs across azimuth sectors indicates that it could also be related to azimuthal anisotropy as the cause. In actuality, these variations are probably a function of both heterogeneity and anisotropy, but without refining the migration models via interpretation or a tomographic update to rule out heterogeneity

as the leading source, it would be dubious to claim that either source alone is accountable for these effects in the data.

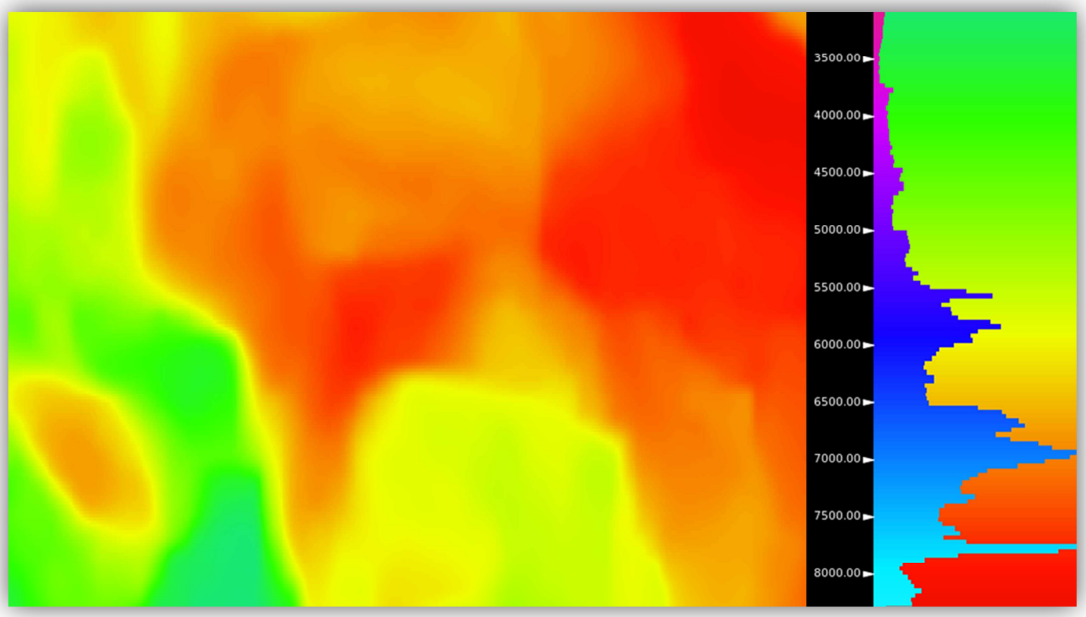

Figure 4-61. Base of salt regional interpretation map exclusively over Test Area 3. The green color represents shallower portions of the horizon (~4Km of depth), while the red corresponds to deeper areas (~7.5Km of depth).

Finally, to efficiently assess the cross-correlation results in a 3D manner, the tiling display of azimuth and depth slices was produced around the area of interest. Figure 4-62 shows this display for the central portion of this test area. Although the cross-correlation shifts do break in a couple of minor low signal-to-noise zones, the majority of the measured shifts were considered to be accurate.

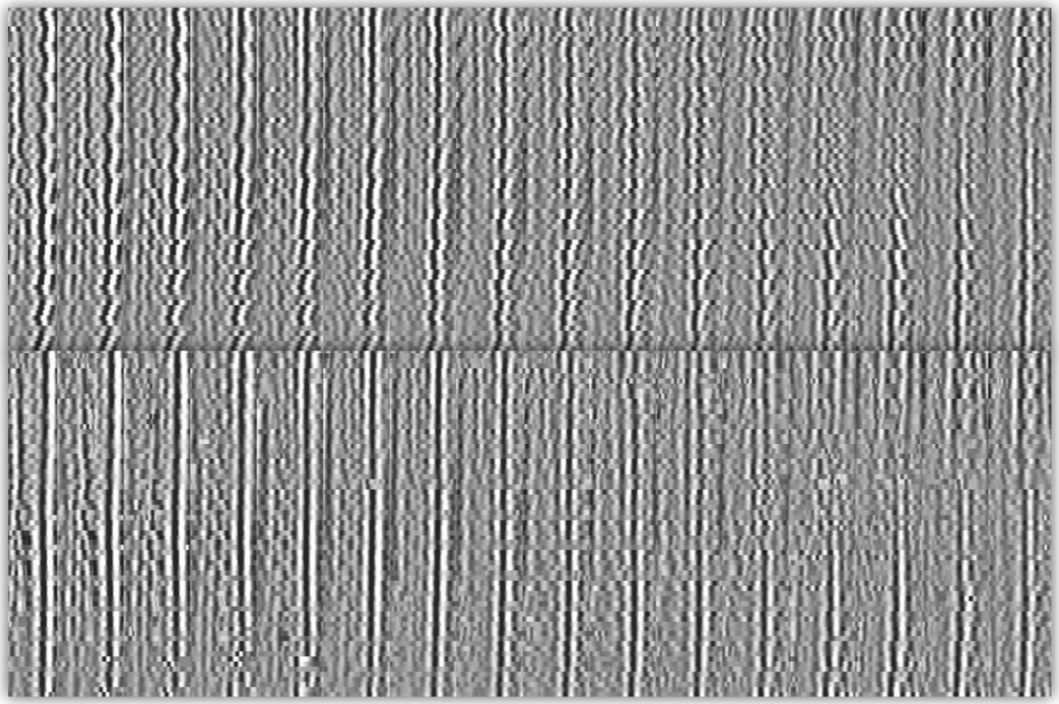

Figure 4-62. 3D spatial displays of depth slice azimuth tiles showing azimuthal moveout before and after corrections, throughout the third test area.

The analysis of this third target ends the Results subsection and the Methodology and Results chapter.

5. Discussion

The majority of the results presented almost random or chaotically distributed azimuthal residuals. For different areas and target horizons, it was possible to observe different types of azimuthal moveouts. Some areas presented moveouts that continuously increase or decrease with azimuth sector, while others showed more of a scalloping pattern with significant deviations only at the middle azimuth sectors.

Due to the high level of geological complexity in the data, the general low resolution of the data, and the lack of forward modeling exercises, it was not possible to correlate some of the observed anomalies to actual geologic sources. However, the proposed workflow does include techniques for identifying if a given anomaly is likely to be induced by the migration models. This was intended to at least rule out the migration models as possible sources that could be contributing to these anomalies. Note that the impulse responses associated with this techniques proved to be more valuable for shallow targets where the models are typically more reliable and heterogeneity tends to be better understood.

As shown in Figure 4-59 applying azimuthal residual moveout corrections can improve images of the subsurface. However, these images were not a result of properly migrating events to their respective position through derived models. Regarding future work for this topic, the next natural step will be to back-project the picked residuals into model updates with the purpose of improving the resolution of the models through a

multi-azimuth implementation of reflection tomography, hence compensating for a higher degree of heterogeneity. This assumes that the additional information from the decomposed azimuth and angle-domains will allow a better fit of the data through tomographic updates for the same type of symmetry system. Alternatively, if a higher order of symmetry system (that takes into account azimuthal variation of velocity) is used without model updates, the anisotropic component of the residuals would be the leading factor of potential improved results.

While the magnitude of residuals encountered in the first and second targets are not expected to translate to meaningful model updates, the third test area should benefit from such an update. Moreover, angle gather tomography can provide enhanced resolution subsalt due to the inherently better discrimination in moveout at depth (compared to offset gathers, where typically not enough offsets are recoded at the deeper portions of the data). Additionally, angle gather tomography only requires simplified ray-tracing that is typically more efficient than in the offset domain, because the ray-tracing associated with the back-projection of residuals becomes only an initial value problem (Zhou et al., 2012).

Finally, throughout this study several quality control methods and plots were described as a part of a variety of techniques. These were vital to the understanding of the obtained results, but only provided qualitative measurements. Future work should look

into new metrics, including quantitative results that could be used to try to improve the migration models.

6. Conclusions

After many iterations of decomposing and investigating relatively low frequency migrated images of azimuth-sectored angle-domain gathers from a GOM wide-azimuth survey, a practical and efficient workflow to assess the significance of azimuthal variations was derived and tested. The techniques mentioned in section 4.3, would allow not only detection of azimuthal effects, but also mapping their distribution at a given target and qualitatively evaluating the impact these have throughout a dataset.

6.1 Findings

Throughout this study, it became clear that the extra azimuthal sampling obtained from the wide-azimuth acquisition was sufficient to record a variety of azimuthal anomalies at multiple target levels. While the nature of most of these is still uncertain, the capabilities to record enough data to assess their significance do exist.

Regarding the migrated data generated for this study, it was found that: (1) depth migrated ADCIG's did exhibit sufficient moveout to be measured and (2) angle-domain imaging provided an efficient, flexible and intuitive way to decompose the data.

During the early stages of the workflow derivation, it was obvious that the ADCIG's had to be preconditioned for the benefit of the cross-correlation routine. Once appropriate scaling and denoising were applied to the azimuth gathers, the cross-correlation algorithm demonstrated that it was an appropriate method to measure the moveout associated with azimuthal anomalies. However, smoothing resulted in more interpretable results, since several trends became distinguishable across multiple azimuth sectors after applying a median filter of approximately 250m to the attribute map images.

Although only relatively large regional signatures were targeted: (1) the maximum frequency used for the migrated images, (2) the relatively sparse azimuthal sampling, and (3) the coarse acquisition grid (150x600m), were identified as the main limiting factors that diminished the resolution of the data, particularly in shallow sections.

6.2 Recommendations

This section will propose recommendations on what type of input data, data attributes, imaging parameters, and data analysis techniques, etc. are potentially better suited for this type of evaluation.

First of all, better azimuthal sampling during the data acquisition will be the most obvious factor that would impact the detection of azimuthal variations. Wide tow

acquisition designs for multiple directions will aid the recording of energy that traveled through a broader range of directions and therefore should provide more insights to the level of azimuthal variations in a given geologic scenario. Likewise, denser acquisition geometries will bring higher fold angular sampling. If a given set of opening angles are being recorded more often along the inline and crossline directions, it should result in higher signal to noise ratio for better populated angle bins; both of these factors will positively influence the quality of the data being input to the analyses described throughout this study.

Similarly, outputting more azimuth sectors for the depth migrated images should also provide a better handle of the distribution and character of these anomalies as a function of azimuth. However, the applicability of this concept is directly linked to the azimuthal sampling of a given dataset.

Increasing the maximum frequency of the azimuth-sectored angle gathers will also result in additional resolution that could benefit the evaluation of these variations, particularly at shallow targets.

Regarding spatial visualization of data, it would be ideal to extract not only the previously described depth slice tiles as a function of azimuth, but to generate the same plots with the data being extracted from actual interpreted surfaces. Such display will be a direct comparison with the other attribute maps discussed in this study, and therefore would help when correlating anomalies or specific features for any target.

For improving the residual moveout picking, optimizing the cross-correlation algorithm so that the user specified parameters vary with depth would improve results; this would facilitate the picking of azimuthal residuals and would add to the robustness of the algorithm itself. Another opportunity would be to smooth the picked residuals along structure instead of smoothing along inline, crosslines or depth slices. Assuming that the sources of the residuals are structurally conformant, this type of smoothing would better honor the geology.

Finally, as part of future work, forward modeling with an orthorhombic ray-tracer or other higher order of symmetry system will be particularly useful tool when trying to quantify and differentiate between azimuthal anomalies caused by heterogeneity or azimuthal anisotropy.

References

Backus, G. E., 1962, Long-wave elastic anisotropy produced by horizontal layering: Journal of Geophysical Research, 67, 4427–4440.

Biondi, B., and W. Symes, 2004, Angle-domain common-image gathers for migration velocity analysis by wavefield-continuation imaging: Geophysics, 69, 1283–1298, doi:10.1190/1.1801945.

Chu, C., B. Macy, and P. Anno, 2011, An accurate and stable wave equation for pure acoustic TTI modeling: 81st Annual International Meeting, SEG, Expanded Abstracts, 2011-0179.

Crawley, S., S. Brandsberg-Dahl, J. McClean, N. Chemingui, 2010, TTI reverse time migration using the pseudo-analytic method: The Leading Edge 29, 1378-1384.

Cary, Peter, X. Li, G. Popov, C. Zhang, 2010, Shear-wave splitting in compliant rocks: The Leading Edge 29, 1278–1285.

Dickens, Thomas A., and Graham A. Winbow, 2011, RTM angle gathers using Poynting vectors: 81st Annual International Meeting, SEG, Expanded Abstracts, 3109–3113.

Fowler, P. J., X. Du, and R. P. Fletcher, 2010, Coupled equations for reverse time migration in transversely isotropic media: Geophysics, 75, S11-S22.

Galloway, W., P. Ganey-Curry, X. Li, R. Buffler, 2000, Cenozoic depositional history of the Gulf of Mexico basin: AAPG Bulletin, 84 (11), 1743 – 1774.

Gray, S. H., J. Etgen, J. Dellinger, and D. Whitmore, 2001, Seismic migration problems and solutions: Geophysics, 66, 1622–1640, doi:10.1190/1.1487107.

Jenner, E., 2001, Azimuthal anisotropy of 3-D compressional wave seismic data, Weyburn Field, Saskatchewan, Canada: Ph.D. thesis, Colorado School of Mines.

Long, A., 2010, An overview of seismic azimuth for towed streamers: The Leading Edge 29, 512-523.

Lynn, H. B., D. Campagna, K. M. Simon, and W. E. Beckham, 1999, Relationship of P-wave seismic attributes, azimuthal anisotropy, and commercial gas pay in 3-D P-wave multiazimuth data, Rulison Field, PiceanceBasin, Colorado: Geophysics, 64, 1293–1311.

Lynn, H. B., L. Veta, and R. J. Michelena, 2011, Introduction to this special section: Practical applications of anisotropy: The Leading Edge 30, 726-730.

McDonnell, A., R. Loucks, W. Galloway, 2008, Paleocene to Eocene deep-water slope canyons, western Gulf of Mexico: Further insights for the provenance of deep-water offshore Wilcox Group plays: AAPG Bulletin, 92 (9), 1169 – 1189.

Michell, S., E. Shoshitaishvili, D. Chergotis, J. Sharp, and J. Etgen, 2006, Wide azimuth streamer imaging of Mad Dog: Have we solved the subsalt imaging problem?: 76th Annual International Meeting, SEG, Expanded Abstracts, 2905–2909.

Pech, A. and I. Tsvankin, 2004, Quartic moveout coefficient for a dipping azimuthally anisotropic layer: Geophysics, 69, no. 3, 699–707, doi:10.1190/1.1759456.

Ramos-Martinez, J., S. Crawley, B. Tsimelzon and S. Kelly, 2011, Full-waveform inversion by pseudo-analytic extrapolation; 81st Annual International Meeting, SEG, Expanded Abstracts, 2011-2684.

Rowan, M., F. Peel, B. Vendeville, 2004, Gravity-driven Fold Belts on Passive Margins: AAPG Memoir 82, 157 – 182.

Rüger, A., 1998, Variation of P-wave reflectivity with offset and azimuth in anisotropic media: Geophysics, 63, 935–947, doi:10.1190/1.1444405.

Thomsen, L., 1986, Weak elastic anisotropy: Geophysics, 51, 1954–1966.

Thomsen, L., 1988, Reflection seismology over azimuthally anisotropic media: Geophysics, 53, 304–313.

Tsvankin, I., 1997, Anisotropic parameters and P-wave velocity for orthorhombic media: Geophysics, 62, 1292–1309.

Whitmore, N. D., 1983, Iterative depth migration by backward time propagation: 53rd Annual International Meeting, SEG, Expanded Abstracts, 382–385.

Yilmaz, Ö., 1987, Seismic data processing: Society of Exploration Geophysicists, Tulsa.

Zhou, C., D. Whitmore and Brandsberg-Dahl, S., 2012, Tomographic model building with angle gathers, 74th Conference and Exhibition, EAGE, Expanded Abstracts, W040.

Zhu, J., J. Mathewson, and G. Liebelt, 2010, A case study for azimuthally anisotropic prestack depth imaging of an onshore Alaska prospect: Geophysics, 75, 177-186.

Zimine, S., G. Lambaré, P. Guillaume, J.P. Montel, J.P. Touré, N. Deladerrière, X. Zhang, A. Prescott, D. Lecerf, S. Navion, J.L. Boelle, A. Belmokhtar and A. Ladmek, 2010, Azimuthal anisotropy? The time and depth imaging points of view: an imaging case history: 72nd EAGE Barcelona, Extended Abstracts.